

UC Irvine

UC Irvine Electronic Theses and Dissertations

Title

Applications of diffuse optical spectroscopy in exercise physiology and metabolic disease

Permalink

<https://escholarship.org/uc/item/0xs2z49m>

Author

Ganesan, Goutham

Publication Date

2015

Copyright Information

This work is made available under the terms of a Creative Commons Attribution-NonCommercial-NoDerivatives License, available at <https://creativecommons.org/licenses/by-nc-nd/4.0/>

Peer reviewed|Thesis/dissertation

UNIVERSITY OF CALIFORNIA,
IRVINE

Applications of Diffuse Optical Spectroscopy in Exercise Physiology and Metabolic Disease

DISSERTATION

submitted in partial satisfaction of the requirements
for the degree of

DOCTOR OF PHILOSOPHY

in Pharmacology

by

Goutham Ganesan

Dissertation Committee:
Associate Professor Pietro R. Galassetti, Chair
Professor Bruce J. Tromberg
Professor Geoffrey W. Abbott

2015

DEDICATION

My wife Ranjani

And

Goddess Sarasvati

TABLE OF CONTENTS

	Page
LIST OF FIGURES	v
LIST OF TABLES	vii
ACKNOWLEDGMENTS	viii
CURRICULUM VITAE	xi
ABSTRACT OF THE DISSERTATION	xiii
CHAPTER 1: INTRODUCTION	
Background- Physiology	1
Background- Diffuse Optical Spectroscopy	13
CHAPTER 2: Brain and muscle oxygenation during incremental exercise in male adolescents	
Rationale	25
Methods	27
Results	32
Discussion	45
CHAPTER 3: Cerebral oxygenation during exercise with an assessment of the effect of training	
Rationale	52
Methods	54
Results	58
Discussion	72
CHAPTER 4: The effect of blood flow restriction on brain and muscle oxygenation during knee extension	
Rationale	78
Methods	81
Results	85
Discussion	94
CHAPTER 5: The use of diffuse optical spectroscopy to measure subcutaneous fat during calorie restriction	
Rationale	100
Methods	104
Results	111

Discussion	123
CHAPTER 6: Conclusion	130
REFERENCES	134

LIST OF FIGURES

	Page	
Figure 1.1	Sample Temporal Point Spread Function	17
Figure 1.2	Sample FDPM Phase and Amplitude fit	20
Figure 1.3	Sample ssFDPM fit	22
Figure 2.1	Sample tracings in PFC and VL	32
Figure 2.2	Subject TR-NIRS means for incremental exercise	34
Figure 2.3	Correlation of TR-NIRS and gas exchange	35
Figure 2.4	Correlation between [HbO ₂] and PETCO ₂	37
Figure 2.5	Muscle [THb] and PFC [HbR]	39
Figure 2.6	Scattering changes	43
Figure 2.7	Effect of constant scattering assumption	44
Figure 3.1	Raw tracings subject 1	60
Figure 3.2	Raw tracings subject 2	61
Figure 3.3	Raw tracings subject 3	62
Figure 3.4	Raw tracings subject 4	63
Figure 3.5	Training mean stO ₂	64
Figure 3.6	Training mean [THb]	64
Figure 3.7	Training mean [HbO ₂]	65
Figure 3.8	Training mean [HbR]	65
Figure 3.9	Segmented fits subject 1	67
Figure 3.10	Segmented fits subject 2	68
Figure 3.11	Effect of constant scattering assumption on stO ₂	71

Figure 3.12	Effect of constant scattering assumption on [THb]	71
Figure 3.13	Deep and superficial CW-NIRS during exercise	76
Figure 4.1	Exercise parameters	86
Figure 4.2	VMO oxygenation	87
Figure 4.3	Piecewise fits in one subject	90
Figure 4.4	PFC Oxygenation changes	92
Figure 5.1	Measurement schematic	110
Figure 5.2	Tissue thickness results	112
Figure 5.3	Sample ultrasound image	115
Figure 5.4	Scattering and absorption spectra	117
Figure 5.5	Mean differences	118
Figure 5.7	DOSI maps subject 8	122
Figure 5.8	DOSI maps subject 4	122

LIST OF TABLES

		Page
Table 2.1	PFC all comparisons	40
Table 2.2	VL all comparisons	41
Table 3.1	Trainign effects	58
Table 3.2	[HbR] threshold times	69
Table 4.1	Summary of regression results	91
Table 5.1	Anthropometric data	112
Table 5.2	All optical data	114

ACKNOWLEDGMENTS

Funding for the various projects described here was obtained from the following sources: NIH P01D048721 (PI: Galassetti), NIH 8UL1TR000153 (Ganesan), UL1TR000153 (Cooper), P41EB015890 (Tromberg), and the Arnold and Mabel Beckman Foundation. General support and funding was also provided by the UCI MSTP program and associated grant. Hamamatsu Photonics Corporation of Japan is also acknowledged for providing the TRS-20 instrument to UC Irvine through a research agreement with the Beckman Laser Institute.

Acknowledgements for Chapters 2 and 3: Scott Graf for performance of exercise testing, Dr. Szu-Yun Leu for statistical analysis; Robert Warren, Abraham Chiu, Newsha Dowlaty, Brian Tran and Nicole Tfaye for help with conducting measurements and data analysis. Thanks also to Drs. Shlomit Aizik and Dan Cooper for expertise in exercise physiology. Finally, thanks to ICTS nursing staff and PERC facilities for helping with studies.

Chapter 4: Joshua Cotter for conducting the study and help with analysis and manuscript writing. Thanks to Warren Reuland for help with experimental design and measurement performance. Co-authors on the published manuscript that comprises much of this chapter are Joshua Cotter, Warren Reuland, Albert Cerussi, Bruce J. Tromberg, and Pietro Galassetti.

Chapter 5: Dr. Shaista Malik for help with origination of project and continued support; Drs. Anais Leproux, Ylenia Santoro, and Thomas O'Sullivan for data analysis, interpretation and consultation. Thanks to Robert Warren for help with conducting

measurements, and to Montana Compton RN for tremendous help in coordinating research volunteers.

Mentors: Thanks to:

I would like to acknowledge Dr. Albert Cerussi for profound assistance in welcoming me into the diffuse optics group, and for rigorous teaching of optical methods and background. Dr. Ramesh Srinivasan also contributed by teaching an invaluable course on time-series analysis that allowed me to overcome fear of MATLAB. Dr. Gregory Adams for early encouragement and input on exercise studies. For demonstrating the proper way to care for both patients and research volunteers on a daily basis, I must thank Barbara Bodenofer, RN. Many of these studies could not have been done without the tireless effort and expertise in exercise physiology of Dr. Joshua Cotter, and so much credit is his as well.

I owe much of the ability to do this work to Dr. Bruce Tromberg. Through a combination of vision, patience, trust, he welcomed me into the Beckman Laser Institute to pursue research in translational biomedical optics, even though I began with little more than a fascination in the topic. I will be ever grateful for this. And finally, thanks go to my advisor, Dr. Pietro Galassetti for his consistent, unfailingly supportive mentorship and expertise over the duration of my doctoral studies. There are not many research mentors who place as much trust and confidence in their students to pursue ideas of their own, and he did this in a way that has enabled all of this work. Furthermore, his personal warmth,

friendship, and culinary skills have been vital to making the whole experience of PhD studies a time of accomplishment and joy.

Ultimately, none of this could have been done without the infinite support and patience of my wife, Ranjani. I can only hope to support her in a similar way for the rest of our lives together.

CURRICULUM VITAE

Goutham Ganesan

2008 B.S. in Biochemistry, University of Maryland,
2008-2017 MD/PhD at University of California, Irvine

FIELD OF STUDY

Biomedical optics in exercise physiology and metabolic disease

PUBLICATIONS

- **Ganesan, G**, Cotter, J, Reuland, W, Cerussi, AE, Tromberg, BJ, and Galassetti, PR. (2014). “Effect of blood flow restriction on tissue oxygenation during knee extension.” *Medicine and Science in Sports and Exercise*. E-pub 05/30/2014.
- **Ganesan, G**, Cotter, J, Reuland, W, Warren, RV, Mirzaei Zarandi, SM, Cerussi, AE, Tromberg, BJ, and Galassetti, PR. (2013). “Use of diffuse optical spectroscopy to monitor muscle and brain oxygenation dynamics during isometric and isokinetic exercise.” *Proc. SPIE 8578, Optical Tomography and Spectroscopy of Tissue X*. 857803-857813.
- Horvath, P, Oliver, SR, **Ganesan, G**, Zaldivar, FP, Radom-Aizik, S, Galassetti, PR. (2013) “Fasting glucose level modulates cell surface expression of CD11b and CD66b in granulocytes and monocytes of patients with type 2 Diabetes.” *Journal of Investigative Medicine*. 61(6) 982-987.

- Killgore, WD., Killgore, DB., **Ganesan, G.**, Krugler, AL., Kamimori, GH. (2006) "Trait-anger enhances effects of caffeine on psychomotor vigilance performance." *Perceptual and Motor Skills*. 103(3) 883-886.

ABSTRACT OF THE DISSERTATION

The use of Diffuse Optical Spectroscopy in Exercise Physiology and Metabolic Disease

By

Goutham Ganesan

Doctor of Philosophy in Pharmacology

University of California, Irvine, 2015

Professor Pietro Galassetti, Chair

While medical practitioners increasingly appreciate the importance of exercise and diet in management of metabolic disorders, there are still few clinical diagnostic tools to assess the effects of these “lifestyle” interventions. Near-infrared spectroscopy (NIRS) is uniquely suited to this purpose because it is non-invasive, non-harmful, and can be used in a variety of tissues. The purpose of these studies is to apply two techniques of NIRS: time-resolved NIRS (TR-NIRS), and frequency domain diffuse optical spectroscopic imaging (DOSI) to physiological studies in humans. The first set of studies describes the use of TR-NIRS to study incremental exercise in children and adolescents. TR-NIRS signals are used to quantify tissue-specific responses to increasing exercise intensity, as well as to determine correlation of thresholds with those occurring in ventilation data. Secondly, the effect of training is assessed by conducting cerebral TR-NIRS measurements before an 8 week training session. And finally, the paradigm of blood flow restriction exercise is investigated as a way of perturbing muscle and cerebral hemodynamics during resistance exercise.

The second portion of these studies involves the application of DOSI to the study of subcutaneous adipose tissue (AT). The role of AT in the pathophysiology of metabolic

disease is increasingly appreciated, but method to measure AT function are limited. We hypothesized that DOSI would be sensitive to changes in AT optical properties with calorie restriction, and conducted a pilot study along those lines. DOSI detected changes in both optical scattering and absorption that are consistent with known phenomena that occur in AT with weight loss, ie reduction in fat cell volume, increased O₂ extraction, and increased hydration. These findings might constitute an optical signature of AT that correlates with improvement in overall metabolism.

Taken together, these studies introduce novel contributions in the field of optical imaging in the context of obesity, metabolism and exercise.

INTRODUCTION

BACKGROUND- PHYSIOLOGY

The work and studies contained in this manuscript are motivated by an understanding of the considerable burdens imposed on individuals and society by metabolic disease. Great attention has been paid, and considerable strides have been made in the treatment of the best known consequences of metabolic disease: Type II Diabetes Mellitus (T2DM) and cardiovascular disease (CVD). Both conditions continue to have a tremendous impact on health; they are as of 2013 respectively the 7th and 1st most common causes of mortality in the United States, accounting together for approximately 27% of all deaths (1). These daunting figures notwithstanding, treatment for CVD has been improved drastically with the advent of widespread use of statins. Not only have these drugs been broadly successful at achieving lower levels of serum low-density lipoprotein (LDL) in patients, it is now clear that they possess distinct mechanisms of action that inhibit the progression of atherosclerosis directly (2).

With regard to T2DM, insulin therapy continues to be the mainstay of treatment late in the disease. Earlier stage treatments such as metformin continue to work effectively, but new drugs that work more comprehensively on disease mechanisms are reaching the clinic and continue to be developed at an encouraging rate (3). The role of health care providers in administering these treatments is clear and unambiguous, and there are rigorous standards for proper disease management in both cases (4,5). Moreover, laboratory and

imaging tests can accurately and reliably determine the stage and severity of both CVD and T2DM in individual patients.

When it comes to the pre-existing factors that lead to or prevent T2DM and CVD, however, the role of clinicians and translational researchers is less well-defined. This relative difficulty in codifying treatment standards has important consequences. The aforementioned statistics on mortality, if examined in a different light, underscore this. CVD and T2DM are often attributed as a proximate cause of death, but if the underlying causes are taken into consideration, then as of the year 2000 as many as 16.6% of all deaths (approximately 400,000)(6) are attributable to “poor diet and physical inactivity (6).” This number misses entirely the astronomical costs in quality of life and resources that result from the morbidity of these conditions. A 1999 study (7) estimated that the total health care costs related to obesity and physical inactivity were \$94 billion, or to put it another way, 9.4% of all US health spending(7). A German study attempted to quantify the lifetime additional cost incurred for those with obesity as children, and estimated a figure of € 19, 479(8). Therefore, it is clear that stronger and earlier interventions are needed to make any difference in this reality. Progress is still disappointingly slow. For those aged 2-19 in the United States, the estimated prevalence of overweight and obesity is 31.8 % (9) and unfortunately there has been no change in prevalence of obesity between the years of 2003 and 2012 (9).

There are undoubtedly many reasons why it is more difficult to make large improvements in preventative care of obesity than in treating CVD or T2DM, but two can be identified readily. Firstly, there are few robust clinical tools for predicting the pattern of progression in obesity, and any potential vascular or metabolic consequences. Such tools

might serve to reinforce the urgency of pursuing early treatment for both patients and clinicians. Secondly, the biomedical science community possesses an incomplete and overly simplistic understanding of the state of obesity and its treatment. With regard to the former, the work detailed in this document is an attempt to apply novel optical tools to serve this very purpose. With regard to the latter phenomenon, that the general understanding of obesity is incomplete is perfectly illustrated by the use of the term “poor diet and physical inactivity (6).” This simplistic view, that obesity and its treatment can be reduced to eating less and exercising more is increasingly being questioned (10). Research into the role of gut flora in determining weight and energy balance has been one reason for this questioning (11). This should also prompt a re-examination of the roles of various tissues in promoting or inhibiting the condition of obesity. To that end, the studies described in this manuscript have two distinct foci: first, the potential insights into physical fitness and exercise tolerance that can be gained by hemodynamic measurements in the cerebrum and skeletal muscles. Secondly, the response of adipose tissue (a proposed link between obesity and diabetes) to changes in metabolic state. In addressing both of these areas, these studies suggest that non-invasive tools of optical spectroscopy could potentially play a unique and important role.

Exercise and obesity

The evidence for benefits of regular exercise in the treatment of obesity and metabolic syndrome (MetS, defined as the combination of truncal obesity, a pattern of dyslipidemia, altered glucose metabolism, hypertension (12)) continues to accumulate

(12). This particular review demonstrates strong evidence for an inverse relationship between exercise training and prevalence of MetS across different populations (12). Increases in aerobic exercise are strongly associated independently with lower blood pressure in patients with hypertension (13). Increased aerobic activity has also been shown to correlate with greater insulin sensitivity in adults (14), and in children and adolescents (15). Exercise is a frontline therapy for reduction of disease risk in MetS. The evidence for these benefits is strong, and is not a point of controversy in clinical practice.

An area in which there is work to be done, however, is in the unique challenges posed by obesity and MetS to the adoption of regular exercise habits. One need not speculate to consider the unique challenges faced by obese individuals in maintaining an exercise routine. It has long been appreciated that obesity adds disproportionately to the work performed during aerobic exercise, partly due to the increased difficulty of ventilation (16). The same has been shown in obese adolescents, with an effect of elevated baseline O₂ metabolism due to increased fat mass (17).

The understanding of potential barriers to exercise is of particular importance in children with obesity, considering the potential lifetime benefits of early intervention. Investigations into this topic reveal that childhood obesity is associated with increased “body consciousness” (18), which itself may constitute a psychosocial barrier to exercise performance (18). This factor compounds existing challenges such as a lack of time, resources, or access to suitable facilities for regular exercise. There are no easy answers to overcome these barriers, but it is clear that those who would prescribe exercise in the treatment of obesity must consider these issues carefully. An open question with regard to this topic is whether there are any neurophysiological correlates with exercise intolerance

in the context of obesity. For example, might it be possible that there are brain hemodynamic or electrical signatures during exercise that reflect a lowered capacity for exercise performance, or an altered predisposition for exercise intolerance? This question will be addressed further below, and in potential follow up studies.

Additionally, while the general benefits of exercise on treatment of systemic blood pressure and insulin sensitivity have been described, there is comparatively less known about tissue-specific effects of exercise. A major goal of the following studies is to understand the effects of exercise on specific tissues (ie, skeletal muscle, brain, and fat) and the vasculature contained therein, and how these effects correlate with the known benefits of exercise. A greater understanding of these tissue-specific effects might help to fill the need for more quantitative assessments of exercise interventions in the clinic.

There is an additional benefit to exercise in the study of metabolic disease, and it is simply the fact that aerobic exercise acts as a strong physiological perturbation. Maximal exercise challenges hemodynamic, neural, endocrine and other physiological systems (19) in a strong way that might reveal subtle and otherwise undetectable deficiencies in function (20). It is this particular feature of exercise that has been taken advantage of in this set of studies to gain insight into tissue vascular function.

Therefore, in this set of studies, we have focused on the application of optical tools to study hemodynamic and metabolic responses in two tissues: the brain and skeletal muscle. What follows is additional background and rationale for conducting assessments in these tissues.

Exercise and the prefrontal cortex

The intersection of exercise physiology and neuroscience is a burgeoning field of inquiry due to improvements in imaging technology and greater understanding of neural function. A full review of this field is well beyond the scope of the current manuscript, but a focused discussion on some topics is warranted. For both methodological and hypothesis-driven reasons, the focus in this manuscript is on the role of the prefrontal cortex (PFC) in response to, and potentially in regulation of exercise performance. The methodological issue in question is the fact that the PFC is the part of the cerebrum most easily accessed by near-infrared spectroscopy (NIRS) techniques (21). The hypothesis-driven reason is that the PFC, given its neurophysiological role, might play an important role in the aforementioned issues of exercise motivation and tolerance (21).

The PFC is the area of the brain that is most highly developed in primates in comparison with lower mammals, and this increased development is thought to be part of the basis for their more complex behaviors (22). Because the PFC receives projections from most of the other cortical regions, it is thought to act as an integrating center for various sensory inputs (22). According to Miller and Cohen (p. 171), "... the PFC serves a specific function in cognitive control: the active maintenance of patterns of activity that represent goals and the means to achieve them" (22). It is this role in goal-directed behavior that makes the PFC a worthwhile area of inquiry in exercise. One might hypothesize that in conditions in which barriers to exercise predominate, there might be alterations in the PFC response to exercise, reflecting a diminished ability to accomplish goal-directed behavior. This may be especially true in common exercise testing paradigms such as maximal aerobic

capacity (VO_2 max) testing, where the decision to cease exercise occurs when the sensory inputs to the brain driven by fatigue overwhelm any central nervous system effort to maintain performance (23).

According to one line of inquiry, exercise is associated with an increase in PFC EEG amplitude in the alpha band, indicating a reduction in activity (24), and therefore a relative “hypofrontality” (24). It is hypothesized that this reduction in activity might be associated with the psychological benefits of exercise, such as reduced anxiety (24). Perhaps paradoxically, higher levels of physical training have been shown to correlate with larger PFC volumes in humans (25). This may be important as functions governed by the PFC are those that tend to more commonly show degradation with age (25).

Detailed studies of electrophysiology during vigorous exercise are difficult for a variety of reasons – development of sweat, movement and scalp muscle artifacts, and difficulty in localizing regional activity in the PFC among them, and so other techniques have been employed. Indeed, there is a substantial literature on the use of NIRS to measure hemodynamics in the PFC during a variety of exercises, and therefore this is not a novel application in and of itself. The interest in NIRS for this purpose is because it is sensitive to metabolic changes that reflect coupling of hemodynamics to underlying neural metabolism. NIRS measurements of Oxyhemoglobin have been shown to correlate with the fMRI BOLD signal that reflects local cerebral metabolism (26). Additionally, there is the observation that regional changes in cerebral blood volume may have value in prediction of positive neural outcomes (25).

Specific experimental aims for each of the studies described here are detailed in those respective chapters. However, there are several broad questions that are being explored:

1. Does the use of diffuse optical spectroscopy, by quantifying changes in optical scattering and path length, improve the measurement of cerebral hemodynamics in comparison with continuous wave NIRS?
2. Do measures of cerebral hemodynamics correlate systematically with ventilatory measures of performance?
3. Do patterns of cerebral dynamics correlate with or influence the sensation of fatigue in exercise?
4. Do parameters of cerebral oxygenation during acute exercise respond to changes in aerobic fitness?

These questions will be addressed in detail in chapters 1-4 of this manuscript.

Skeletal muscle physiology and metabolic disease

As the primary organs involved in any type of exercise, it is not surprising that muscle physiology determines aspects of overall metabolic health. At the most basic level, skeletal muscle is of prime importance as a site of insulin-dependent glucose uptake. By

this fact alone, one would expect skeletal muscle health to play an important role in the treatment of obesity and MetS. Indeed, it has been demonstrated in both animals and humans that there is a causative link between the deposition of triglycerides in skeletal muscle and the development of insulin resistance (27). Even acute administration of intravenous fatty acids can induce short-term insulin resistance by inhibition of insulin-dependent glucose uptake in the muscle (28). It appears that the mechanism is partly through the accumulation of diacylglycerol (DAG) in myocytes, which acts as an activator of protein kinases that blunt the response to insulin (28). Beyond the basic effect of increased muscle energy expenditure in exercise, there are other mechanisms that might explain the insulin sensitizing effect of exercise in the muscle. For example, acute elevations of the cytokine IL-6 in response to aerobic exercise might enhance lipolysis within the skeletal muscle (28). IL-6 can also be classified as a “myokine,” that is a cytokine released from contracting muscle. There have also been other myokines characterized, such as IL-13, IL-15, and irisin that contribute to increased substrate metabolism, and therefore greater insulin sensitivity (29). As described previously, there is no doubt that aerobic exercise is beneficial in treatment of MetS, regardless of whether it causes weight loss.

It is more difficult to draw conclusions about the effect of resistance training in patients with obesity or MetS, mostly because considerably fewer studies are done to investigate this. The evidence seems to suggest that resistance training does enhance glucose uptake and insulin sensitivity in the muscle, but that this effect is likely limited to the muscle being trained (30). Furthermore, there is some evidence that suggests the presence of insulin resistance itself attenuates the insulin sensitizing effect of resistance training (30). Despite this ambiguity, there is strong evidence that resistance training can

help to preserve lean body mass in conjunction with weight loss in a hypocaloric diet (31). This would serve to maintain energy expenditure and potential act synergistically to improve insulin sensitivity. However, similar to aerobic exercise, obesity presents unique barriers to the performance of resistance training. Additionally, there is much ambiguity about what types of resistance training can maximize the benefit in obesity and MetS (32).

To this end, new methods of studying muscle function and composition, are needed. Existing methods are either functional (e.g., measurements of strength, range of motion), or involve expensive imaging modalities such as MRI which are difficult to use dynamically. None of the established methods can determine without biopsy the relative oxidative capacity of the muscle, or levels of water and lipid content. Therefore, in this set of studies, diffuse optical imaging and spectroscopic methods have been used in an attempt to better understand muscle function in response to both aerobic and resistance exercise.

The role of adipose tissue

Much of the most compelling recent work in the pathophysiology of insulin resistance has come from studies of adipose tissue (AT). AT encompasses both subcutaneous fat tissue as well as visceral fat surrounding the internal organs. Rather than being a passive site for storage of excess dietary lipids, AT has been conclusively shown to be an important endocrine organ and a regulator of metabolism. This was perhaps most convincingly shown by the characterization of the ob/ob knockout mouse (33). The loss of

this gene in mice led to a dramatically obese and insulin resistant phenotype (33). The ob gene was later discovered to code for the peptide hormone Leptin, which is produced by adipocytes and acts by various mechanisms in controlling appetite and body weight (34).

Since the discovery of leptin and leptin resistance, several other adipokines have been identified, the most studied being adiponectin and resistin. Adiponectin has been shown to have an insulin-sensitizing effect, whereas resistin has shown the opposite activity (35). In one cohort of obese and control subjects, insulin resistance (measured by HOMA-IR, an index of fasting circulating glucose and insulin concentrations) was correlated to the circulating levels of resistin and leptin (35). More recent evidence suggests that circulating levels of adiponectin are protective against progression of metabolic disease, and correlated with lower levels of inflammation and insulin resistance (36). The insulin-sensitizing effects of adiponectin seem to be due to increased hepatic and skeletal muscle activity of AMP-Kinase (AMPK), enhancing glucose uptake and beta oxidation of fatty acids (36). Adiponectin also seems to have anti-atherosclerotic activity by various effects on macrophages and cytokine production (36).

The relationship between AT and insulin resistance might involve even more fundamental properties than endocrine secretions. As early as 1971, it has been observed that there is a correlation between circulating insulin levels and the size of adipocytes (37). This observation has received new attention in recent years, and has been repeated in a variety of populations (38,39). The average size of both subcutaneous and visceral adipocytes is increased in obesity and has been shown to decrease even with moderate weight loss (40). The likely mechanism for this relationship is that larger adipocytes result in poorer oxygenation of mitochondria within them, and therefore a state of hypoxia. This

hypoxia causes induction of hypoxia inducible factors (HIFs) which are known to be involved in the development of chronic inflammation and insulin resistance (41). This phenomenon is discussed in greater detail in chapter 5, but it is becoming clear that adipocyte size may be a useful biomarker in the assessment of metabolic disease.

As implied by the above connection between adipocyte size and poor oxygenation, the vascularization and blood supply of AT is also increasingly recognized for relevance to metabolic disease. Because of the constant remodeling that AT undergoes with changes in energy balance, it experiences a high level of baseline angiogenesis, even though the vascular fraction is still low in comparison with more metabolically active tissues (42). Studies in humans have found that obesity is accompanied by reduced vascularization of AT, which actually seems to be associated with elevated O_2 tension and inflammation (43). This inflammation typically leads to macrophage infiltration, cytokine release, and the previously discussed effects of increasing insulin resistance (44).

What is missing in the study of AT biology as it relates to metabolic disease is a set of methods for non-invasively assessing AT in humans. This is important because AT in humans is in many ways fundamentally different than in most mammals, where there are persistent depots of “brown” thermogenic AT (45). To date, methods of studying AT physiology have included skin surface measurements of impedance (46), PET imaging with FDG (47), and MRI/MRS (48). It is a major contention of this manuscript that diffuse optical spectroscopic techniques may play an important role in the imaging and characterization of AT physiology in humans, and preliminary data in support of this are extensively described in chapter 5.

BACKGROUND- DIFFUSE OPTICAL SPECTROSCOPY

The unifying theme of all the subsequent studies described is a methodological one – the use of tissue spectroscopic and imaging technologies that fall under the category of diffuse optical spectroscopy (DOS). These techniques allow for the quantitative near-infrared spectroscopy (NIRS), and are able to quantify the bulk optical properties of biological tissues. An understanding of DOS requires some basic theory of NIRS, and thus there will be a brief discussion of this topic.

Near-infrared spectroscopy – theory and history

In its most basic form, near-infrared spectroscopy (NIRS) refers to quite the same method as chemical analysis techniques done using visible and UV light in cuvettes, just using light from a longer part of the electromagnetic spectrum (49). Like any such method, NIRS makes use of the Beer-Lambert law, which relates the path length of light through a sample and its absorption coefficient to the level of attenuation of an incident light source, as follows:

$$E_o = E_i(e^{-\mu_a d}) \quad (50)$$

Near-infrared (NIR) light (typically 650 – 1000 nm, with some extension into longer wavelengths) has properties that allow it to be used for spectroscopic analysis of biological

materials, where light of shorter wavelengths would be absorbed to much too high a degree. Most importantly, NIR light is absorbed minimally, and can therefore penetrate several centimeters into most tissues (51). Most biological tissues, unlike clear solutions in cuvettes, are multiple scattering media with respect to NIR light. This and the fact most tissue NIRS measurements are done using a reflectance geometry necessitate corrections to the basic Beer-Lambert law for quantitative spectroscopy. With these additional terms, a modified Beer-Lambert law can be derived (52). This modified form contains a term called the differential path length factor, which describes the mean distance travelled by photons through the tissue, and is dependent on the absorption and scattering properties of the propagation medium (50). Finally, with measured absorption coefficients at discrete NIR wavelengths, and known molar extinction coefficients (53), relative concentration changes in Oxyhemoglobin (HbO₂), deoxyhemoglobin (HbR), and in some cases cytochrome c oxidase (54).

The earliest applications of continuous wave NIRS in humans involved studies of brain metabolism and oxygenation state since the brain, among tissues accessible under the surface, is uniquely sensitive to O₂ deprivation (54). Britton Chance, one of the pioneers of both benchtop and applied spectroscopy methods (49), pioneered the use of NIRS to study muscle responses to perturbations in blood flow and oxygenation (55). The early NIRS methodologies made use of what are known as continuous wave (CW) light sources; that is, emitted at a constant frequency and amplitude. These techniques will be subsequently referred to as CW-NIRS, and have been applied in numerous variations to study many human tissues. In the brain, functional NIRS (fNIRS) has become an increasingly important tool to monitor event-related hemodynamic responses in the

cerebral cortex, applied in a wide range of cognitive and neurological experimental paradigms (56). fNIRS systems now typically make use of an array of “optodes” or optical channels to make simultaneous measurements in multiple areas of the brain (56). CW techniques such as fNIRS have important desirable attributes; firstly, their relatively simple hardware allows for very fast sampling of data, as well as a relatively low cost. Additionally, these instruments tend to be easily integrable with other tools of physiology, such as EMG or EEG electrodes (57) . Despite their widespread use, there are some crucial limitations on the quantitative power of CW-NIRS methods, and thus there is in certain situations a need for more a more rigorous optical approach, as will be described in the next section.

Diffuse Optical Spectroscopic (DOS) techniques

The principal limitation of CW-NIRS devices is the inability to quantify hemoglobin concentrations accurately. This inability is due to the lack of information obtained about photon path length due to the use of constant frequency and amplitude light (57). In order to obtain such quantitation, methods capable of addressing the fundamental equations that govern light-tissue interactions are required. Biological tissues are described as turbid media with regard to the propagation of light through them; that is, scattering of light is much more predominant than absorption. Therefore, light transport in tissue can be understood as being analogous to the diffusion of heat, and therefore can be assessed using a diffusion equation (58). The diffusion equation, according to Yodh and Chance (58), can be formulated as follows, assuming a homogenous medium:

$$\nabla D \nabla U(\mathbf{r}, t) - v \mu_a U(\mathbf{r}, t) - \frac{\partial U(\mathbf{r}, t)}{\partial t} = S(\mathbf{r}, t)$$

Here, the function $U(\mathbf{r}, t)$ represents the optical energy density at position \mathbf{r} and time t . $S(\mathbf{r}, t)$ represents the source terms at position \mathbf{r} and time t and v represents the speed of light in the medium. The term D is the diffusion coefficient, which depends upon the reduced scattering coefficient (μ_s') and the absorption coefficient (μ_a) in the medium (58). This is the critical piece of information is that the diffusion of light is dependent on optical scattering and absorption properties of the medium. These properties, if solved for, can be used to quantify path length and hemoglobin concentrations in tissue (57). The absorption coefficient is due to the concentration of absorbing chromophores in the medium, whereas the scattering coefficient is partially dependent on the density of spherical objects in the medium of a size roughly comparable to the optical wavelength, in this case ~ 1 micron (58). This would include organelles such as mitochondria, etc (59).

There are two primary mathematical and technological approaches to solving this equation, and these two methods form the foundation of existing DOS technologies (58). Both approaches (time-domain and frequency domain) are employed in the following studies and will be described further.

Time domain approach to DOS

The time-domain approach relies on the basic premise that the detected profile of a reflected optical pulse of very short duration will predictably contain information about the

scattering and absorption properties of the propagation medium (60). Early experimental work showed that experimental detected pulses did match quite well with predicted signals based on analytic and statistical methods (60). The detected profile of an incident short pulse is referred to as a temporal point-spread function (TPSF), and an example is shown in figure 1.1.

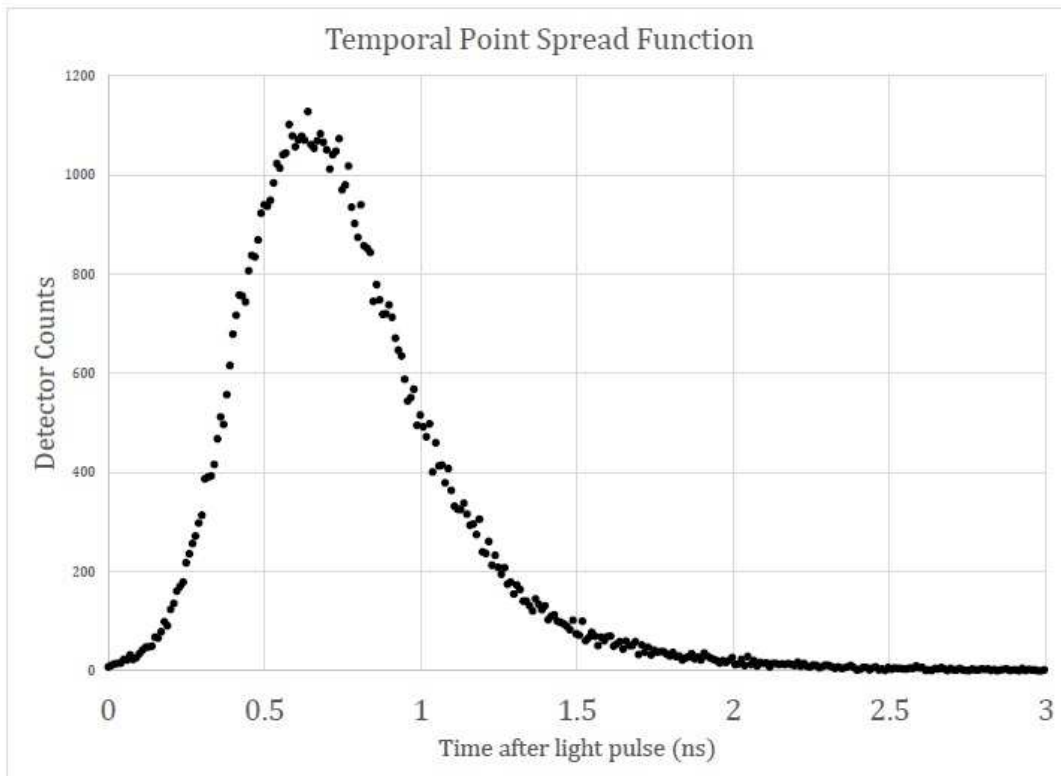


Figure 1.1 Sample temporal point spread function: An example of a detected TPSF obtained from the TRS-20 time-resolved NIRS system. This signal was obtained from a measurement of cerebral oxygenation using a source-detector separation of 3 cm. The x-axis represents time after the initial light pulse in nanoseconds, whereas the y-axis is the number of detected counts by the photomultiplier tube. These TPSF curves contain information about tissue optical properties when analyzed in conjunction with a calibration accounting for instrument function.

While the theoretical foundations for time-resolved DOS have been established for a long time, it has only recently become possible to create clinic-ready measurement devices to perform measurements in humans. This is because TR-NIRS systems require sophisticated electronics to control the width in time of incident light on the picosecond scale, as well as very fast, and therefore expensive, detectors to resolve the full TPSF. In this manuscript, the TRS-20 device for performing TR-NIRS has been employed (Hamamatsu Photonics KK, Hamamatsu, Japan). All subsequent descriptions and TR-NIRS data will refer to this specific instrument. The TRS-20 instrument uses two independent measurement channels, and light pulses of three wavelengths (760, 795, and 830 nm) along with photomultiplier tubes (PMTs) for detection (61). Fiber-optics cables connect the instrument to silicone-based probes that can be placed on the skin surface to measure the desired tissue. Typically, many TPSFs are summated over a long interval (5 seconds) to achieve an adequate signal to noise ratio (62). It has been demonstrated that in addition to providing quantitation of optical properties as described above, the TRS-20 also allows for greater penetration depth when compared with CW-NIRS devices, and therefore better resolution of deeper tissues, at least with regard to cerebral tissue (62). Detected TPSF curves from tissue are convolved with a calibration for instrument function (62), usually obtained by direct detection of the incident pulse through air with no intervening tissue. The normalized TPSF is fitted to a prediction of the diffusion equation, and μ_s' and μ_a at the three wavelengths are obtained, and subsequent calculation of tissue concentrations of oxyhemoglobin ([HbO₂]), deoxyhemoglobin ([HbR]), and total hemoglobin ([THb]) (61). Additionally, the oxygen saturation (stO₂) can also be calculated, which is simply the ratio of [HbO₂]/[THb]. When used to make continuous recordings, event markers can be placed

in the data to indicate transitions between activities or the occurrences of anomalous events. Additionally, there is an analysis mode that allows for the re-processing of data such that the scattering coefficients can be assumed as fixed from their initial values. This mode, called “fitting-and-change” (FAC) allows for the assessment of the effect of scattering changes over the course of a measurement. The default mode, in which each TPSF is fitted to the diffusion equation is referred to as fitting all data, or FAD if specification is necessary. The TRS-20 is capable of measuring at various source-detector separations on the skin surface, but in the subsequent studies only separations of 3 cm and 4 cm have been used. Further details of implementation of TRS-20 for individual studies are contained in the respective methods sections of those chapters.

Frequency-domain approach to DOS

As opposed to the time-domain approach, which uses very short pulses of light, the frequency domain photon migration (FDPM) to DOS employs light sources whose intensity is modulated in time, in order to generate photon-density waves whose propagation in tissue is dependent on the optical properties of the diffusion equation (63). While there are several methodological approaches to FDPM, the one that will be discussed in this work is the use of single source-detector pair modulated and many frequencies. This is the fundamental approach of the Diffuse Optical Spectroscopic Imaging (DOSI) technology developed at the Beckman Laser Institute UCI over the past 2-3 decades (63). The first iteration of this DOSI system involved the placement of a fiber-coupled light source and avalanche photodiode (APD) detector on the tissue surface. Just as in the case of time-

domain measurements, these measurements are conducted using a reflection geometry and the assumption of a semi-infinite medium (63). The light sources are laser diodes of discrete NIR wavelengths whose power is modulated by a network analyzer which sweeps through a range of frequencies up to 1 GHz. For each frequency of incident light, there is a corresponding phase shift and amplitude detected after passage through the tissue, and these parameters at all incident frequencies can be used to solve for μ_s' and μ_a at each wavelength (63). This approach to FDPM was used in early studies to quantify optical properties cancerous tissues with accuracy (64).

The current generation of FDPM technology makes use of a dramatically smaller unit that performs the frequency-sweep functionality without a network analyzer, and uses four laser diode sources: 660 nm, 690 nm, 780 nm, and 830 nm (65). In figure 1.2, an example of an FDPM measurement is shown, with amplitude and phase fitting at each of four wavelengths. These phase and amplitude measurements must be calibrated using measurements of solid tissue-simulating phantoms of known optical properties in order to derive tissue optical properties (63).

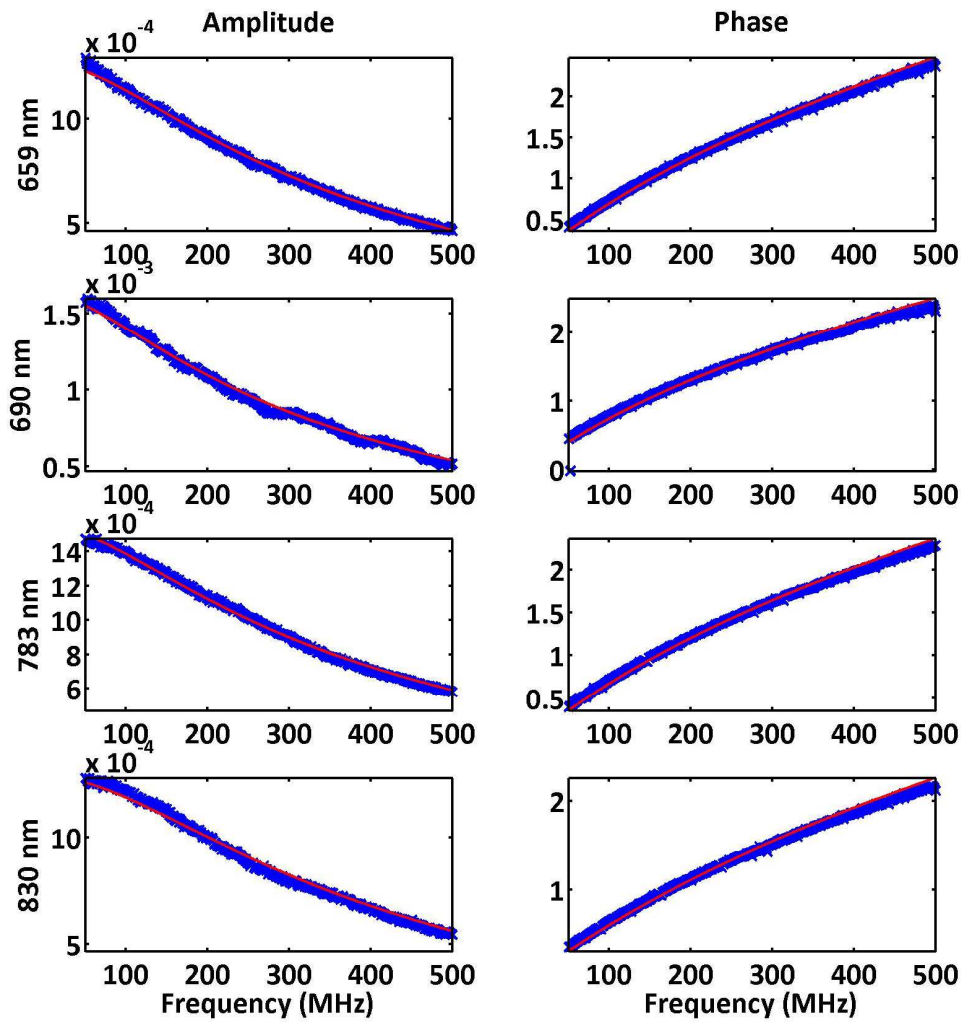


Figure 1.2 Sample FDPM phase and amplitude: A sample of an FDPM measurement taken from a human abdomen. The left column shows the raw (blue) and fitted (red) detected amplitude at each modulation frequency (x-axis) at all four laser diode wavelengths. The right column shows the same for the phase shift. Note that at higher modulation frequencies, detected amplitude declines while the phase shift increases. The red fitted curves are used to calculate optical properties from the diffusion equation.

An additional component critical to the studies detailed in this work is broadband reflectance spectroscopy. From a technical standpoint, this is extremely simple to do. It involves the use of a broadband white light source, and any commercially available spectrophotometer. By measuring the spectrum of the reflected light, the relative attenuation of light can be assessed as a function of wavelength. However, if this broadband reflectance is anchored to quantitatively determined tissue optical properties, those properties can be extrapolated for the whole range of wavelengths measured, usually 650-1000 nm (66). The process involves fitting a power-law curve to the FDPM scattering coefficients based on Mie theory(67), and then fitting the broadband reflected light profile to the known absorption coefficients, as shown in figure 1.3.

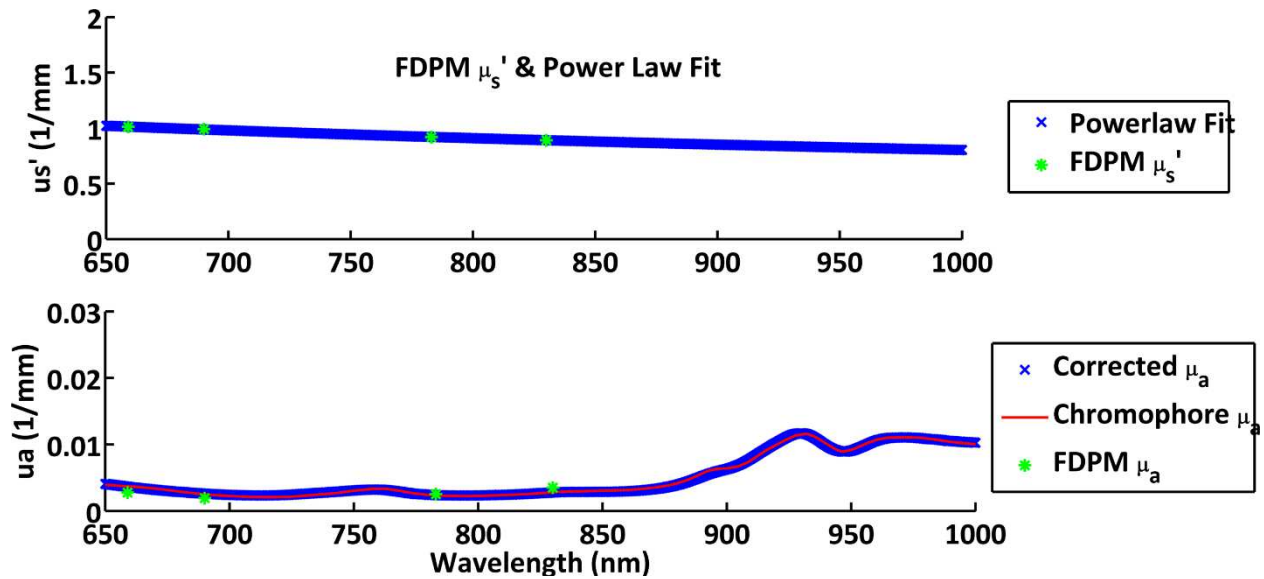


Figure 1.3: sample ssFDPM fits: Sample broadband scattering (top) and absorption (bottom) fits using combined FDPM and broadband approach of DOSI. Using this method, precise tissue concentrations of oxyhemoglobin, deoxyhemoglobin, water and lipid can be quantified.

The advantage of combining the two modalities is the great increase in spectral information content. Rather than only 4 wavelengths of data to calculate concentrations, it can now be done with 350 wavelengths. This also allows for highly sophisticated spectral analyses, and for potential characterization of other absorbing species (68).

The combined FDPM and broadband approach is integrated into a single instrument classified as Diffuse Optical Spectroscopic Imaging (DOSI), and has been used extensively especially in the fields of breast cancer (69-71). Using grids of measurements on a the tissue of interest, sparse images can be created to visualize the distribution of optical or physiological properties, and hence the imaging component of the technique (72). The specific details of the implementation of DOSI are included in the methods section of chapter 5, where the technique is primarily used.

Concluding remarks

With the groundwork of biomedical science and the basics of the technology described, the remainder of this manuscript is devoted to the specific applications of the tools previously described to various studies in humans. The ultimate aim of all of these studies is to improve our understanding of the regulation of hemodynamics and metabolism in tissues during physiologically relevant perturbations. Therefore, the focus is on specific tissue responses to exhaustive exercise, and in chapter 5, calorie restriction. While the two perturbations are fundamentally different, the aim of these studies is similar in the sense that the meaning and import of the recorded DOSI signals is sought, not simply the technical achievement of conducting the measurements. In the more distant future, it is

hoped that DOSI and related techniques will play a greater role in day-to-day clinical medicine. Their ease-of-use, relatively low cost, and novel information content make them particularly attractive for this purpose.

CHAPTER 2: Brain and muscle oxygenation during incremental exercise in male adolescents

RATIONALE

Cardio-pulmonary exercise testing (CPET) is frequently used as a research and clinical tool to assess fitness or exercise limitation in a variety of populations, often with concomitant measurements of gas exchange. The information gained from CPET can be enhanced by simultaneous measures of regional tissue oxygenation using near-infrared spectroscopy (NIRS), a technique capable of assessing hemoglobin (Hb) content and oxygenation in a variety of tissues. Indeed the combination of CPET and measurement of regional tissue oxygenation through NIRS is proving to be an increasingly powerful tool in identifying limitations of exercise capacity in both adults and children in health and disease (73,74). Among the basic physiological applications for NIRS measurements in skeletal muscles are the study of muscle oxygen uptake kinetics in relation to pulmonary function (75-77), modeling changes in skeletal muscle blood flow (78,79), and assessment of muscle fatigue(80). Additionally, neurological responses to exercise can also be non-invasively studied with NIRS, with the goal of understanding cerebral vascular regulation (81), or elucidating central mechanisms governing exercise performance (21). There is still relatively little known about these central mechanisms in children, and their potential role in regulating motivation and perceived exertion.

While techniques such as NIRS are an appealing adjunct to CPET, particularly in children because they are noninvasive and safe, there are many outstanding issues that

must be addressed with regard to different NIRS approaches, as well as data interpretation. For example, the impact of changes in tissue scattering and optical path length in the context of exercise has not been fully investigated. Additionally, there remains much work to be done in describing NIRS signals in the context of pulmonary gas exchange measurements beyond $\dot{V}O_2$. Finally, the degree to which Hb oxygenation dynamics reflect underlying O_2 availability and blood flow, respectively, is unclear.

Published NIRS studies typically employ continuous wave (CW-NIRS) devices, whose main limitation is the inability to account for changes in tissue optical scattering. Assessment of scattering coefficients (μ_s') and path length (PL) is necessary for quantitative assessment of Hb content and oxygenation. There are several modified NIRS approaches capable of measuring these quantities, collectively known as diffuse optical spectroscopy (DOS) techniques. One such approach is time-resolved spectroscopy (TR-NIRS). In contrast to CW-NIRS, TR-NIRS involves emission of ultra-short (100 ps) pulses of light into a tissue of interest, and subsequent detection on the surface of the tissue at a fixed distance. As the short pulse travels through tissue and is subjected to multiple scattering, its detected profile broadens. This temporal point-spread function (TPSF) can be used to calculate both tissue photon PL, and ultimately absorption coefficients (μ_a) and μ_s' . This is done by modeling the tissue using the diffusion approximation, a technique which has been described thoroughly elsewhere (60). These values, along with known molar extinction coefficients, are then used to calculate concentrations of oxyhemoglobin ([HbO₂]), deoxyhemoglobin ([HbR]), and total hemoglobin ([THb]) using the Beer-Lambert law. From these, oxygen saturation is also calculated (stO_2 , [HbO₂]/[THb]).

In this study we used TR-NIRS to study oxygen saturation and hemoglobin concentrations during exercise in quadriceps (vastus lateralis, VL) and prefrontal cortex (PFC) in a group of healthy male children and adolescents with varying ages and fitness levels. Our objectives were: 1) To examine average absolute oxygen saturation (stO₂) and hemoglobin concentrations, as well as changes in optical scattering and path length at several stages of exercise and recovery and 2) to study TR-NIRS kinetics during exercise to determine if there are any correlations between the two tissues, or correlations between tissue oxygenation and pulmonary gas exchange dynamics.

METHODS

Exercise Studies

Eleven male children and adolescents (Average age 15.3, range 10.4 – 17.5) were recruited for the study. In each case, a parent provided written informed consent for participation, and each child provided assent. Studies were conducted in the early to mid-afternoon in the UC Irvine Pediatric Exercise Research Center under the supervision of an exercise physiologist. After vital signs were measured and evaluation for contraindications to exercise was performed, each subject rested for 15 minutes. Subjects were placed and fitted on a stationary cycle, and were told to remain still for several minutes. EKG leads and a mouthpiece for expired gas collection were placed and connected to a metabolic cart system (Sensormedics) for breath-by-breath pulmonary gas exchange. This was followed by a three minute unloaded warm-up, during which baseline pulmonary, cardiac, and

optical data were recorded. Based on age, height, weight, and activity level each subject underwent either a 15-W or 20-W per minute incremental protocol. Each subject was instructed to maintain a cycling rate of 60-80 revolutions per minute, as indicated on the ergometer display. At the point of volitional exhaustion or reduction of cycling speed below 45 rpm, resistance was reduced to zero, and subjects were asked to continue unloaded pedaling for three minutes after momentarily stopping. Finally, at 3 minutes post-exercise, subjects were asked to stop pedaling, and optical measurements continued for 3 additional minutes.

TR-NIRS Measurements

The dual channel TRS-20 instrument (Hamamatsu Photonics, Japan) was calibrated using fixed-distance cylinders for measuring instrument function, after an initial warm-up period. During rest on the cycle, optical probes were placed superior to the left PFC, as close as possible to the hairline, and lateral so as to avoid measuring over cerebral sinuses(82). The second channel probe was placed on the VL muscle on the anterolateral aspect of the thigh, midway between the anterior superior iliac spine and the patella. The source-detector separation used was three cm, and data was recorded every 3 seconds. Both probes were secured to the skin using double sided adhesive, and an elastic headband was used to limit motion and ensure proper contact on the forehead probe. Using the TRS-20 software, data were processed by fitting to the diffusion approximation with mean photon path length (PL) to calculate scattering (reduced scattering coefficient, μ_s') and absorption (μ_a) at each measurement point and for each wavelength. These values were

then used to calculate absolute concentrations of $[HbO_2]$ and $[HbR]$, and $[THb]$. Using these values, oxygen saturation is also calculated (stO_2 , $[HbO_2] / [THb]$). Values for PL and μ_s' at the 796 nm wavelength were also analyzed over the course of incremental exercise to determine if these parameters changed significantly.

Data Analysis

First, TR-NIRS parameters ($[HbO_2]$, $[HbR]$, $[THb]$, stO_2 , PL, and μ_s' at each stage were calculated by averaging 20 seconds oxygenation data from TRS-20 control software at baseline (BL), unloaded pedaling (UP), and incremental exercise (20% (E20), 50% (E50), 80% (E80), peak work rate (PK), 2 minutes post (PT2), and 5 minutes post (PT5)) for each subject. μ_s' , due to lower signal-to-noise ratio, was analyzed only at three time points: BL, E50, and PK. The linear mixed model (LMM) was used to evaluate differences in TR-NIRS parameters among the 8 exercise/recovery stages (3 for μ_s') and the repeated measurements were modeled with unrestricted covariance structure. *Post hoc* pairwise comparisons between all exercise stages were performed and p-values were adjusted using Bonferroni's method. The mean level, standard error (SE), and corresponding 95% confidence interval (CI) were all obtained from the LMM. This analysis was performed using SAS 9.4 (Cary, NC) and the significance level was set at 0.05. Then, correlation between the gas-exchange measurements (HR, V_{O_2} , V_{CO_2} , VE, PET_{O_2} , and PET_{CO_2}) and TR-NIRS measurements ($[HbO_2]$, $[HbR]$, $[THb]$, and stO_2) were assessed by Pearson's correlation between pairs of variables during the entire course of exercise for each subject.

Next, the slope-change or threshold events in gas exchange and TR-NIRS data were identified using a piecewise regression method. TR-NIRS thresholds were characterized in PFC [HbO₂] (a change to negative slope late in exercise), PFC [HbR] (a change from steady-state to positive slope), and VL [THb] (change to steady-state or decline). For gas exchange data, VE and PET_{CO2} were used to identify the second ventilatory threshold in each test using the same piecewise method. This was done using a tool called Shape Language Modeling (SLM, D'Errico, John. (2009) Shape Language Modeling.

<http://www.mathworks.com/matlabcentral/fileexchange/24443>. Retrieved 2/19/2013).

Prior to regression analysis, each data set was also filtered using a moving window Hampel Filter to remove outliers, defined as points more than 2.5 standard deviations (SD) away from the mean of the window (Outlier Detection and Removal, Nielsen, Michael Lindholm.

(2012)). [http://www.mathworks.com/matlabcentral/fileexchange/34795-outlier-](http://www.mathworks.com/matlabcentral/fileexchange/34795-outlier-detection-and-removal-hampel)

[detection-and-removal-hampel](http://www.mathworks.com/matlabcentral/fileexchange/34795-outlier-detection-and-removal-hampel) . Retrieved 3/15/2013). Then, all data sets were smoothed

using a robust loess method with a span of 9 measurements. The SLM tool was used to obtain for each tracing piecewise linear fits, with the output being the overall goodness of each fit (adjusted R-squared) and the position in time of the slope changes, or

“breakpoints,” as determined from an initial guess by visual inspection and iteratively calculated to achieve the optimal adjusted r-squared value. These detected breakpoints in gas-exchange data and TR-NIRS measurements were expressed as a fraction of time to peak work rate achieved. The relationship of threshold time between gas-exchange measurements and TR-NIRS measurements were then evaluated using the Pearson's correlation.

Effect of changes in scattering

To assess the effects of scattering changes on computed chromophore concentrations, direct comparison was made between fitting all data (FAD), or default fitting mode with the fitting and change (FAC) mode, in which scattering coefficients were assumed to be fixed from the initial values obtained at baseline. For individual subjects, the FAD and FAC data were plotted to visualize potential differences, and for group averages, these were analyzed by two-way repeated measures ANOVA.

RESULTS

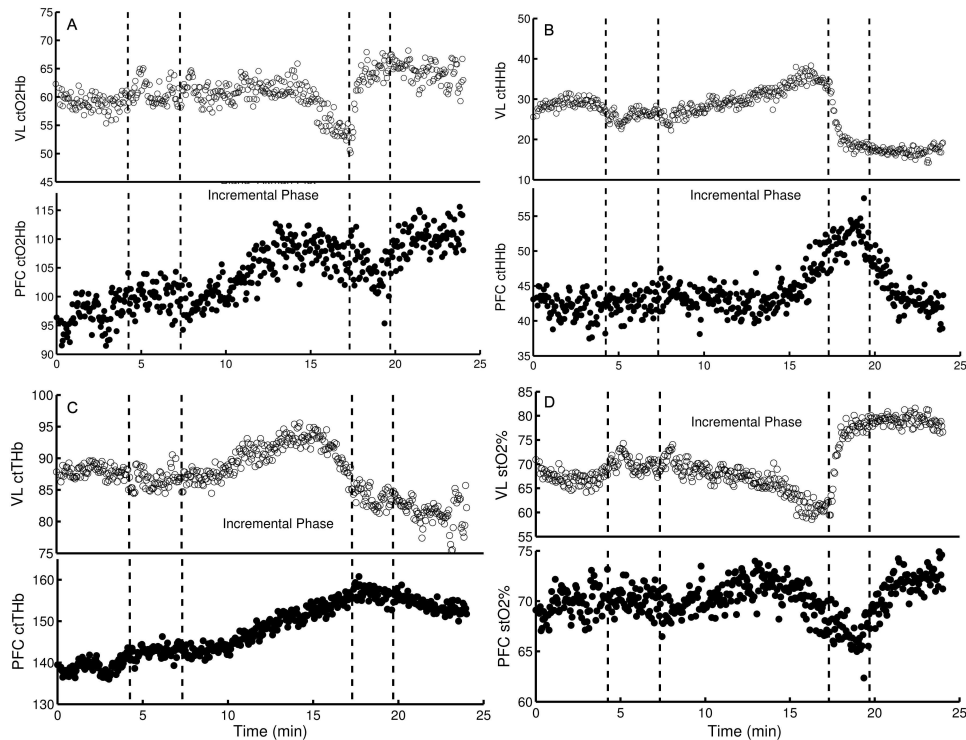


Figure 2.1: Sample tracings in PFC and VL(A) - (D) show representative tracings for absolute [HbO₂], [HbR], [THb], and stO₂ respectively in one subject. Vertical dashed lines delineate stages of exercise (Baseline, unloaded pedaling, incremental phase, recovery pedaling, and full rest). Within each plot, hollow circles denote traces from VL, while filled circles are from PFC.

Figure 2.1 shows example tracings in both PFC and VL for all TR-NIRS variables.

Figure 2.2 shows means and 95% CIs for all 11 subjects at the 8 averaged stages: baseline, unloaded pedaling, 20, 50, 80 and 100% of peak effort, and 2 and 5 min post (BL, UP, E20, E50, E80, PK PT2, and PT5, respectively).

Exercise caused a significant increase in PFC [HbO₂] over BL at E80 (Fig. 2.2A, E80 – BL = $6.33 \pm 0.96 \mu\text{M}$, adj.*p* = 0.0017), as well as a significant and persistent increase in [HbR], which was largest at PT2 (Fig. 2.2B, PK-BL = $5.85 \pm 1.36 \mu\text{M}$, adj.*p* = 0.044; PT2-BL = $7.98 \pm 1.18 \mu\text{M}$, adj.*p* = 0.0014). PFC [THb] began to increase after E50, and remained

elevated through recovery (Fig. 2.2C, E80-E50= 5.28 ± 0.67 μM , adj. $p = 0.0004$; PT2-BL= 12.29 ± 2.19 μM , adj. $p = 0.0062$). The saturation stayed the same until 80% of peak work rate and then showed a significant drop at PK (Fig. 2.2D, PK-E80= -2.95 ± 0.53 μM , adj. $p = 0.0064$), and it remained significantly lower than BL until PT2 (PT2-BL= -3.79 ± 0.62 μM , adj. $p = 0.0034$).

VL [HbO_2] displayed a slight, non-significant decrease during exercise, then increased rapidly in recovery hyperemia (Fig. 2.2E, PT2- PK = 13.04 ± 2.03 μM , adj. $p = 0.0021$). VL [HbR] increased significantly in the middle stages of exercise, reached a plateau between 80% and peak exercise, and decreased to sub-baseline levels during recovery (Fig. 2.2F, E80-UP= 8.01 ± 1.28 μM , adj. $p = 0.0026$; PT2 - PK= -12.06 ± 2.06 μM , adj. $p = 0.0044$; and PT5 - BL= -7.16 ± 1.64 μM , adj. $p = 0.039$). VL [THb] increased significantly from UP to E80, then dropped slightly until peak exercise (Fig. 2.2G, E80-UP= 6.99 ± 0.84 μM , adj. $p = 0.0002$). VL stO_2 decreased significantly from UP and E20 to E50, E80 and PK ($p < 0.034$), with differences ranging from the smallest E50-E20= -2.99 ± 0.44 μM to the largest PK-UP = -6.84 ± 1.35 μM . stO_2 then increased significantly at PT2 and PT5 above all other stages (adj. $p < 0.0012$) with the difference ranging from the smallest PT2-UP= 6.17 ± 0.82 μM to the largest PT5-PK= 13.49 ± 1.67 μM .

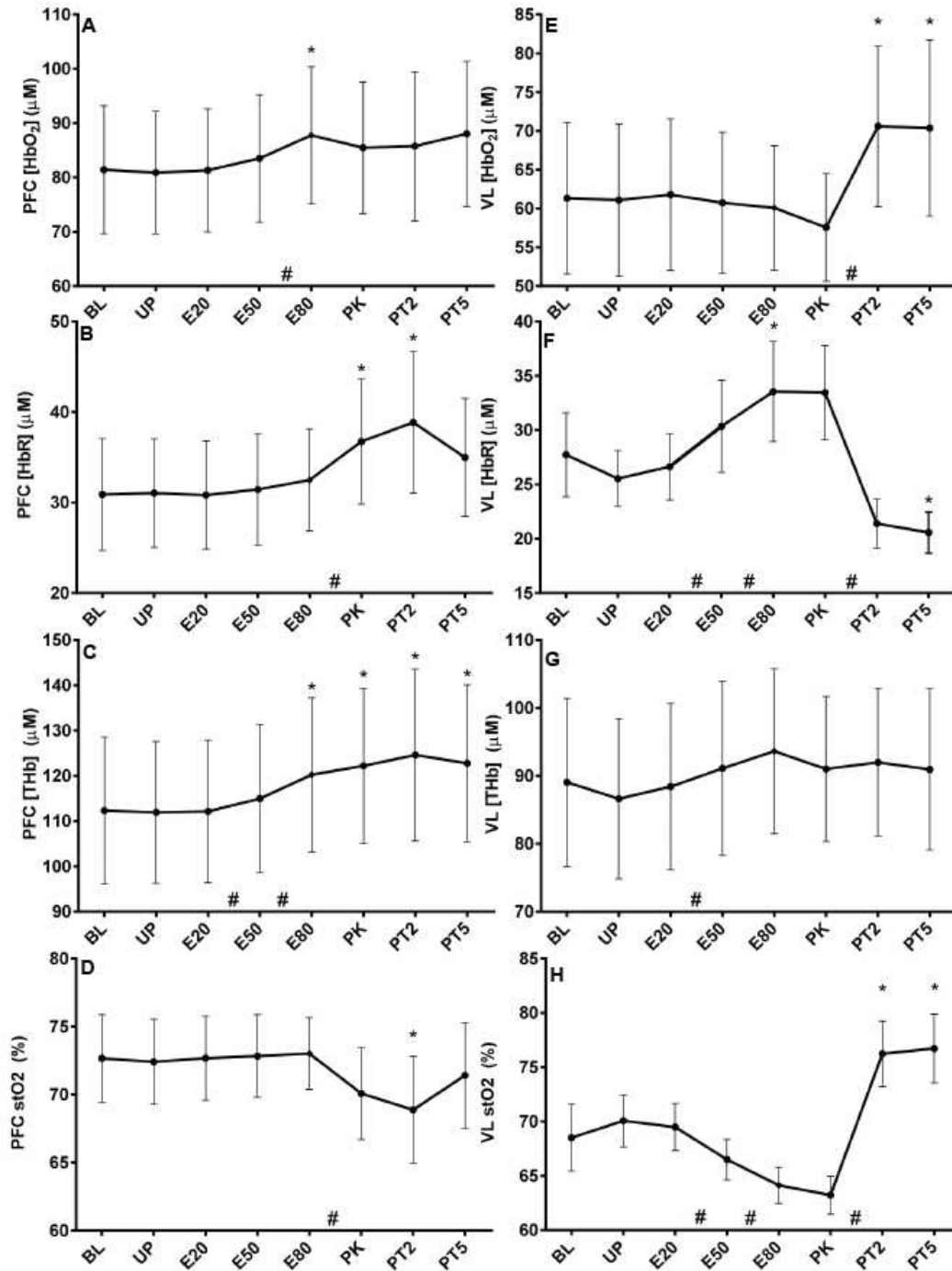


Figure 2.2: Subject TR-NIRS means for incremental exercise: Sample means \pm 95% CIs for [HbO₂], [HbR], [THb], and stO₂ in PFC (A - D) and VL (E - H). BL = baseline, UP = unloaded pedaling, E20 = 20% peak WR, E50 = 50% peak WR, E80 = 80% peak WR, PK = peak WR, PT2 = 2 minutes post, and PT5 = 5 minutes post. * = p < .05 vs. BL. # = p < .05 between consecutive data points.

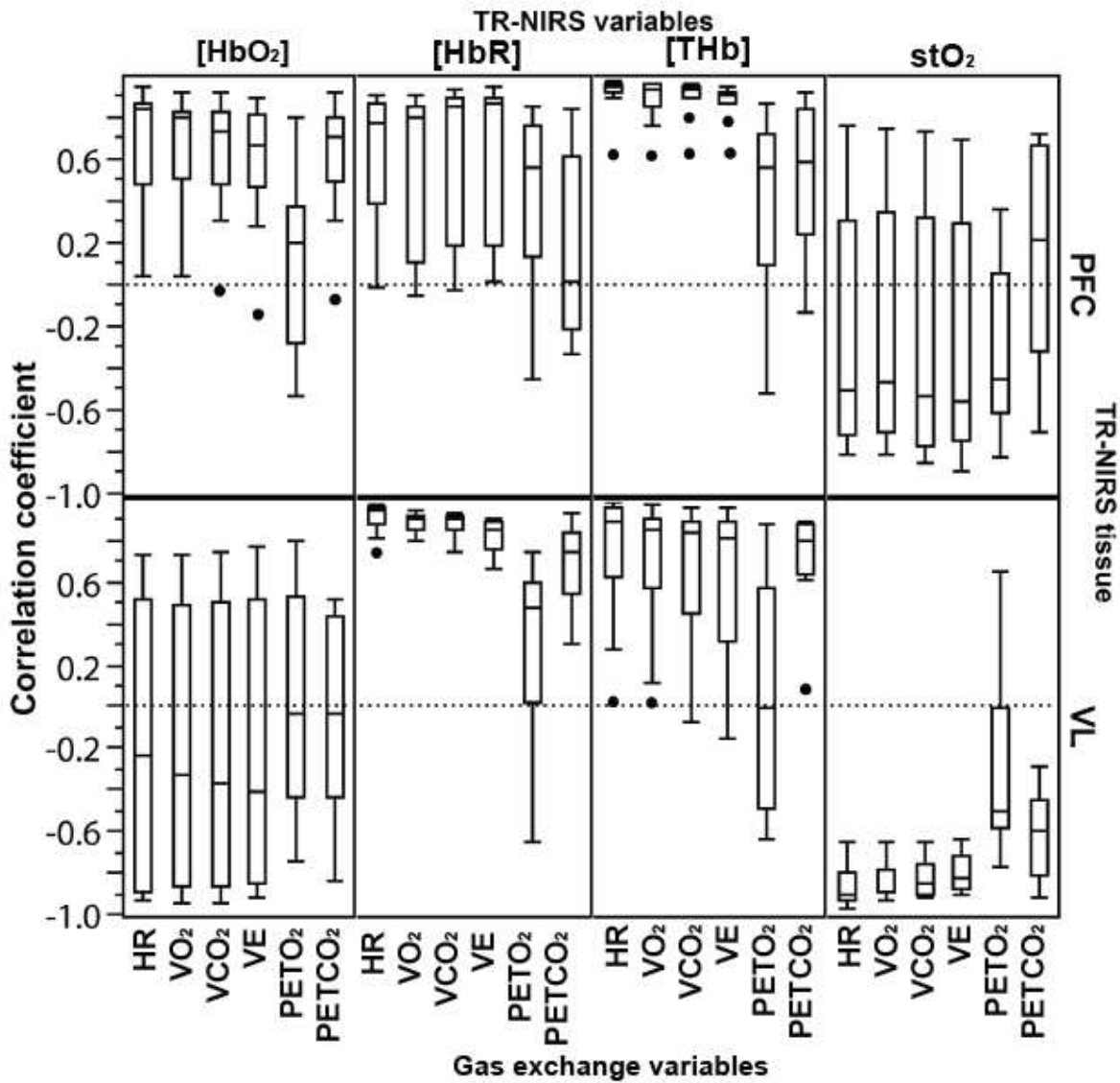


Figure 2.3: Correlation of TR-NIRS and gas exchange: Box plots of correlations between gas exchange variables and TR-NIRS variables in PFC (top row) and VL (bottom row) for both tissues over the entire duration of incremental exercise. Dots represent individual subject data. Boxes represent first quartile, median, and third quartile. Whiskers represent data range from minimum to maximum, with outliers shown as separate points.

Correlation between gas exchange and TR-NIRS measurements

Figure 2.3 shows the distribution (box plot) of the correlations between gas-exchange variables (HR, VE, VO_2 , VCO_2 , PET_{O_2} , PET_{CO_2}) and all four TR-NIRS variables in both tissues over the entire course of incremental exercise from the 11 subjects. It was found that VL [HbR] showed a high degree of positive correlation with the progressively increasing gas exchange variables, VO_2 , VCO_2 , VE, and HR ($r > 0.7$ for all). There was a reciprocal correlation between these variables and VL stO_2 ($r < -0.6$ for all). These same variables were highly positively correlated to PFC [THb] ($r > 0.6$ for all). PET_{CO_2} was moderately correlated with VL [THb], with one exception ($r > 0.6$ for 10/11 subjects).

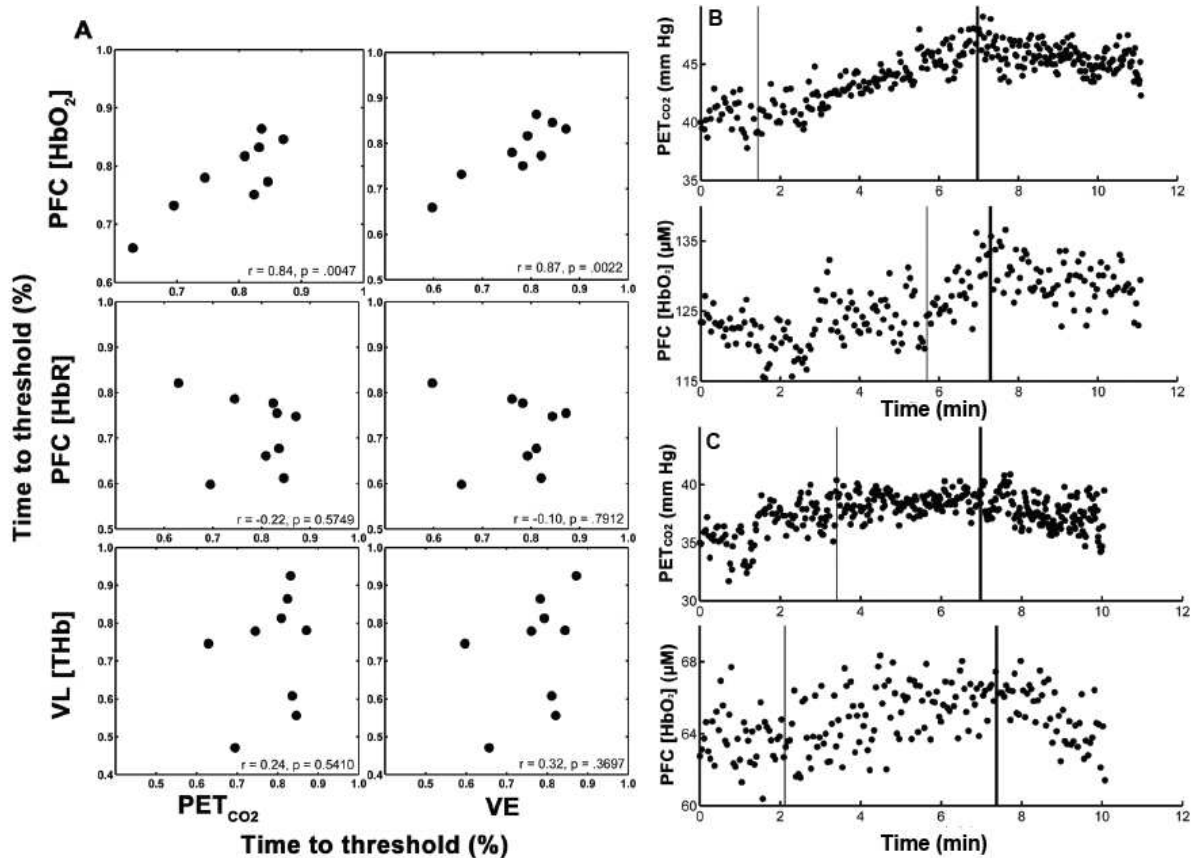


Figure 2.4 : Correlation between [HbO₂] and PETCO₂: A shows Pearson Product correlation between relative threshold times in PFC [HbO₂] (top), PFC [HbR] (middle), and VL [THb] (bottom), and the second ventilator threshold as detected in PETCO₂ (left column) and VE (right column). Fractional timings are normalized to total exercise time for each individual subject. B and C are representative piecewise fits for PETCO₂ (top) and PFC [HbO₂] (bottom) for two subjects. Thick vertical lines represent detected breakpoints of interest, while thinner lines represent other breakpoints.

Detection of TR-NIRS thresholds

On average, the VL [THb] threshold (transition from positive slope to steady state or negative slope) occurred at 73 ± 13 (mean \pm SD) % of PK. The PFC [HbR] threshold (transition from small positive slope or flat line to larger positive slope) occurred at 70 ± 7 % of PK, and the PFC [HbO₂] threshold (transition from positive slope to zero or negative

slope late in exercise) occurred at 80 ± 7 % of PK. We determined whether any of these thresholds were correlated in time to the occurrence of the second ventilatory threshold, identified in tracings of PET_{CO_2} and VE using the same piecewise regression technique. It was found that there was a strong correlation between PFC $[HbO_2]$ threshold and the timing of the transition to a negative slope in PET_{CO_2} ($r = 0.84$) and to increased positive slope in VE ($r = .87$). There were no such correlations with PFC $[HbR]$ and VL $[THb]$ (Fig 2.4A). There were 2 subjects in whom the threshold could not be resolved from the piecewise regression model. When examining the data visually, one revealed no such transitions in either PET_{CO_2} or $[HbO_2]$ in the late stages of exercise and in the other, there was a decline in $[HbO_2]$ at 0.91 of total exercise time, but a change to steeper positive slope in PET_{CO_2} at a similar time (0.84 of total time).

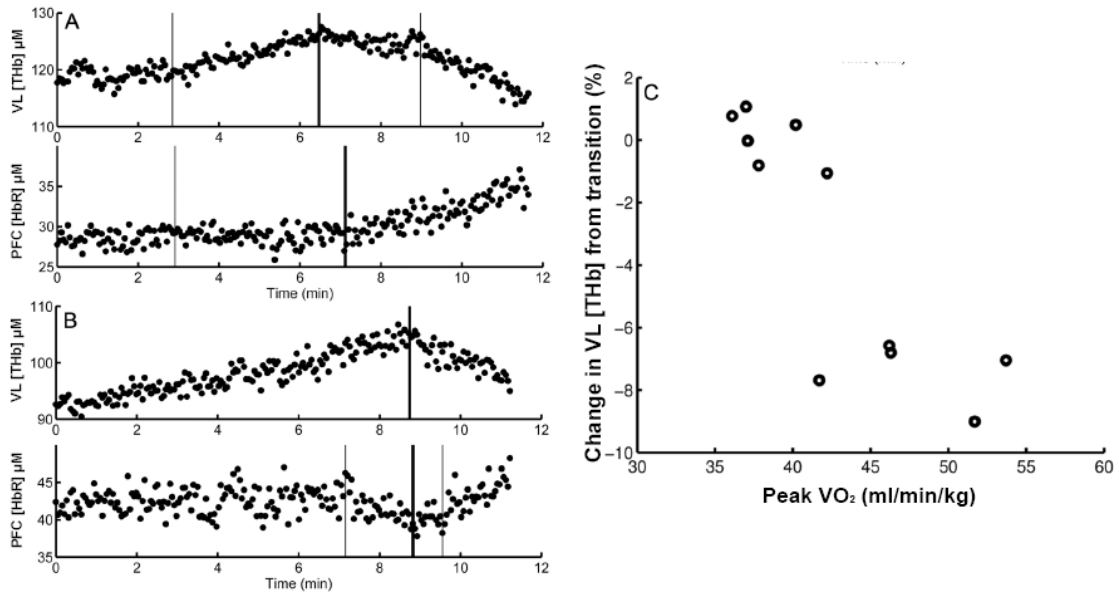


Figure 2.5: Muscle [THb] and PFC [HbR]: A - B show representative piecewise fits of VL [THb] (top) and PFC [HbR] (bottom) in 2 subjects. The thick vertical lines represent the detected breakpoints of interest, while the thinner lines represent other breakpoints. C shows scatter plot of peak VO₂ (ml/min/kg) achieved by individual subjects on the x-axis, and the percentage drop of VL [THb] from peak for each corresponding subject on the y-axis.

A moderate correlation was also found between thresholds in VL [THb] and PFC [HbR] ($r = .73$). Specifically, it appears that there is a transition to steady state or negative slope in VL [THb] at a similar time to when there is a transition to more steeply increasing PFC [HbR]. Figure 2.5 demonstrates this in two representative subjects (Fig. 2.5A and 2.5B).

Table 2.1 PFC All comparisons: Full Comparisons for each optical variable for ramp exercise in PFC.

Supplementary Information: PFC Oxygenation Full Statistics												
	PFC [HbO ₂]			PFC [HbR]			PFC [THb]			PFC [stO ₂]		
	Diff.	SE	Adj P	Diff.	SE	Adj P	Diff.	SE	Adj P	Diff.	SE	Adj P
UP - BL	-0.53	0.89	1.0000	0.16	0.37	1.0000	-0.37	0.92	1.0000	-0.28	0.38	1.0000
E20 - BL	-0.12	0.85	1.0000	-0.06	0.44	1.0000	-0.18	1.03	1.0000	0.01	0.35	1.0000
E50 - BL	2.09	1.23	1.0000	0.56	0.52	1.0000	2.65	1.44	1.0000	0.16	0.38	1.0000
E80 - BL	6.33	0.96	0.0017	1.60	0.96	1.0000	7.93	1.44	0.0073	0.35	0.62	1.0000
PK - BL	4.04	1.54	0.7229	5.85	1.36	0.0445	9.88	1.99	0.0159	-2.59	0.89	0.4213
P2 - BL	4.32	1.75	0.9347	7.98	1.18	0.0014	12.29	2.19	0.0062	-3.79	0.62	0.0034
P5 - BL	6.60	2.14	0.3242	4.09	1.43	0.4678	10.69	1.62	0.0017	-1.18	1.21	1.0000
E20 - UP	0.41	0.72	1.0000	-0.22	0.25	1.0000	0.19	0.62	1.0000	0.27	0.34	1.0000
E50 - UP	2.62	0.89	0.4139	0.40	0.37	1.0000	3.02	1.01	0.3817	0.42	0.32	1.0000
E80 - UP	6.86	0.77	0.0001	1.44	0.75	1.0000	8.30	1.05	0.0004	0.61	0.52	1.0000
PK - UP	4.57	1.14	0.0706	5.69	1.23	0.0264	10.26	1.54	0.0016	-2.34	0.81	0.4659
P2 - UP	4.85	1.76	0.5659	7.82	1.13	0.0012	12.66	2.13	0.0040	-3.53	0.66	0.0090
P5 - UP	7.12	2.05	0.1683	3.93	1.45	0.6193	11.06	1.42	0.0004	-0.92	1.26	1.0000
E50 - E20	2.21	0.67	0.2199	0.62	0.35	1.0000	2.83	0.61	0.0268	0.15	0.29	1.0000
E80 - E20	6.45	0.91	0.0009	1.66	0.89	1.0000	8.11	0.88	<.0001	0.35	0.60	1.0000
PK - E20	4.16	1.06	0.0801	5.91	1.20	0.0166	10.07	1.31	0.0005	-2.60	0.84	0.3236
P2 - E20	4.44	1.52	0.4232	8.04	1.07	0.0006	12.48	1.92	0.0019	-3.80	0.57	0.0017
P5 - E20	6.72	1.99	0.1949	4.15	1.34	0.3177	10.87	1.28	0.0002	-1.19	1.18	1.0000
E80 - E50	4.24	1.00	0.0476	1.04	0.64	1.0000	5.28	0.67	0.0004	0.19	0.60	1.0000
PK - E50	1.95	1.02	1.0000	5.29	1.09	0.0182	7.24	1.05	0.0012	-2.76	0.79	0.1688
P2 - E50	2.23	1.71	1.0000	7.42	0.96	0.0004	9.65	1.78	0.0083	-3.95	0.67	0.0040
P5 - E50	4.51	2.18	1.0000	3.53	1.33	0.6763	8.04	1.36	0.0041	-1.34	1.25	1.0000
PK - E80	-2.29	0.88	0.7536	4.25	0.77	0.0074	1.95	0.69	0.4955	-2.95	0.53	0.0064
P2 - E80	-2.01	1.50	1.0000	6.38	1.09	0.0044	4.36	1.30	0.2051	-4.14	0.74	0.0065
P5 - E80	0.27	1.91	1.0000	2.49	1.45	1.0000	2.76	0.89	0.3120	-1.53	1.21	1.0000
P2 - PK	0.28	1.54	1.0000	2.13	0.92	1.0000	2.41	1.31	1.0000	-1.19	0.78	1.0000
P5 - PK	2.56	2.09	1.0000	-1.76	1.91	1.0000	0.80	1.02	1.0000	1.41	1.45	1.0000
P5 - P2	2.28	1.56	1.0000	-3.89	1.51	0.7650	-1.61	0.98	1.0000	2.61	1.05	0.9017

Table 2.2 VL all comparisons: Full Comparisons for each optical variable for ramp exercise in VL.

Supplementary Information: VL Oxygenation Full Statistics

	VL [HbO ₂]			VL [HbR]			VL [THb]			VL [stO ₂]		
	Diff.	SE	Adj P	Diff.	SE	Adj P	Diff.	SE	Adj P	Diff.	SE	Adj P
UP - BL	-0.22	0.53	1.0000	-2.19	0.80	0.6019	-2.41	0.62	0.0844	1.56	0.65	1.0000
E20 - BL	0.45	0.69	1.0000	-1.10	0.92	1.0000	-0.64	0.86	1.0000	0.98	0.81	1.0000
E50 - BL	-0.58	0.73	1.0000	2.63	1.01	0.7519	2.04	0.79	0.7550	-2.01	0.94	1.0000
E80 - BL	-1.23	1.41	1.0000	5.82	1.28	0.0293	4.58	1.19	0.0891	-4.39	1.24	0.1517
PK - BL	-3.76	1.97	1.0000	5.73	1.41	0.0851	1.97	1.60	1.0000	-5.28	1.48	0.1456
P2 - BL	9.28	0.89	<.0001	-6.33	1.59	0.0729	2.95	1.79	1.0000	7.73	1.05	0.0007
P5 - BL	9.05	1.13	0.0003	-7.16	1.64	0.0394	1.90	1.65	1.0000	8.21	1.16	0.0010
E20 - UP	0.67	0.44	1.0000	1.09	0.56	1.0000	1.77	0.58	0.3363	-0.58	0.48	1.0000
E50 - UP	-0.36	0.68	1.0000	4.82	1.06	0.0308	4.45	0.66	0.0014	-3.57	0.80	0.0337
E80 - UP	-1.01	1.48	1.0000	8.01	1.28	0.0026	6.99	0.84	0.0002	-5.95	1.13	0.0099
PK - UP	-3.54	2.08	1.0000	7.92	1.29	0.0030	4.38	1.19	0.1164	-6.84	1.35	0.0137
P2 - UP	9.50	1.17	0.0003	-4.14	1.07	0.0885	5.36	1.51	0.1454	6.17	0.82	0.0005
P5 - UP	9.27	1.34	0.0011	-4.97	1.09	0.0297	4.31	1.55	0.5472	6.65	0.89	0.0006
E50 - E20	-1.03	0.50	1.0000	3.72	0.67	0.0070	2.69	0.42	0.0023	-2.99	0.44	0.0013
E80 - E20	-1.68	1.34	1.0000	6.91	0.96	0.0008	5.23	0.94	0.0065	-5.37	0.82	0.0018
PK - E20	-4.21	2.03	1.0000	6.82	0.95	0.0009	2.81	1.46	1.0000	-6.26	1.08	0.0049
P2 - E20	8.83	1.24	0.0009	-5.24	1.34	0.0824	3.59	1.74	1.0000	6.74	0.97	0.0011
P5 - E20	8.60	1.43	0.0037	-6.06	1.29	0.0231	2.54	1.81	1.0000	7.23	0.96	0.0005
E80 - E50	-0.65	0.95	1.0000	3.19	0.47	0.0013	2.54	0.88	0.4568	-2.38	0.51	0.0258
PK - E50	-3.18	1.66	1.0000	3.10	0.60	0.0111	-0.08	1.53	1.0000	-3.27	0.82	0.0708
P2 - E50	9.86	1.22	0.0003	-8.96	1.86	0.0194	0.91	1.84	1.0000	9.74	1.17	0.0002
P5 - E50	9.64	1.53	0.0026	-9.78	1.80	0.0081	-0.15	1.83	1.0000	10.22	1.18	0.0002
PK - E80	-2.52	1.00	0.8387	-0.09	0.34	1.0000	-2.81	1.04	0.8674	-0.89	0.47	1.0000
P2 - E80	10.51	1.50	0.0010	-12.15	2.09	0.0048	-1.63	1.55	1.0000	12.12	1.39	0.0002
P5 - E80	10.29	1.96	0.0103	-12.97	2.05	0.0024	-2.89	1.73	1.0000	12.60	1.42	0.0001
P2 - PK	13.04	2.03	0.0021	-12.06	2.06	0.0044	0.98	0.79	1.0000	13.01	1.68	0.0004
P5 - PK	12.81	2.40	0.0093	-12.88	1.98	0.0019	-0.07	1.21	1.0000	13.49	1.67	0.0003
P5 - P2	-0.23	0.74	1.0000	-0.83	0.32	0.8017	-1.05	0.70	1.0000	0.48	0.43	1.0000

Changes in optical path length (PL) and scattering

PL at 796 nm declined significantly during exercise in both tissues. In the VL, path length at E50 and all subsequent stages was lower than the baseline value (from 14.90 cm at BL to 14.56 at E80, $p < .001$). In the PFC, this occurred at E80 and all subsequent points (from 15.39 cm at BL to 15.13 cm at 0.8 PK, $p < .05$). With regard to scattering coefficient, μ_s' (assessed at only BL, E50, and PK) there was on average an increase in the PFC in the latter half of exercise (10.46 cm^{-1} v. 10.65 cm^{-1} , E50 v. PK, $\text{adj.}p = .038$) and an average decrease in the VL which occurred in the first half of exercise (8.54 cm^{-1} v. 8.36 cm^{-1} , UP v. E50, $p = .0028$). These changes are summarized in figure 2.6.

In several instances, it was observed that using the fitting-and-change (FAC) processing method caused the calculated chromophore concentrations to be different both in absolute numbers as well as dynamics, as in the examples shown in one representative subject (Figure 2.7).

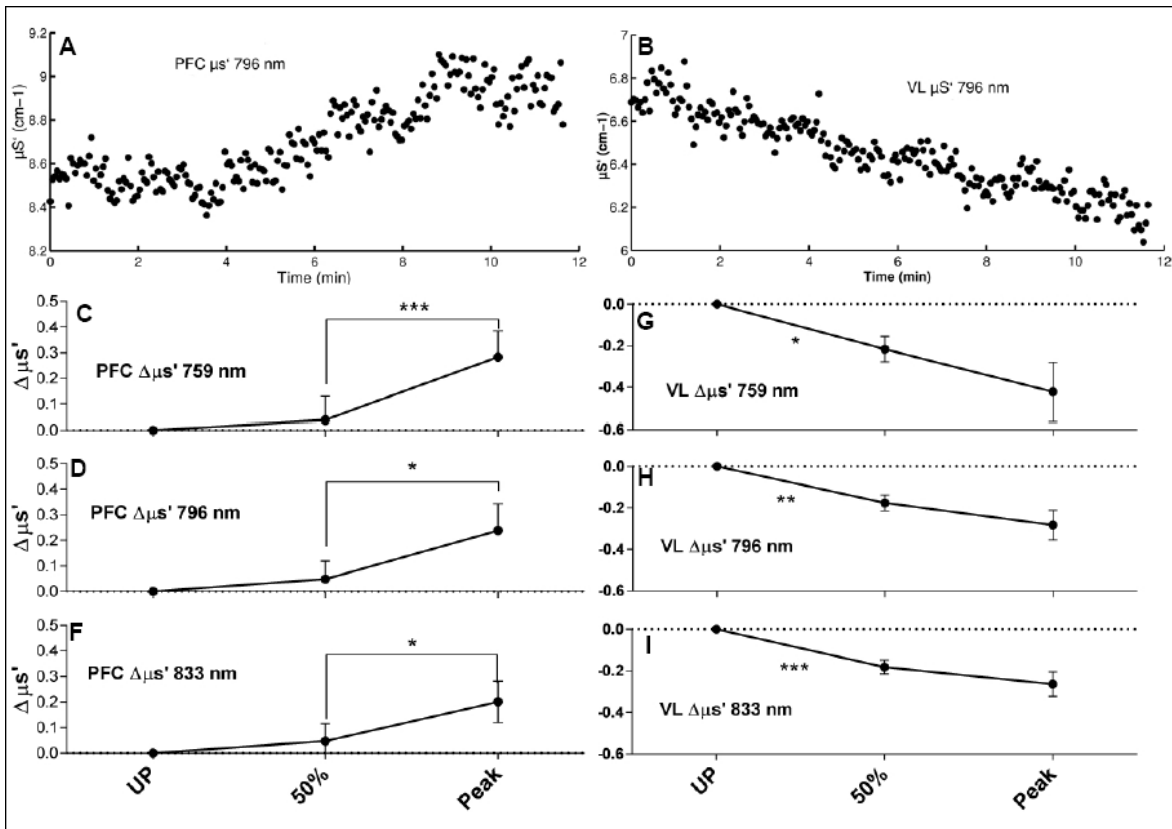


Figure 2.6: Scattering changes: Summary of scattering changes during exercise in both tissues. Panel A shows raw data for PFC scattering coefficient at 796 nm during ramp exercise in one subject, whereas panel B shows the same for the VL. C-F show mean changes in PFC 796 μ_s' for all 11 subjects at UP, E50, and PK exercise, whereas G-I show mean changes in scattering from UP in the VL.

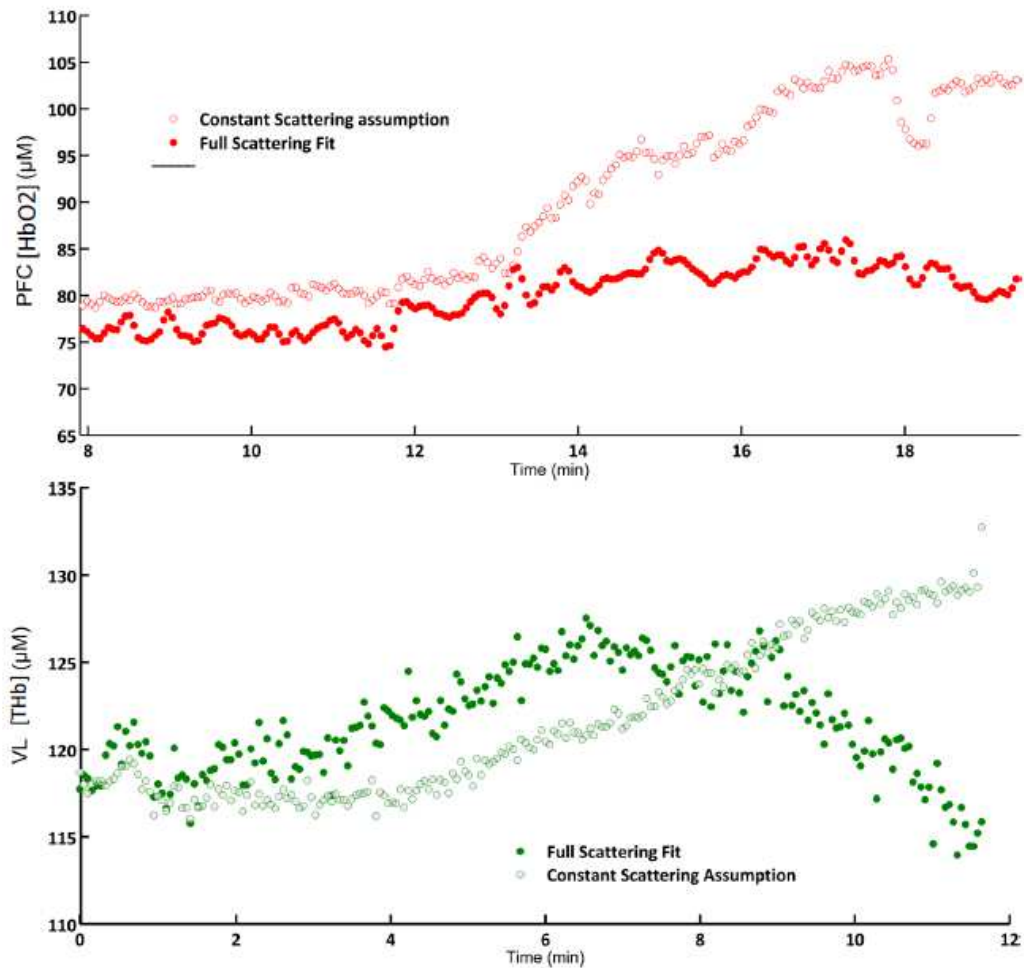


Figure 2.7 Effect of constant scattering assumption: PFC [HbO₂] (top) and VL [THb] (bottom) in one subject during ramp exercise. The filled circle represent the full time-domain fit, whereas the hollow circles are the same data processed with the assumption of constant scattering coefficients.

Note that the assumption of constant scattering results in significantly different physiological dynamics, as well as very different values of both PFC [HbO₂] and VL [THb] at maximal exercise intensity.

DISCUSSION

In this set of studies we demonstrated significant changes in absolute hemoglobin concentrations, oxygenation, and optical PL and μ_s' that occur simultaneously in the exercising muscle and brain of children during incremental cycling and post-exercise recovery. We also identified physiological thresholds that can be detected in both VL and PFC TR-NIRS data, the temporal relation of these thresholds to one another, and to systemic physiological responses, such as VE and PET_{CO2}.

Muscle Oxygenation

In our study a significant and progressive decrease in stO₂ occurred during the middle stages of incremental exercise. This was accompanied by an increase in [THb] from UP to E80. This change in [THb] was driven by a large increase in [HbR], and in absolute terms, a smaller decrease in [HbO₂]. VL [HbR] was highly correlated to progressive measures of exercise intensity. As shown in figure 2.3, VL [HbR] and stO₂ were uniformly highly correlated to VE, HR, V_{O2} and V_{CO2} indicating an intensity-dependent increase in muscle O₂ extraction. These findings are consistent with those recently reported in ramp

exercise in adults, demonstrating general agreement with existing CW-NIRS methodologies (83,84). The increase in [HbR] has been demonstrated to reflect microvascular O₂ extraction (85). We also observed that during each incremental test VL [THb], an index of total blood volume in muscle tissue(86), after a steady initial increase, displayed a threshold, i.e. a point beyond which it remained constant or declined from a peak value. Furthermore, there was a significant correlation between the timing of the VL [THb] threshold and the time at which PFC [HbR] begins to increase more steeply ($r = .73$). Based on this analysis, subjects either demonstrated a noticeable drop in VL [THb] from the threshold value to PK ($n = 5$, ranging from -6.6% to -9.0%), or little to no change ($n = 6$, ranging from -1.1% to +1.1%). The subjects who demonstrated larger drops in VL [THb] tended to also have higher levels of peak aerobic fitness, achieving peak V_{O₂} values of > 40 ml/min/kg (Fig. 5C). In incremental cycling, leg vascular conductance (VC) and blood flow are known to reach maxima before V_{O₂} peak (87), possibly due to the increasing sympathetic vasoconstriction in the later stages of exercise, which dampens the O₂ demand-driven vasodilation that occurs during the earlier stages of exercise (87). We can speculate that the threshold in muscle [THb] we observed corresponds to a maximum in VC reached in the incremental test. Other invasive methods must be used to confirm this in future studies. The observation that this muscle [THb] threshold correlates with the onset of faster O₂ extraction in the PFC suggests the possibility of signaling between exercising muscle and the brain, perhaps by increased afferent autonomic stimuli(88). In this study, only one location on the VL was measured, and therefore we cannot address any potential effects of dynamic spatial heterogeneity in the exercising muscles of the leg (89,90), nor the inhomogeneity introduced by variations in subcutaneous tissue thickness(91) or skin

blood flow(92). Nonetheless, based on these results, the assessment of the [THb] threshold in exercising muscle during incremental tests may be a way to evaluate muscle vascular adaptation to exercise.

PFC Oxygenation

The typical pattern of NIRS measurements in the PFC during ramp exercise is an increase in both [HbR] and [HbO₂] with increasing intensity, with a possible decline in [HbO₂] and stO₂ at the highest intensities depending on age and training status(93,94). It is hypothesized by some that this decline in stO₂ may be a limiting factor in exercise performance (93-95), however the published evidence is not conclusive (95). Other studies have shown that intense exercise is associated with an increase in regional cerebral blood flow (CBF) using techniques such as Trans-Cranial Doppler Ultrasound and clearance of ¹³³Xe(96). More recently, Vogiatzis et al showed that in athletes, incremental exercise is associated with an increase in frontal cortex blood flow, with a relative reduction at the highest intensities when exercise was performed under hypoxic conditions(97). Similar findings were recently reported in a group of adult subjects, in which low-intensity exercise increased cerebral vascular conductance(VC) (98) (at least in young individuals), while higher work intensities induced a decline in cerebral VC in both old and young adults(98), a decline attributed to the simultaneous decrease in arterial CO₂ content, caused by hyperventilation late in exercise (98). Taken together, these and other studies point to an increase in cerebral VC and blood volume at lower intensities, with a likely decrease at the highest intensities.

In our study, the level of [THb], which has been tied to the level of cerebral blood volume (94), also increased and seemed to plateau above E80, remaining elevated for at least the first 5 min after exercise cessation. Interestingly, PFC [THb] was correlated to exercise intensity in much the same way as VL [HbR] (figure 3). This suggests that the increase in [THb] is dependent on the increases in cardiac output and ventilation. On average, we also observed an absolute decline in stO₂ beginning at E80. Others have suggested that PFC stO₂ declines in late exercise in response to hyperventilation and decreased PET_{CO2} (81). Because stO₂ is sensitive to changes in both [HbO₂] and [HbR], we chose to analyze [HbO₂] specifically because it tends to more closely follow perfusion (99). The high degree of temporal correlation between the point at which PET_{CO2} declines and the point at which PFC [HbO₂] declines ($r = 0.84$) would lend evidence to a relationship between the drop in PET_{CO2} and PFC perfusion late in incremental exercise.

PFC [HbR] in most subjects seemed to behave differently from [HbO₂], following as determined by piecewise linear regression, with slow and fast phases of increase. The fast phase began at an average of 70% of PK ($\sigma = 8\%$). This behavior likely reflects increasing glucose, lactate, and O₂ A-V differences (98), as well as increased PFC O₂ demand to maintain performance at the highest intensities. With regard to brain metabolism, Secher et al (88,96) have extensively reviewed concepts of cerebral metabolism in exercise. There is evidence of both regional increases in anaerobic metabolism, as well as increased glycolysis and oxidation of lactate late in exercise(88). These changes, although still incompletely understood, appear related to increased lactate availability, and perhaps increased sympathetic activity. We can speculate that the changes observed in PFC [HbR] in our study are driven by the well-known delayed accumulation of blood lactate.

Interestingly, PFC [THb] and [HbR] also remained significantly elevated for several minutes post-exercise (12.3 and 8.0 μM higher, $p = .0062$ and $.0014$, respectively, at PT2). PFC stO_2 was also significantly lower (3.8% less than BL, $p = .0034$) in the first minutes post-exercise, perhaps reflecting excess post-exercise oxygen consumption in PFC(100). It should also be noted that PFC [HbO₂] decline occurs in the context of a continuously increasing [HbR], perhaps indicating an early discrepancy between continuously increasing metabolism and a limitation in perfusion. While not conclusive, this leaves open the possibility that the decline in [HbO₂] is predictive of test cessation.

Changes in optical path length and scattering

We found that exercise is associated with changes in PL and μ_s' in both tissues. One potential explanation for a change in PFC PL and scattering is a change in cerebral fluid distribution with exercise. It has been shown that in mice, brain edema is associated with a measurable increase in scattering properties (101). Other hypotheses for changes in scattering with exercise are speculative (including changes in hematocrit and blood density), and warrant further investigation, combined with other measurements, such as intracranial pressure. In the case of exercising muscle, the overall picture is different. Ferrari et al reported that using a frequency-domain NIRS device, the assumption of constant scattering results in overestimation in the change in both [HbO₂] and [HbR] in the exercising muscle (83). In contrast to the values reported here, the same study also

reported that exercise was associated with an increase in muscle μ_s' . Given the significant changes in PL and μ_s' , it is possible that CW-NIRS methods would interfere with detection of NIRS threshold events during incremental exercise, such as has been suggested in another published report involving a steady-state exercise challenge (102).

The observation that not accounting for changes in scattering can lead to different physiological interpretations is particularly interesting. In the bottom panel of figure 2.7, it is shown that one can obtain entirely different physiological dynamics of muscle [THb] by the two processing methods. Using the more accurate FAD method, it appears that there is a threshold in muscle [THb], a time point after which the level declines until maximal exercise, as described below. However, the FAC method completely loses sensitivity to this event. There is some precedent for similar observations in the literature (102), but further exploration of this topic is warranted, perhaps by comparison of FAD method to other ways of interpreting the TPSF data obtained by TR-NIRS, such as monte carlo methods.

Correlations between gas exchange and TR-NIRS measurements

As figure 3 demonstrates, there are TR-NIRS variables that show correlation with gas exchange parameters over the whole duration of incremental exercise. However, a more careful analysis would take into account the known threshold behavior observed in incremental exercise. To that end, we have used a data-driven approach to determine whether there are correlations between threshold events in physiological data collected by different instruments and at different sites. This method required minimal averaging of data, and provided iterative determination of the optimal points of slope changes. We also

applied the same technique to the study of pulmonary gas exchange data to make correlations between established ventilatory transitions and TR-NIRS measurements. While the use of this particular software tool in physiology is relatively novel, the concept of threshold modeling is not. Incremental exercise is frequently modeled by division into three phases by identifying two ventilatory thresholds, or increases in the rate of ventilation (103). A similar approach was used by Mizuno et al (104) to identify transition times in both heart rate and oxygenation data in incremental exercise. They found, using a two-linear phase approach, that quadriceps oxygenation changes were correlated in time to the onset of slope changes in HR. This approach was successful, despite the observation that in later stages of exercise, HR does not follow first degree kinetics; indeed, others have described the HR transition as a loss of the linear relationship between HR and work rate (105). While the piecewise linear approach does not achieve full mathematical description of physiological kinetics (77), it is useful in the identification of transitions between phases, which are frequently described in a variety of exercise paradigms.

In summary, our findings show that significant, reproducible changes occur in muscle and PFC oxygenation in children performing and recovering from intense exercise. These changes often parallel the kinetic profiles of established cardiopulmonary variables, as shown by the observed correlation between onset of hyperventilation and reduction in PFC perfusion.

CHAPTER 3: Cerebral oxygenation during exercise with an assessment of the effect of training

RATIONALE

If optical measurements of cerebral oxygenation and hemodynamics are to be of any use in longitudinal assessments, the effects of training on these responses must be established. In most cases, successful aerobic training denotes an increase in peak $\dot{V}O_2$ achieved during incremental exercise testing (20). Given recent discoveries, such as an association between exercising training and higher brain volume in later life (106), there is and will continue to be increased interest in the neurological effects of exercise training. Furthermore, it has been demonstrated that acute exercise has beneficial effects on executive function in children and adolescents, a function mediated in part by the prefrontal cortex (PFC) (107). What is not known is whether there is any similar effect of prolonged training on executive function (107). TR-NIRS clearly cannot address this question directly, but any information about potential hemodynamic or vascular adaptation to training will add to the weight of evidence either way.

While the range of NIRS responses to incremental exercise is being investigated thoroughly at many institutions (as described in the discussion of the previous chapter), there is very little published data on cerebral oxygenation in combination with training status. Moreover, there is little to nothing published on this topic in the study of pediatric subjects, and certainly no studies using diffuse optical techniques such as TR-NIRS as opposed to commercial CW-NIRS systems. This set of data is novel in several ways, and should prove an important contribution to the literature of cerebral hemodynamics and their adaptation during exercise training.

The hypotheses investigated in this study are fairly straightforward, and somewhat exploratory. Firstly, given that aerobic training, if successful, will result in an increase in peak VO_2 achieved during incremental exercise, one might hypothesize an increase in peak values of TR-NIRS oxygenation parameters. For example, we might expect that peak exercise post-training might be characterized by a lower stO_2 at the highest intensities, or a higher maximal PFC [HbR]. Secondly, we might hypothesize that training will influence the relative position of the oxygenation thresholds described in the previous chapter; that is, we might expect that the relative work intensity at which PFC [HbR] begins to increase will be higher post-training, reflecting an acquired “resistance” to the rapid deoxygenation that occurs at high intensities. And finally, this data set will be used to continue the investigation of the potential effects of optical scattering on reported PFC oxygenation values.

In addition to addressing new hypotheses, these studies are also an opportunity to improve on the methodologies described in the previous chapter. For example, in these studies, a longer source-detector separation has been used, 4 cm, which ought to allow for

deeper tissue penetration (51). Additionally, the measurement interval was increased to five seconds from three, to achieve a higher signal-to-noise ratio and therefore more reliable data. And finally, rather than using the above-described SLM method for identification of NIRS thresholds, in this study, a more robust statistical method implemented in R called segmented regression was used (108,109). Unlike the SLM method, segmented regression allows for the computation of confidence intervals around estimated breakpoints, and also the estimation of the number of real breakpoints in addition to their position in time. This latter function, although highly desirable, is still somewhat experimental.

METHODS

In most respects, the methods used in this experimental data set are similar to those used in the previous chapter, with the exception of the longitudinal training aspect.

Study population

Subjects were 14 healthy children of average age 15.1 ± 1.6 years (STD, 9 F, 5 M). All participants provided written informed assent along with parental consent prior to participation. Pre and post training assessments included both incremental and interval exercise challenges with gas exchange measurements, body composition by dual x-ray absorptiometry, as well as regular physical activity by actigraphy. Prior to each testing visit, vital signs were measured. Training was conducted with the goal of improving peak O₂ consumption (VO₂ peak). For studies of TR-NIRS, only the control study participants were assessed, and therefore asthma and obesity were exclusion criteria. Other measures performed included tests of pulmonary function, as well as various questionnaires.

Incremental exercise testing

All subjects underwent incremental maximal exercise testing twice before and after the training period. For all incremental tests, the same resistance step-rate was used, and was initially determined by subject height, weight, and reported physical activity levels. Each test consisted of a brief warm-up of pedaling with no resistance (< 30 seconds) followed by continuous increasing resistance on an electromagnetically braked cycle ergometer. Ramp phase continued until voluntary termination or prolonged inability to maintain cycling speed of > 45 rpm. Gas exchange measurements were collected during the ramp phase by a mouthpiece connected to a metabolic cart (Sensormedics). Breath-by-

breath values were tabulated and analyzed in conjunction with TR-NIRS measurements. EKG was also continuously monitored using four skin surface electrodes.

Exercise Training Protocol

Training sessions were conducted 3 times per week over a duration of 8-10 weeks, under the supervision of a trained exercise physiologists. Sessions were at least 30 minutes long and consisted of moderate to high intensity exercise on stationary equipment.

TR-NIRS measurements

TR-NIRS measurements using the TRS-20 device were conducted using 1 channel during incremental maximal testing visits before and after training. In situations where two TR-NIRS measurements were collected before and/or after training, the testing session when a higher peak work rate was achieved was analyzed. Measurements were made on the left prefrontal cortex (PFC), with the optical probe placed as far superior and lateral on the forehead as possible, without interference from hair. The source-detector separation used in these studies was 4 cm, and the measurement interval was five seconds. TR-NIRS measures included concentrations of oxyhemoglobin ([HbO₂]), deoxyhemoglobin ([HbR]), total hemoglobin ([THb]) and oxygen saturation (stO₂).

Data Analysis

Continuous TR-NIRS data was combined with breath-by-breath gas exchange data, and binned into approximately 20-second long windows using MATLAB (Version 2013a, Mathworks, Natick, MA). Then, data from baseline (BL), 20%, 40%, 60%, 80% and peak exercise were tabulated for each test for comparison between pre and post training testing sessions. These time points are referred to as BL (baseline), E0 (onset of resistance), E20 (20% of peak work), E40 (40%), E60 (60%), E80 (80%), and PK (peak exercise).

Additionally, binned data was analyzed using the segmented package (108) in R. For this analysis, cerebral [HbR] responses were analyzed in two ways: one with the number of internal breakpoints set to two, and one with no initial guesses regarding the number and location of breakpoints. For each [HbR] tracing, a three-phase model was computed with breakpoints corresponding to changes in slope of [HbR], along with 95% confidence intervals centered around each breakpoint. The time at which each breakpoint occurs was normalized to the total exercise time to obtain a percentage of peak exercise time at which each transition occurred. These transitions were tabulated and analyzed for any differences between pre- and post training sessions. Two-way repeated analysis of variance was conducted on pre-training and post-training TR-NIRS parameters, with effects of exercise stage and training assessed. Post-hoc multiple comparisons with Bonferroni correction were reported. Plots of raw TR-NIRS data were generated in MATLAB.

RESULTS

Effect of training

The mean weight of subjects pre-training was 56.1 ± 8.7 kg, whereas it was 56.7 ± 8.6 kg post-training, with no significant change. The mean pre-training BMI was 20.25 ± 2.02 .

Table 3.1 Training effects: The effects of 8 weeks of aerobic training on incremental test performance, measured by total time of exercise and peak work rate achieved.

Subject	Total exercise time (min)		Peak Work	
	Pre training	Post training	Pre training	Post training
1	8.60	9.22	132	137
2	9.35	10.74	142	160
3	7.39	8.26	111	122
4	8.84	10.45	181	211
5	8.72	10.04	176	211
6	13.27	14.05	201	216
7	7.82	8.45	121	126
8	8.64	9.64	131	147
9	10.67	12.02	216	244
10	12.42	12.15	246	251
11	10.51	12.30	215	246
12	10.25	9.90	156	151
13	10.40	11.72	157	176
14	8.70	8.84	132	166
Mean	9.68	10.56	166	183
Std	1.68	1.69	41	46
SEM	0.45	0.45	11	12
	<i>p</i>	0.0002916	<i>p</i>	0.000157

Broadly, the training regimen used was successful in causing increased performance on the incremental test, both in terms of total exercise time and peak work rate achieved.

Subjects were able to cycle for close to one minute longer after training ($p < 0.001$), and achieved a work rate approximately 17 watts higher on average ($p < 0.001$). These effects are shown for all subjects in Table 3.1.

TR-NIRS tracings

In broad terms, the dynamics measured by TR-NIRS were similar in this subject group to those described in the previous chapter. This was important to establish because the source-detector separation was changed to 4 cm for these studies to allow for greater optical penetration depth. What follows are a series of 4-panel images showing raw tracings both pre-training and post-training for four individual subjects. Note that post-training tracings (red) tend to be longer, reflecting longer times until exhaustion.

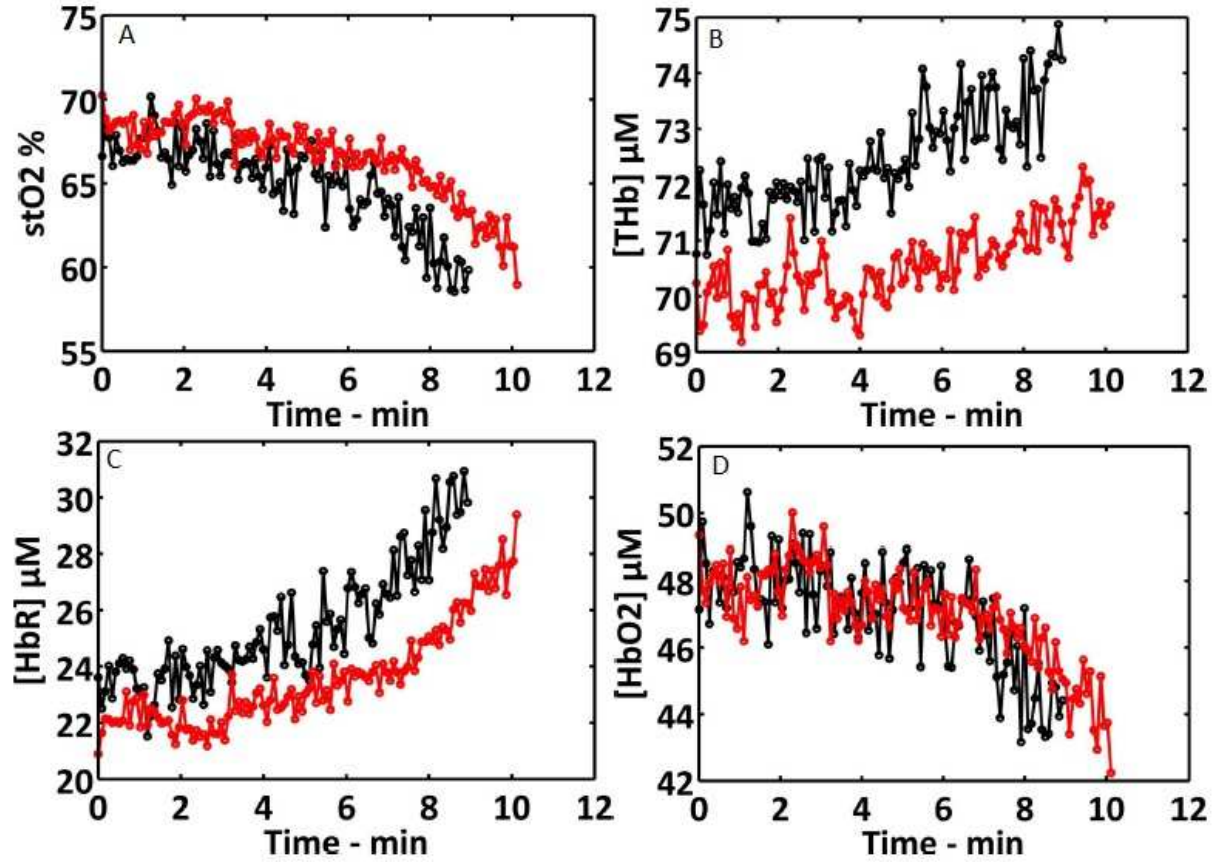


Figure 3.1: Raw tracings subject 1: Raw tracings of stO_2 (A), THb (B), $[HbR]$ (C), and $[HbO_2]$ (D) in one female subject before (black) and after (red) aerobic training.

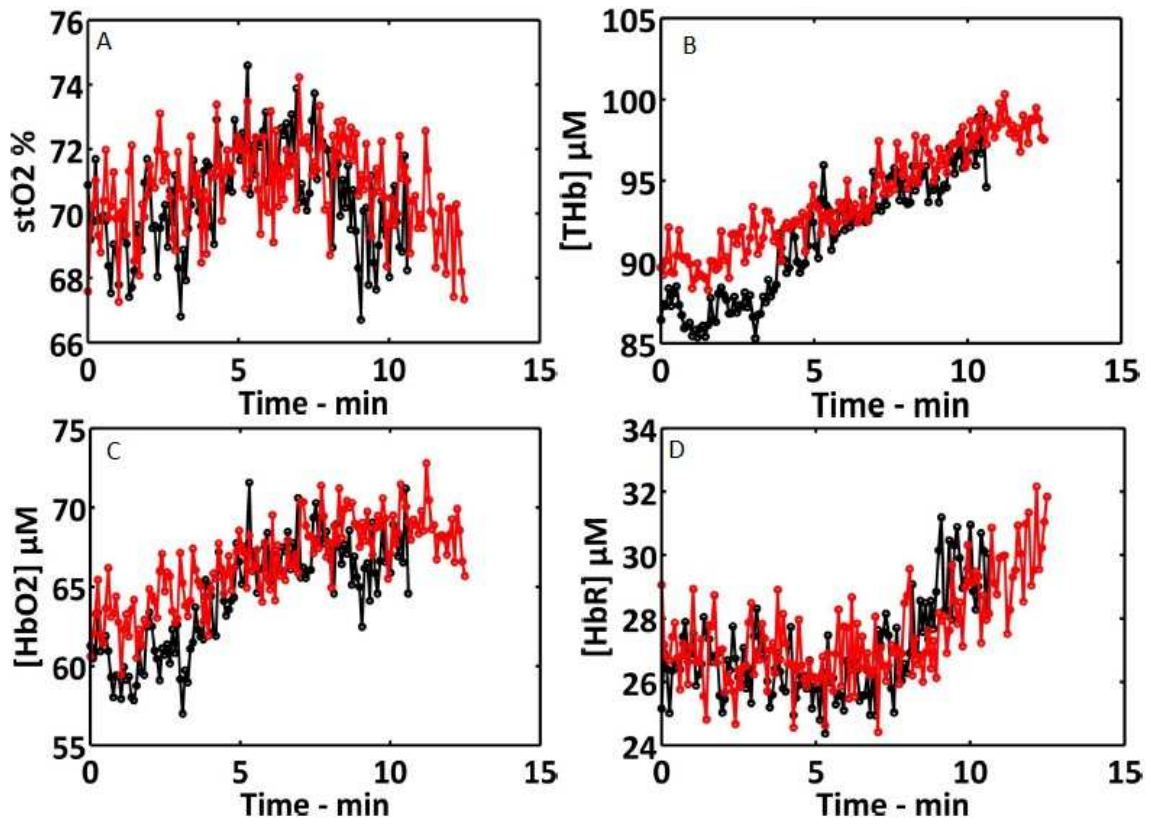


Figure 3.2: Raw tracings subject 2 Raw tracings of stO_2 (A), THb (B), $[HbO_2]$ (C), and $[HbR]$ (D) in one male subject before (black) and after (red) aerobic training.

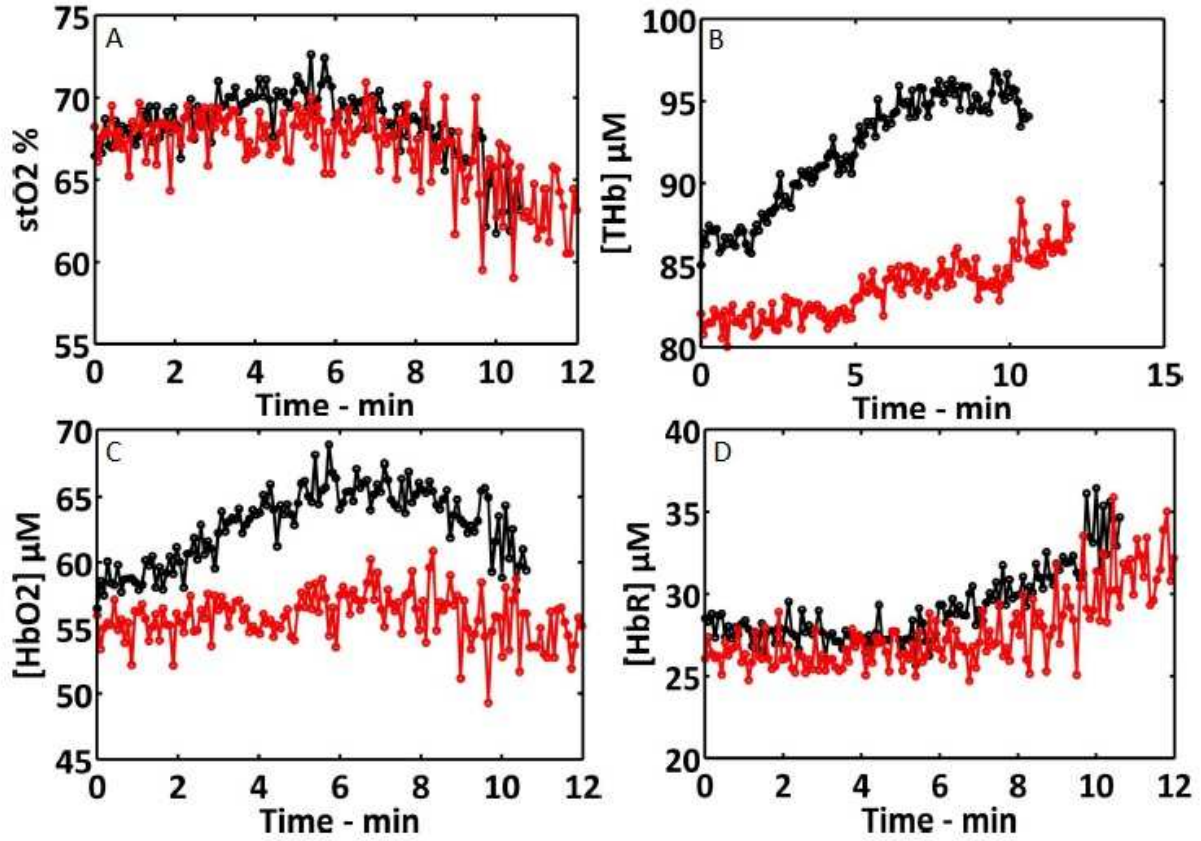


Figure 3.3: Raw tracings subject 3. Raw tracings of stO_2 (A), THb (B), $[HbO_2]$ (C), and $[HbR]$ (D) in one female subject before (black) and after (red) aerobic training.

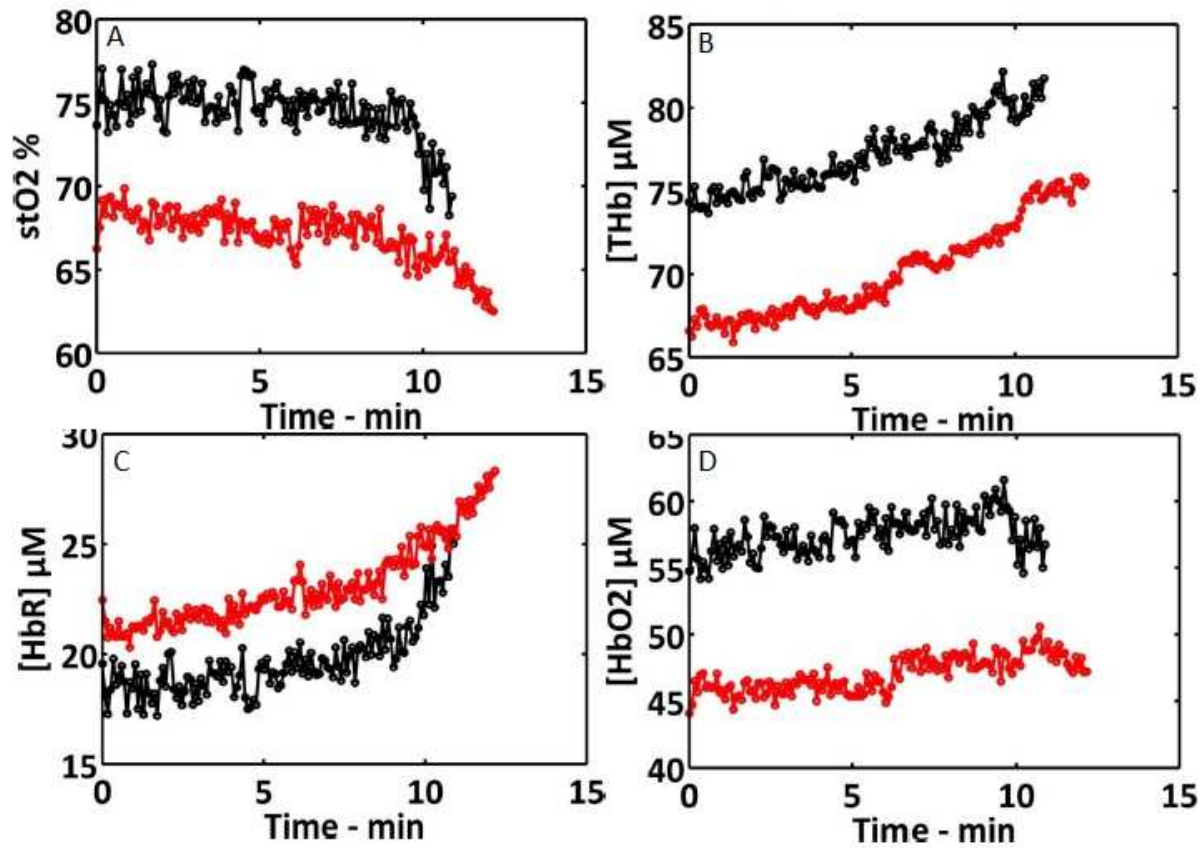


Figure 3.4: Raw tracings subject 4. Raw tracings of stO₂ (A), THb (B), [HbR] (C), and [HbO₂] (D) in one male subject before (black) and after (red) aerobic training.

The following plots show mean and standard error of the four parameters shown above for all 14 participants.

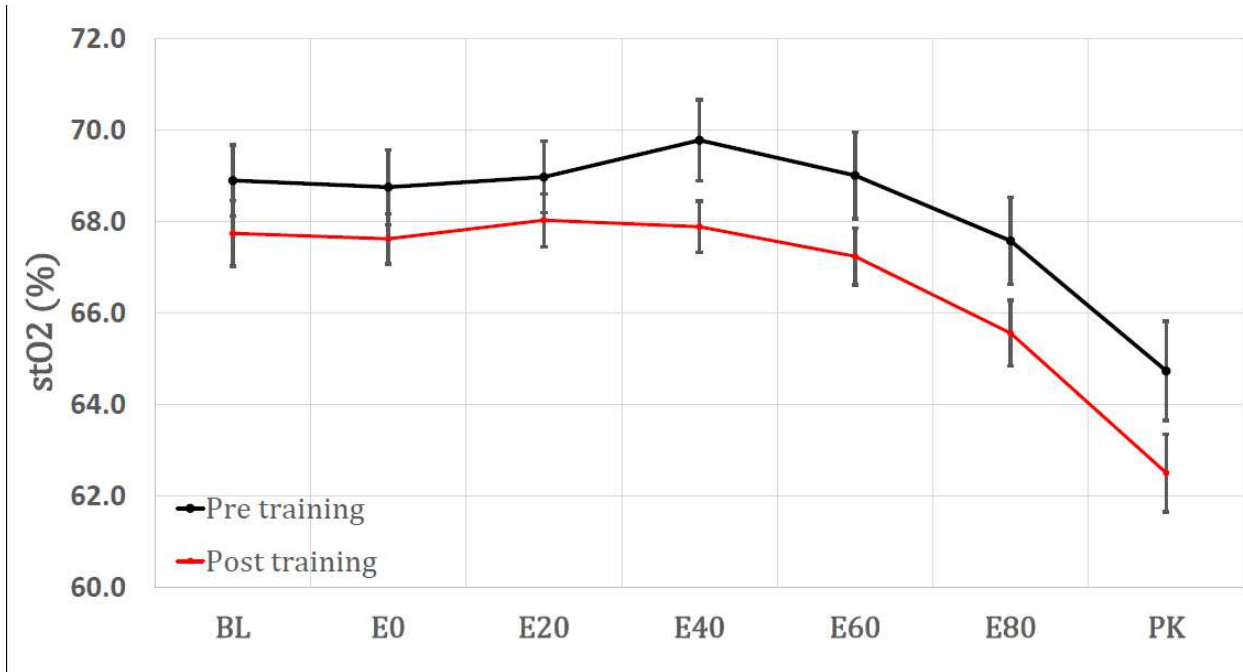


Figure 3.5: Training mean stO₂: Mean and SEM of stO₂ in all 14 subjects during incremental exercise pre (black) and post (red) training.

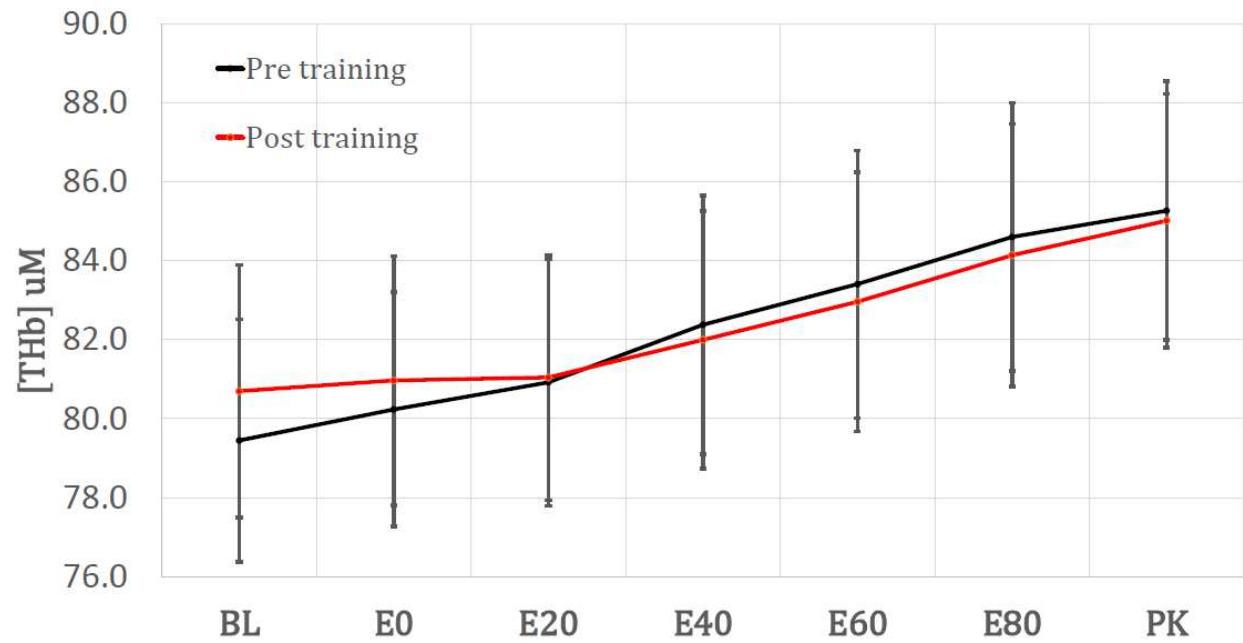


Figure 3.6: Training mean [THb]. Mean and SEM of [THb] in all 14 subjects during incremental exercise pre (black) and post (red) training

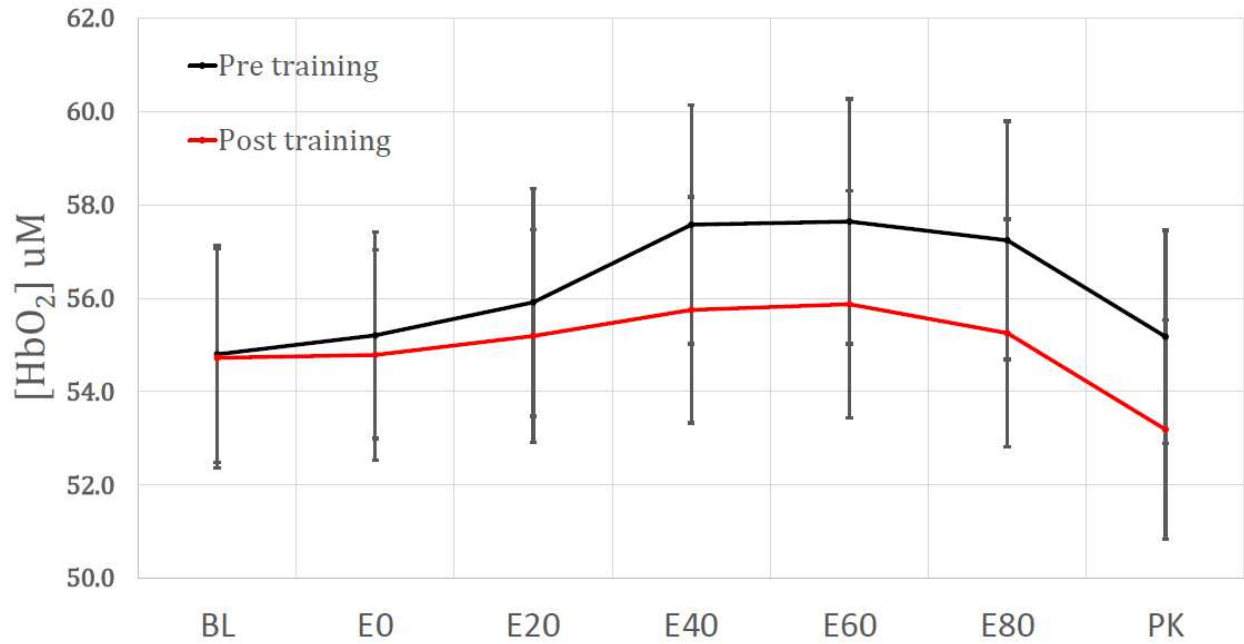


Figure 3.7: Training mean [HbO₂]. Mean and SEM of [HbO₂] in all 14 subjects during incremental exercise pre (black) and post (red) training

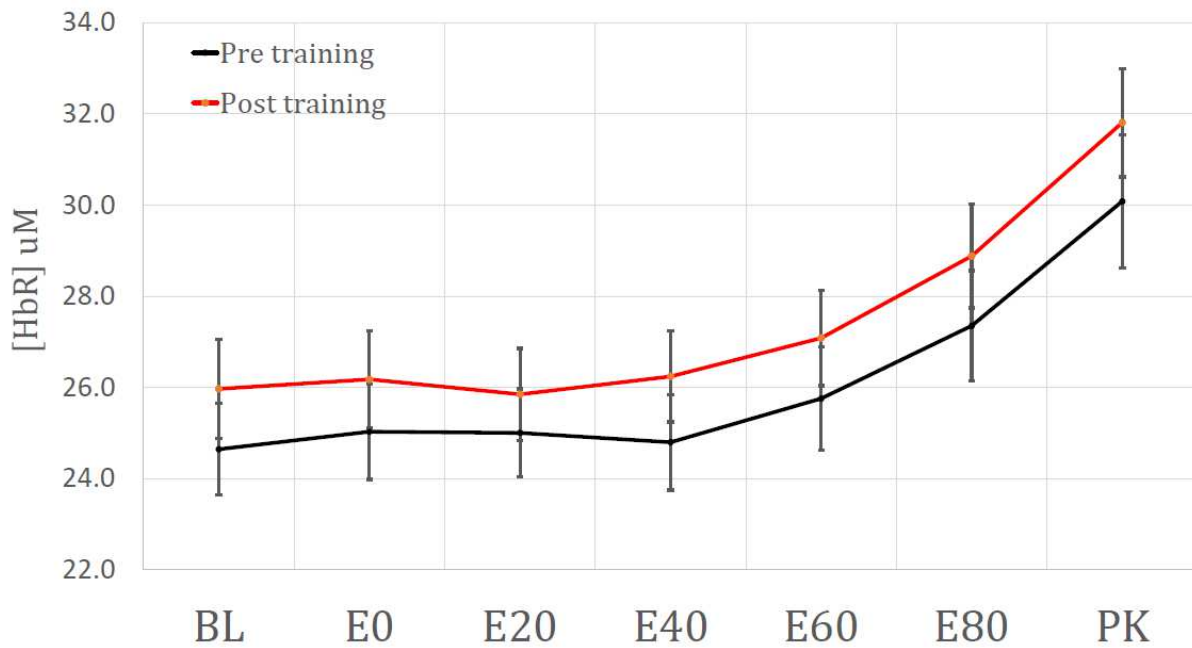


Figure 3.8: Training mean [HbR]. Mean and SEM of [HbR] in all 14 subjects during incremental exercise pre (black) and post (red) training

Two-way ANOVA revealed significant effects of exercise stage on all TR-NIRS parameters ($p < 0.001$ for all). However, there were only significant interactions between training status and exercise stage for $[\text{HbO}_2]$ ($F(6,78) = 3.851, p = .002$) and $[\text{THb}]$ ($F(6,78) = 3.98, p = 0.002$). There were no significant effects of training on either $[\text{HbR}]$ or stO_2 . In pre-training tests, stO_2 declined from BL to PK by $4.2 \pm 0.8\%$ ($p < 0.001$), and in post-training tests, it declined by $5.2 \pm 0.8\%$ ($p < 0.001$), but the difference between pre and post training declines was not significant. With regard to $[\text{HbR}]$, there was a mean increase of $5.4 \pm 0.3 \mu\text{M}$ from BL to PK pre training ($p < 0.001$). In post-training measurements, this increase was $5.8 \pm 0.3 \mu\text{M}$ ($p < 0.001$), but there was no difference between pre and post training responses. With regard to $[\text{HbO}_2]$, there was a significant increase in $[\text{HbO}_2]$ pre-training from BL to E60 ($+2.8 \pm 0.4 \mu\text{M}, p < 0.001$), but there was no such significant increase in post-training at any time point. However, post-training PK $[\text{HbO}_2]$ was significantly lower than the BL concentration ($-1.5 \pm 0.4 \mu\text{M}, p = 0.008$). $[\text{THb}]$ pre training increased from BL to PK by a mean of $5.8 \pm 0.3 \mu\text{M}$ ($p < 0.001$), whereas the post-training increase over the same interval was $4.3 \pm 0.3 \mu\text{M}$ ($p < 0.001$). In this case, the post-training increase in $[\text{THb}]$ was significantly lower ($p = 0.033$) than it was pre-training.

Regression analysis of $[\text{HbR}]$

As in the previous chapter, piecewise regression methods were applied to determine when during incremental exercise slope changes could be observed, specifically in tracings of $[\text{HbR}]$. In this case, the “segmented” package (108). First, $[\text{HbR}]$ data was

binned into approximately 20-second windows over the course of the entire incremental test. Then, using the segmented package, [HbR] from each incremental test was modeled using a three-phase linear approach. As shown in the following figure, the output of these models included optimal positions of breakpoints as well as confidence intervals for their position in time. In cases where the unsupervised algorithm did not produce a three-phase model, a version with two initial guesses for breakpoint positions was used.

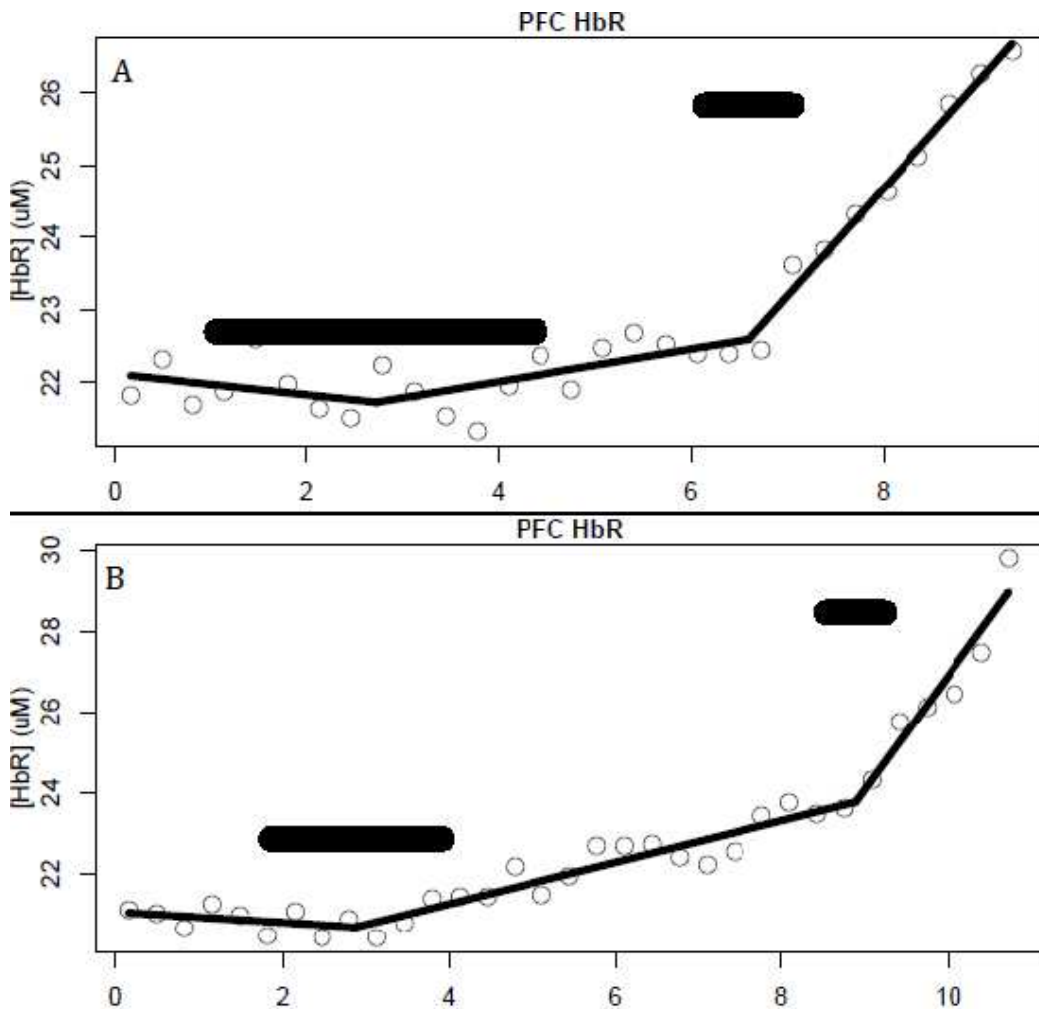


Figure 3.9: Segmented fits subject 1: Sample results from segmented regression of [HbR] in pre-training (A) and post-training (B) tests. Both are results of unsupervised application of segmented algorithm. The solid black bars indicate 95% confidence intervals of breakpoint position in time (x-axis). Note that post-training reflects a longer absolute time of exercise. The first and second transitions are clearly observed here.

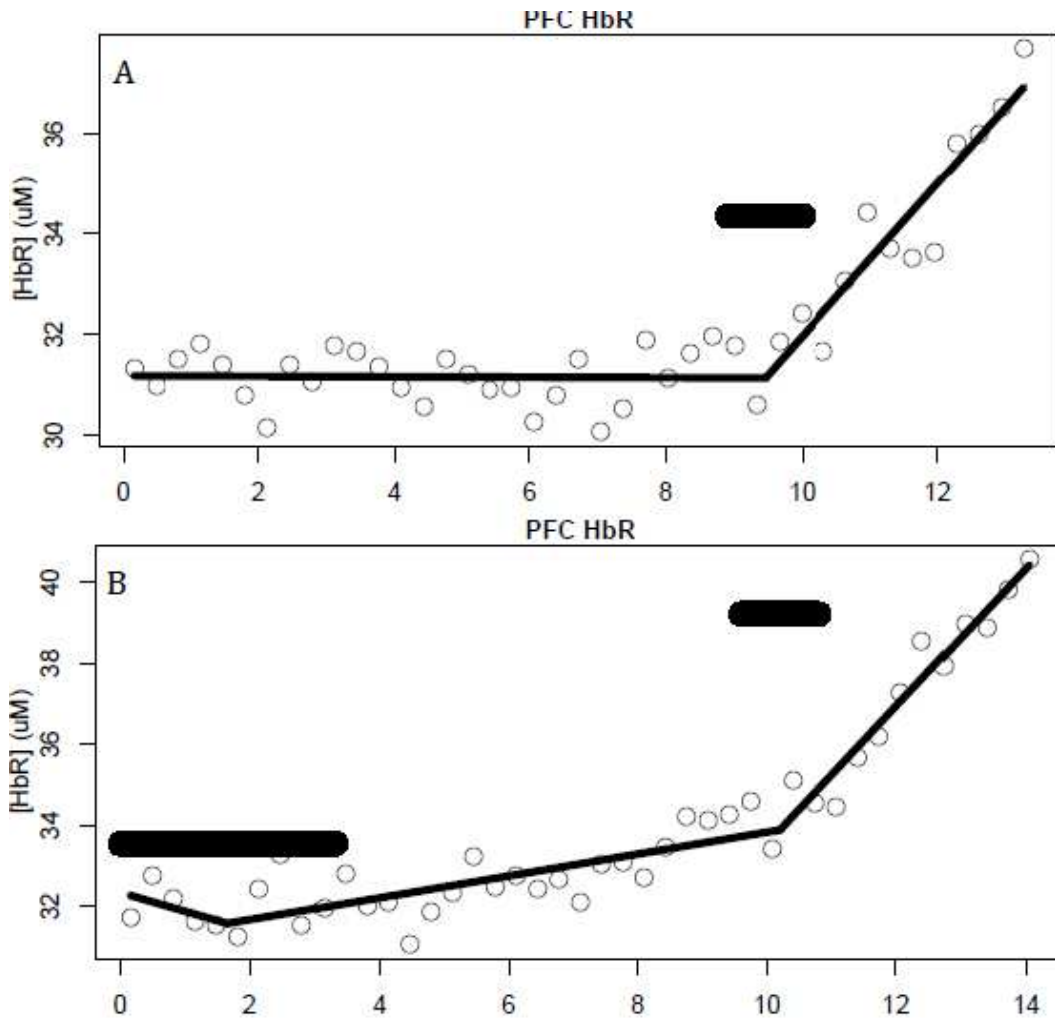


Figure 3.10: segmented fits subject 2. Pre-training (A) and post-training (B) [HbR] fits from a second subject. Note that in pre-training, only one breakpoint was observed, the final transition.

As figure 3.10 shows, there were some cases in which an early transition could not be identified. However, a late transition in [HbR], after which a consistent increase occurs until exhaustion is almost universally observed in this data set. Therefore, the placement and reliability of this final transition appears to be a particularly repeatable finding. Subsequent analysis on the occurrence of this breakpoint only was conducted.

Table 3.2 summarizes the relative time (as a fraction of total incremental test time) at which this final transition occurred in each subject pre and post training.

Table 3.2: [HbR] threshold times: Summary of relative timings of final [HbR] transitions in all subjects. Note that this method did not identify a transition in one subject pre-training, and in one subject post-training. There is no significant difference between mean values pre and post training by paired two-tailed t-test.

Final HbR Transition		
Subject	pre training	post training
1	0.833	0.723
2	0.719	0.826
3		0.745
4	0.672	0.744
5	0.737	0.732
6	0.713	0.787
7	0.881	0.621
8	0.959	0.849
9	0.850	0.878
10	0.794	0.755
11	0.597	0.669
12	0.753	
13	0.845	0.690
14	0.736	0.748
Mean	0.776	0.751
Std	0.097	0.071
SEM	0.027	0.020

Effect of constant scattering assumption

For this and subsequent analysis, all 28 studies were combined to address the questions of scattering changes with more power. By one-way repeated measures ANOVA, there were no significant effects of exercise intensity on scattering coefficients. However, when [THb] and stO₂ were analyzed using both FAD and FAC methods to determine effects of constant scattering assumption, there did appear to be differences. . For this analysis, all 28 studies (pre and post training) were combined to increase power. Two-way ANOVA revealed significant interactions between processing method and exercise intensity for both stO₂ (Figure 3.11, $F(6, 162) = 22.46, p < 0.001$), and [THb] (Figure 3.12, $F(6,162) = 13.15, p < 0.001$). At E60, FAD reports an stO₂ 0.6% lower than FAC ($p = 0.004$), 1.5% lower at E80 ($p < 0.001$), and 2.2% lower at PK ($p < 0.001$). For [THb], the FAD method resulted in higher reported values at E60 (2.0 μM higher, $p < 0.001$), E80 (4.0 μM higher, $p < 0.001$), and PK (4.2 μM higher, $p < 0.001$).

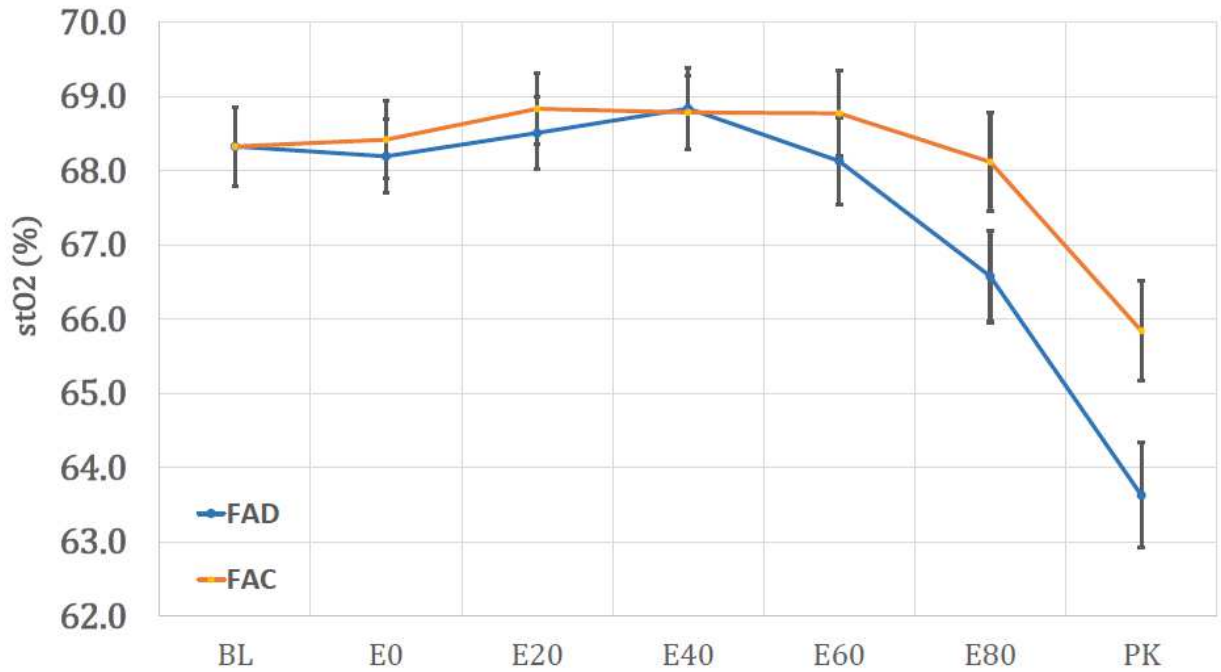


Figure 3.11: Effect of scattering assumption on stO₂: Mean stO₂ for all tests (n = 28) using the two processing methods, FAD (blue) and FAC (orange). FAD means the use of the full TPSF to characterize scattering and absorption continuously, whereas FAC means the assumption of constant scattering coefficients. Error bars reflect standard errors, and * denotes p < 0.05 between methods.

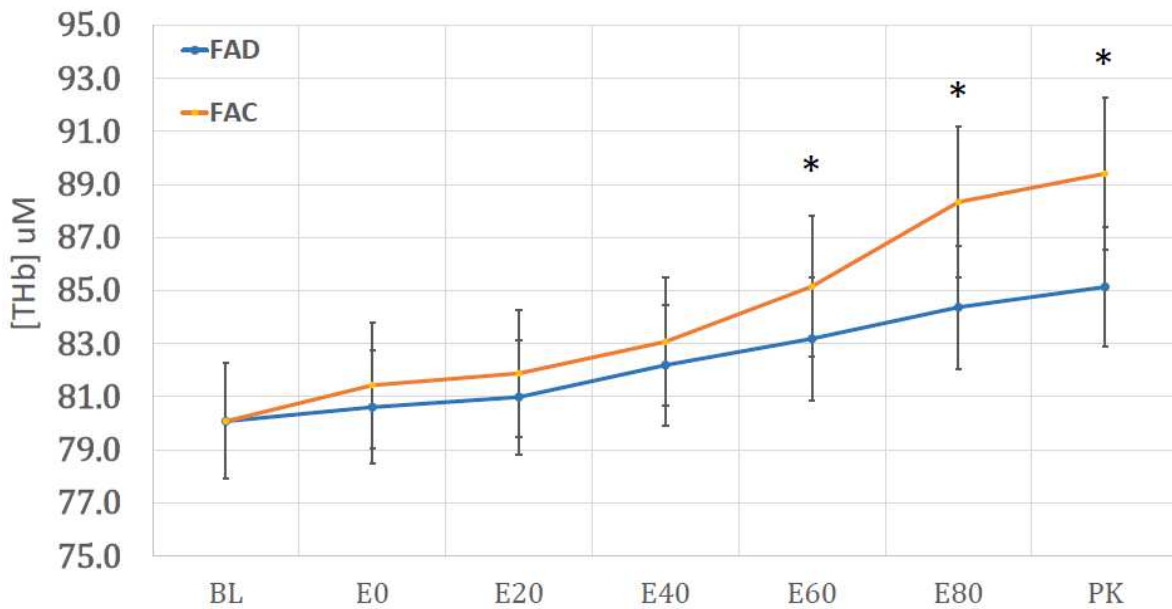


Figure 3.12: Effect of scattering assumption on [THb]: Same as above, but for [THb].

DISCUSSION

Effect of training

The principal finding from this data set is that while the period of training had a large and nearly uniform effect on the time spent during incremental exercise and the peak work rate, there appear to be only small changes in cerebral oxygenation. Indeed, it appears that the mean curve of [HbR] during incremental exercise for all subjects tested is merely shifted up to a higher concentration, with no significant difference due to training. Analysis of the relative position of the [HbR] transition late in exercise demonstrated no significant change in this parameter as well. However, this necessarily implies that that the [HbR] transition occurs at a higher absolute work rate on average. With regard to the other variables, there was also no significant effect of training on stO₂. Subjects experienced a decline in PFC stO₂ at PK stage, and there was no significant difference between the magnitude of this decline pre and post training.

The only hints of a difference between pre and post-training tests are two-fold: 1. In pre-training, there was a significant increase in [HbO₂] from BL to E60, whereas this was not observed post-training. 2. The change in [THb] from BL to PK was significantly higher pre-training than post-training. Finally, 3. There is a slightly but significantly higher mean [THb] at BL post training. The first observation runs in partial contradiction to one published study using a CW-NIRS device, in which the authors identified a relationship between increased training status and peak increase in [HbO₂] during incremental exercise

(110). However, this study was done in two separate groups of subjects, not in a population that underwent training and was measured both before and after the intervention (110). What we observed, quite to the contrary is a loss of any significant increase in [HbO₂] in the middle stages of exercise, with a preservation in the late-stage decline in [HbO₂]. This suggests perhaps that the increase in [HbO₂] with work intensity may be a feature of the untrained state, and its attenuation a phenomenon of vascular adaptation in the PFC. This is also suggested by the significantly lower BL-PK difference in PFC [THb] post-training, despite the achievement of significantly higher peak work rate. It is conceivable that eight weeks of training allow cerebral vasculature to more efficiently auto-regulate and prevent larger oscillations in [THb], and therefore blood volume. And finally, if one accepts that [THb] is a measure of cerebral blood volume (111), it appears that training is associated with slightly higher (1.2 μM higher, p = 0.003) PFC blood volume at baseline. This would suggest early increase in vascularization, potentially serving to enhance O₂ delivery to this part of the brain. This is important because multiple studies have suggested that exercise can have a pro-angiogenesis effect in various parts of the brain, in rats (112,113).

Another finding from the above-cited paper (110) was that the threshold for decline in oxygenation occurred at a higher absolute VO₂ in trained vs. untrained subjects. In fact, they used a late-exercise change in slope in a very similar way to determine the location of this threshold. However, the method used was visual inspection of the breakpoint position and agreement between multiple investigators (110). While this method of threshold determination is not preferable to the automated one used in this data set, it is nonetheless a finding corroborated by our data. Specifically, we observed that the [HbR] transition occurs at a higher absolute work rate during exercise after training, similar to the

published observations between training and untrained subjects (110). This adds weight to the argument that NIRS can be used to identify threshold events in exercise physiology that might have some utility in clinical monitoring of fitness and exercise effectiveness.

Effect of scattering changes

The results of the analysis of using the FAD and FAC processing method are somewhat more contradictory in this set of studies than in the previous chapter. While there are significant differences in the outcomes obtained by the two methods in the late stages of exercise, there are no significant changes in scattering coefficients themselves. This is in partial contradiction to the findings in the previous study. This might be explained by several factors. The first possibility is that the longer source-detector separation reduces sensitivity to scattering changes that are driven by changes in superficial tissues such as skin, and cerebro-spinal fluid which are known to contribute to scattering *in vivo* (114). The second possibility is simply variance in responses between subjects, which may be a factor considering the large degree of noise in measurements of scattering. And finally, given that there appears to be a trend toward a larger increase in scattering at 760 nm as opposed to the other wavelengths, it may be that there is a change in the wavelength dependence of scattering that is affecting the calculated concentrations (67).

Subsequent studies must examine this data more carefully to determine which, if any of these explanations are correct. One possible approach would be to try alternate

methods of fitting such as Monte Carlo to determine optical properties, and compare these to the FAD/FAC method.

Penetration depth of TR-NIRS signals

A persistent issue of concern in cerebral NIRS measurements is the degree to which signals are contaminated by superficial tissues (114). According to simulations using Monte Carlo methods, it is clear that time-domain methods can achieve sensitivity to cortical hemodynamics, and that this can be improved with technical advances (51). More recent studies have shown that TR-NIRS (specifically TRS-20) offers advantages in penetration depth over all commercial CW-NIRS systems compared to it (62). However, further studies with alternate instrumentation could be used to more firmly establish the sensitivity of TR-NIRS. Future studies should include an additional CW-NIRS system with shorter source-detector separation pairs to resolve superficial changes from deep ones. In this regard, we have collected some pilot data using a CW-NIRS system called PocketNIRS (Hamamatsu Photonics). Figure 3.13 shows the raw data from one such test.

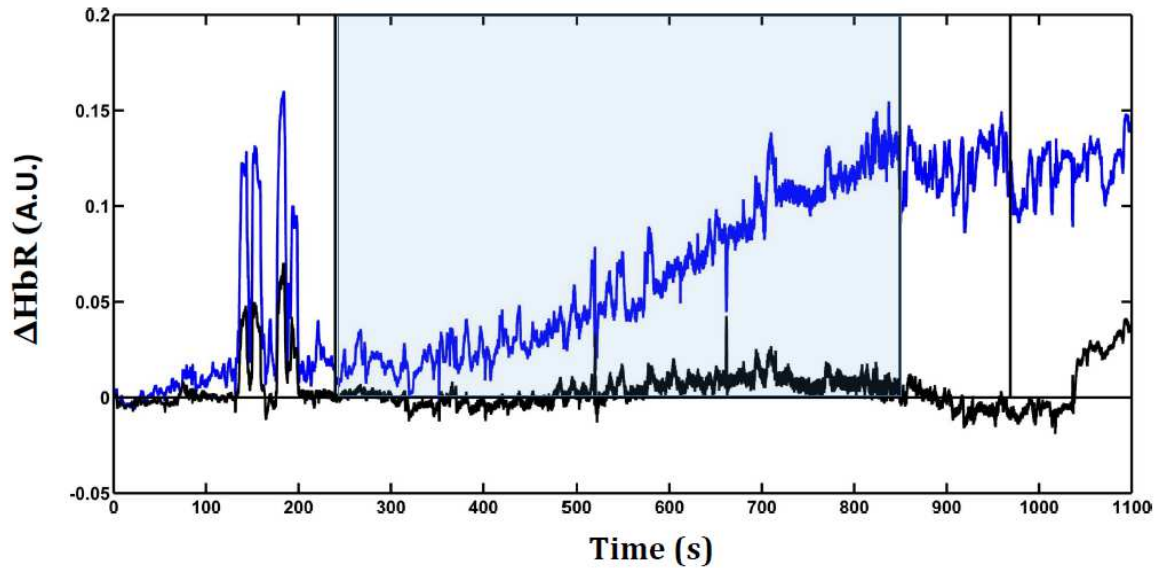


Figure 3.13 Deep and superficial CW-NIRS during exercise: Raw data from a pocketNIRS tracing of PFC oxygenation during incremental exercise. The blue tracing is from the left PFC using a 3-cm source-detector separation, whereas the black tracing is from the right PFC using a 1-cm separation. The y-axis units are in terms of relative change from baseline in [HbR], as the CW-NIRS is not capable of absolute quantitation.

As seen above, the short source-detector separation probe which is sensitive to a more superficial depth of light-tissue interactions sees very little change in [HbR] compared to the 3-cm separation channel. This would seem to indicate that using a 3-cm or 4-cm probe is likely enough to achieve sensitivity to cortical PFC dynamics. However, this finding must be repeated in many more subjects to more firmly establish it.

Segmented regression

The use of the segmented regression method is somewhat experimental in this context. As mentioned above, even recent studies of exercise physiology that identify thresholds tend to use methods such as visual inspection of optimal breakpoint values

(110). While these methods are not necessarily invalid, more quantitative methods would improve reproducibility and utility of these thresholds. There has been some development in this regard, with a recent paper that used a sequential manual segmented regression to identify NIRS thresholds (115). However, to our knowledge, there have been no published studies using the specific segmented regression method described here in exercise physiology. As far as this is true, this is a novel contribution of this set of studies to the field of tissue oxygenation in exercise.

CHAPTER 4: The effect of blood flow restriction on brain and muscle oxygenation during knee extension

RATIONALE

The following consists largely of a published manuscript in the journal *Medicine and Science in Sports and Exercise*, of which the author of the present work is also the primary author(116). In recent years, considerable attention has been drawn to the potential utility of blood flow restriction (BFR) in enhancing the skeletal muscle response to resistance exercise. Exercise with BFR, often referred to as Kaatsu training, has been shown to cause significantly larger increases in muscle size and power compared to non-BFR resistance exercise of comparable intensity/duration (117,118). American College of Sports Medicine guidelines recommend sets of exercise at 70-85% of 1-repetition maximum (1RM) to achieve hypertrophy in novices or intermediates (118), whereas it has been shown that even intensities as low as 20% of 1RM can induce hypertrophy with concomitant BFR (119). This observation and many subsequent published findings point to the utility of BFR in rehabilitation, especially in treatment of disuse atrophy of muscle (120,121), and in the prevention of muscle loss due to aging and its comorbidities(122).

The specific mechanisms for these enhancements with BFR are being actively investigated, and several proteins that may play a role have been identified, such as mammalian target of rapamycin (m-TOR), heat shock proteins, and nitric oxide synthase. It is thought that the prevention of metabolite clearance from the exercising muscle causes an enhancement of signaling along these pathways (123). Independent of specific molecular

signaling, it is likely that muscle oxygenation kinetics and perfusion play a role in initiating activity in these pathways.

Near-Infrared Spectroscopy (NIRS) is a non-invasive optical method used to dynamically measure tissue content of oxy- and deoxyhemoglobin ($[HbO_2]$ and $[HbR]$), which together reflect the balance between blood flow and oxygen uptake, and has numerous applications in exercise medicine and sports science (124). Considerable work has been done to characterize NIRS response profiles of muscles in a variety of resistance exercise conditions (125) (126). There have also been some studies that have used NIRS to assess cerebral hemodynamics during resistance exercise (127). Due to the available range of available commercial instrumentation, most studies (such as those mentioned above) have utilized continuous wave (CW) NIRS techniques (125), which only report relative changes in tissue hemoglobin concentration and oxygen saturation. In contrast to CW-NIRS, time-resolved NIRS (TR-NIRS) is able to quantitatively separate light absorption from scattering and measure absolute concentrations of tissue oxy- and deoxyhemoglobin. This is accomplished by measuring and fitting the temporal point spread function (TPSF) of remitted light signals to a computational model of light transport in tissue (60). These features make TR-NIRS particularly attractive for the current study because it allows compensation for factors that can diminish the accuracy of hemodynamic measurements, such as differences in path length and scattering (83) secondary to large changes in blood volume.

To gain insight into potential physiological mechanisms for the effect of BFR, we conducted a study of isokinetic knee extension exercise with and without partial BFR (occlusion pressure of 100 mm Hg) using a commercial TR-NIRS oximeter (TRS-20,

Hamamatsu KK, Japan) (61). Two independent measurement channels were used to simultaneously assess the oxygenation dynamics of the exercising muscle and the prefrontal cortex (PFC). For the muscle studies, we chose to measure oxygenation of the oblique fibers of the vastus medialis muscle (VMO). These muscle fibers insert medially on the patella and are thought to be important in preventing injuries such as subluxation and lateral displacement of the patella and in the assessment of patello-femoral pain syndrome (128,129). There have been efforts to study the VMO using EMG (130), but no published studies to our knowledge that have used NIRS or related techniques to examine oxygenation of the VMO during knee extension exercise. There is ongoing interest in whether therapeutic interventions can specifically target the VMO for hypertrophy (131).

While local metabolic fatigue is certainly a determinant of overall work performance at the skeletal muscle level, in recent years growing attention has been directed towards the regulatory effect of the central nervous system on effort and fatigue during exercise (21,132). Blood flow and oxygenation kinetics of critical cerebral areas, such as the prefrontal cortex (PFC), have been hypothesized as possible determinants of compliance in exercise regimens and in the ability to sustain longer exercise challenges in general (133). This may be especially relevant during conditions of BFR when the subjective perception of fatigue is amplified. While NIRS techniques have been employed in this area of research as well, most published studies also rely on CW-NIRS techniques (21,95,96). We hypothesized that exercising under BFR conditions would: a) produce a significant increase in [THb] and [HbR], as well as a drop in O₂ saturation (stO₂, the ratio of [HbO₂]/[THb]) in the VMO, and b) create a “metabolic activation” pattern (i.e. [HbR] profile) similar to that present in non-BFR fatigue (i.e. obtained with a much higher workload) in the PFC.

Methods

This study was conducted under an institutional-approved human subjects protocol and carried out in the Human Performance Laboratory (HPL) at the University of California, Irvine (Irvine, CA). For these studies, a total of 7 healthy male subjects were recruited, and each provided written informed consent. This study required three separate visits to the HPL not including a preliminary consent/familiarization session.

Familiarization period

Each subject was familiarized with all elements of the experimental protocol before the first testing condition. During the first visit to the HPL, body mass and resting blood pressure were measured and each subject was screened for possible contraindications to exercise. The Biodex dynamometer (System 3, Biodex Corp., Shirley, NY) was used for all exercise sessions and measurements. Isokinetic extension of the dominant knee joint was conducted at an angular velocity of 30° per second with a range of motion (ROM) of 90° (90° of flexion to full extension). Maximal torque production for knee extension (1 repetition maximum, 1RM) was obtained from the highest torque produced during five repetitions at maximal exertion. Subjects were familiarized with the Biodex real-time visual feedback of peak torque production until they could reliably produce torque as close to 50% of 1RM as possible, which was used for all testing conditions in the three subsequent visits.

Testing visits

Testing sessions were conducted during early morning hours in a fasted state. The three conditions for this exercise study are as follows: 1) exercise to volitional fatigue with blood-flow restriction (BFR), 2) exercise without BFR matched to the number of repetitions from the BFR condition (Matched), and 3) without BFR to fatigue (Fatigue). The subjects were randomly chosen to perform the three conditions in one of two orders: 1) BFR, Matched, Fatigue or 2) Fatigue, BFR, Matched. Each of these conditions were conducted on separate visits, separated by at least 48 hours. Before each exercise condition, after the baseline oxygenation was assessed for several minutes, the subjects performed a brief warm-up. Rest periods between sets were 90 seconds and the minimum number of repetitions per set was 10. For the BFR and Fatigue conditions, sets were terminated when two consecutive repetitions produced torque more than >10% lower than 50% 1RM. For the BFR condition, an 85 cm-long segmental occlusion cuff was wrapped around the proximal thigh and connected to a rapid inflator (E20 Rapid Cuff Inflator, Hokanson Inc.). The occlusion pressure was set to 100 mm Hg in order to achieve sub-systolic vascular occlusion. Cuff inflation occurred 30 seconds before the start of the first set with pressure being maintained during all exercise sets and rest periods. Immediately after cessation of the third set, the cuff was deflated. The number of repetitions achieved during the BFR condition was used to determine the number of repetitions in the Matched condition. The protocol for the Fatigue condition was identical to that for BFR except with the absence of the occlusion. At the end of each exercise set,

subjects were asked to provide a rating of perceived exertion (RPE), expressed as a number between 6 and 20 (134). One subject was excluded from data analysis, due to failure to adequately follow experimental instructions regarding consistent torque production.

TR-NIRS Measurements

Prior to exercise testing, TRS-20 silicone fiber holders were placed over the VMO and PFC (superolateral forehead), and secured directly to the skin with double-sided clear tape. The VMO probe was further secured with overlying tape and the PFC probe with an elastic headband to prevent motion and maintain consistent tissue contact. The probe was aligned parallel to the muscle fibers. Source-detector separation was 30mm for the VMO and 40mm for the PFC. Continuous measurements were made with ensemble averaging approximately three seconds to ensure adequate signal-to-noise ratio. TR-NIRS, as implemented in the TRS-20 and described in a recent publication (61), uses a single-photon counting method with photomultiplier tubes to record individual pulses reflected from tissue in a semi-infinite mode. From the raw reflected pulse, the intensity of reflectance, mean path length and absorbance change can all be derived without model assumptions. Then, a least-squared method is used to fit a curve derived from the diffusion equation to the obtained reflectance, and this allows the determination of reduced scattering coefficient (μ_s') and absorption coefficient (μ_a). From absorption coefficients, pathlength calculations, and known molar extinction coefficients at the three wavelengths, concentrations of oxyhemoglobin ([HbO₂]), deoxyhemoglobin ([HbR]), total hemoglobin ([THb]), and

oxygen saturation (stO_2) were calculated using the Beer-Lambert law(61). stO_2 is defined as the ratio of $[HbO_2]/[THb]$, expressed as a percentage.

Data Analysis

Repetitions, RPE, and total work output were recorded and tabulated for each set. All TR-NIRS output variables ($[HbR]$, $[HbO_2]$, $[THb]$, and stO_2) were averaged for the baseline period, all sets, and all rest periods in both tissues. Average values were calculated for each set and rest period and tabulated using Prism (Version 6, Graphpad Software, San Diego, CA.). The same program was also used for ANOVA and subsequent Bonferroni-corrected multiple comparisons. Mean optical path length (PL) and μ_s' at 796 nm in VMO were also analyzed using coefficients of variation (CV) calculated over the course of the whole exercise challenge in the BFR and Matched conditions. CV values were compared between conditions using paired, two-tailed t-test. For analysis of oxygenation kinetics, $[HbO_2]$ and $[HbR]$ for the first set and recovery period of exercise by each subject were imported to MATLAB (Version R2013A, Mathworks). The beginning of the rapid phase of deoxygenation for both $[HbR]$ and $[HbO_2]$ was identified and used as the starting point for subsequent fitting. The Shape Language Modeling tool (SLM, D'Errico, John. (2009) Shape Language Modeling. <http://www.mathworks.com/matlabcentral/fileexchange/24443>. Retrieved 2/19/2013) was used to apply a sequential piecewise linear model to each $[HbO_2]$ and $[HbR]$ curve. We chose to apply this method in the first set and recovery because it was the longest set in repetitions, and it would allow for determination of the effect of BFR independent of any prolonged effects of occlusion. The output of each of these

fits is an R-squared value, and a series of “breakpoints” (BP) time t , which represent the optimized times (and corresponding concentrations) of transition between the phases. Using this approach, [HbR] and [HbO₂] were modeled as following two-phase kinetics during both exercise and recovery: an initial fast phase, followed by a longer, and slower second phase. The values for fit parameters (transition concentrations and rapid-phase slopes) were averaged for all subjects across two conditions (BFR and Matched, the conditions in which overall timing was similar due to similar number of repetitions) and compared using paired, two-tailed t-tests.

RESULTS

Exercise Parameters

Both repetitions and work output demonstrated significant F-values with respect to experimental condition and the RPE demonstrated a significant interaction between conditions and sets (Figure 4.1). The Fatigue condition was associated with a significantly higher number of repetitions (Fig. 1A, $p < 0.001$), and therefore higher total work (Fig. 4.1B). There was not a significant difference in work output between BFR and matched conditions (Fig. 4.1B). BFR was associated with a significantly higher RPE (Fig 4.1C) than the Matched condition for all sets (16.8 v. 13.6 for set 1, 18.4 v. 12.8 for set 2, and 18.6 v.

13.0 for set 3, $p < 0.0001$), but only higher than the Fatigue condition in set 2 (18.4 v. 16.8, $p = 0.0128$).

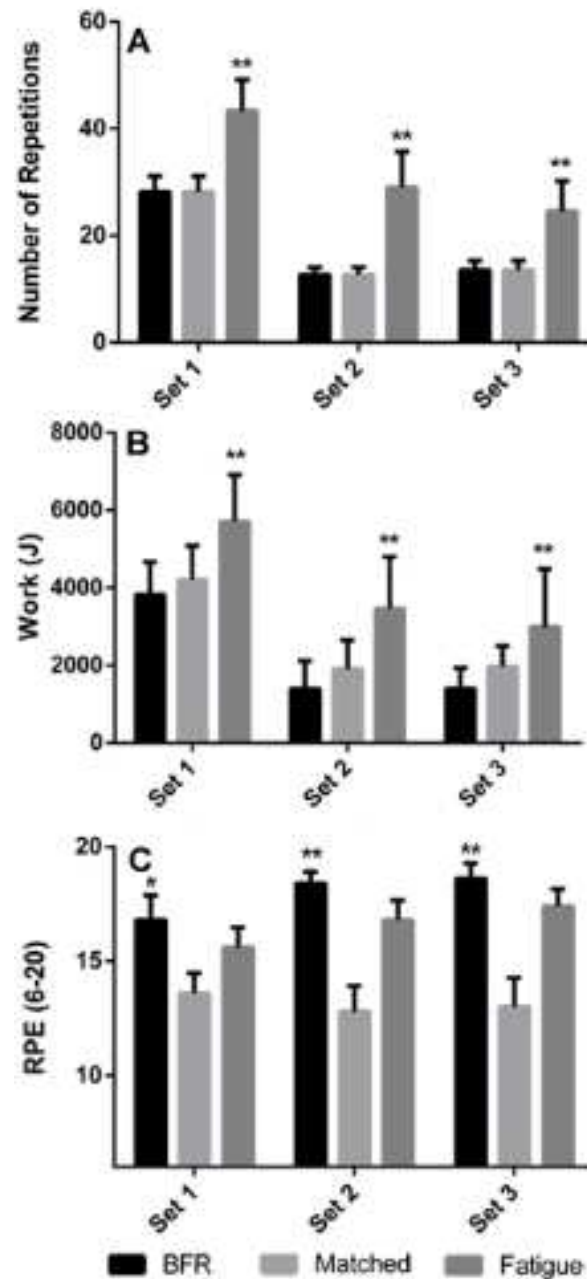


Figure 4.1 Exercise parameters: Average number of repetitions (A), total work output (B), and response to rating of perceived exertion (RPE) scale (C) for each set averaged for all subjects. For RPE, subject 1 was excluded due to missing data points. All variables were analyzed using two-way repeated measures ANOVA, with post-hoc multiple comparisons with Bonferroni correction. In (C), * denotes the BFR condition is significantly different from

the matched, whereas ** denotes BFR as significantly different from both other conditions.

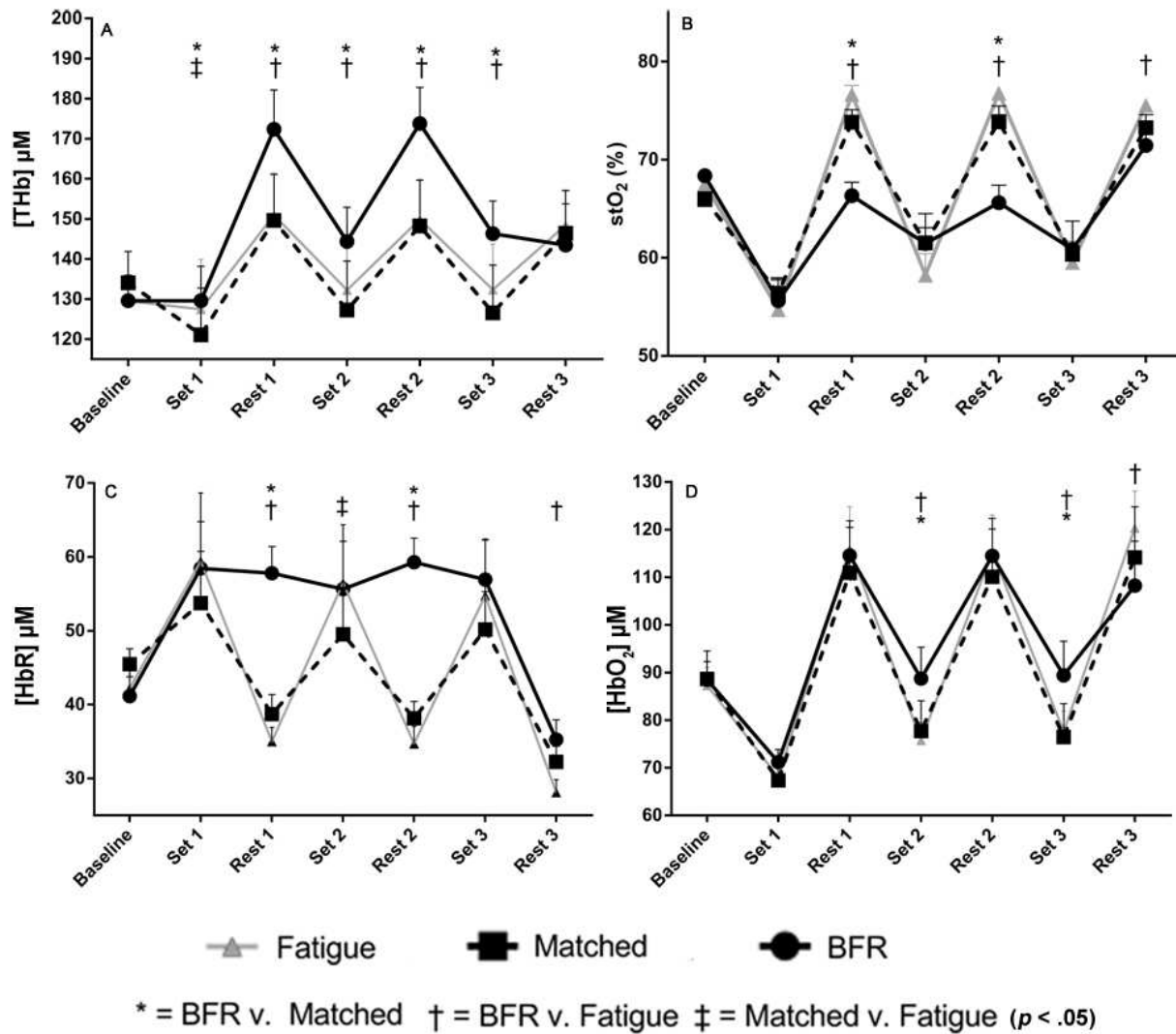


Figure 4.2: VMO Oxygenation Average absolute [THb] (A), stO_2 (B), [HbO₂] (C), and [HbR] (D) in the VM0 muscle. Data analyzed using two-way repeated measures ANOVA with post-hoc Bonferroni-corrected multiple comparisons. Event markers entered into TRS-20 during testing were used to divide data into stages. In BFR condition, occlusion pressure of 100 mm Hg was applied 30 s before start of Set 1, and released immediately at the end of set 3.

VMO Oxygenation

In figure 4.2, average values for each stage of exercise across six subjects are shown. For all four variables, there were significant F-values for interaction between exercise condition and stage of exercise. BFR exercise was associated with a significantly higher average [THb] than other conditions at each stage from the first rest period until the end of the third set when occlusion was released ($p < 0.001$ in all cases, Fig. 4.2A). During rest periods 1 and 2, this was driven by a significantly higher [HbR] in exercise with BFR over other conditions (Fig. 4.2C, BFR v. Fatigue: rest 1 and rest 2 ($p < 0.001$ for both), BFR v. Matched: rest 1 and rest 2 ($p < 0.001$)). During sets 2 and 3, the increased [THb] was driven by a higher [HbO₂] (Fig. 4.2D, set 2 and set 3: BFR vs. Matched and Fatigue, $p < 0.01$ for all). The average [HbO₂] was also significantly higher in the Fatigue condition than the BFR condition in the third rest period ($p < 0.001$), after the release of the occlusion. BFR was associated with a nearly 10% lower average stO₂ during rest periods 1 and 2 than the other conditions (Fig. 4.2B, $p < 0.001$ in both cases). Reduced scattering coefficient (μ_s') and PL at 796 nm were also analyzed in the BFR and Matched conditions. It was found that the CV for PL was significantly higher for BFR than Matched condition over the whole duration of exercise (4.9% v. 3.0%, $p = 0.002$). There was also a trend toward a difference in CV of μ_s' at 796 nm, but it did not reach statistical significance (6.0% for BFR v. 4.0% Matched, $p = 0.09$). Finally, in comparison with the Matched condition, the percentage change in PL from baseline to final recovery was different (-2.7% BFR v. -0.6% Matched, $p = 0.03$).

Two-Phase Linear Fitting Results

Figure 4.3 shows representative results from a single subject for two-phase piecewise linear fitting of [HbO₂] and [HbR] during set 1 and rest 1. Panels A and B show data for [HbO₂] in Matched and BFR conditions, respectively, whereas panels C and D show [HbR] fits in the same conditions. For all variables, the slope and duration of the rapid first phase (phase 1) and the concentration at the transition between phases during both exercise and recovery were analyzed, as shown in Table 4.1. In subject 6, the rapid phases in [HbO₂] seemed to occur faster than the measurement time of the TRS (3 s) and therefore parameters for this phase were not included in the analysis. Significantly different fit parameters were identified in analysis of [HbR] during rest 1. Specifically, the concentrations at which both rapid and slow phases of [HbR] clearance began were higher in the presence of BFR ($p = 0.029$ and $p = 0.011$ respectively). This reflected the fact that in BFR, the rapid phase of [HbR] clearance during recovery was preceded by a “spike” of [HbR] contributing to the higher average concentration (Fig. 4.2C). To accommodate this, an extra breakpoint was included in the fitting procedure for the BFR condition. This [HbR] “spike” was detected in all six subjects analyzed in the BFR condition and to some extent in the Matched condition for only 2 subjects. For [HbO₂] during recovery, the duration of the first phase was significantly longer in BFR vs. Matched conditions (51 vs. 31 s, $p = 0.047$). However, the slope of [HbO₂] increase was also significantly lower (56 vs. 89 $\mu\text{M/s}$, $p = 0.004$). Finally, in the BFR condition (but not Matched) there was a correlation between the magnitude of increase in [THb] from first set exercise to recovery, and the slope of rapid-phase clearance of [HbR] during recovery ($r = -0.88$, $p = 0.02$).

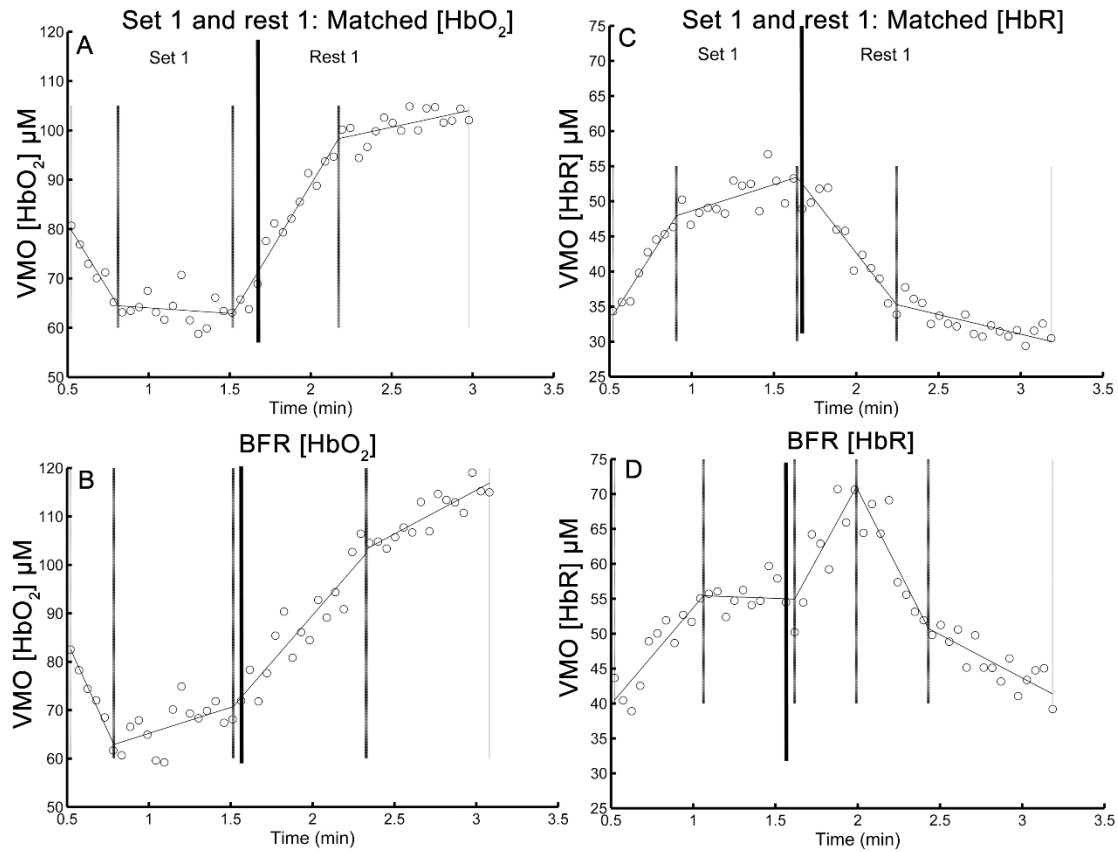


Figure 4.3: Piecewise fits in one subject: Representative single-subject results of Shape-Language Modeling (SLM) results using piecewise linear spline fitting of the first set and rest periods. A and B show the results of [HbO₂] fitting for Matched (A, $R^2 = 0.952$) and BFR conditions (C, $R^2 = 0.888$). B and D show results of [HbR] fitting for Matched (C, $R^2 = 0.976$) and BFR (D, $R^2 = 0.965$). Solid black lines represent event markers for division between exercise and recovery. Vertical narrow lines represent the position in time of optimally-fitted breakpoints between linear phases. The circles represent raw data points, and the solid lines represent the fitted linear segments.

Table 4.1: Summary of regression results: Summary of average \pm SEM of fitting parameters for all subjects for the first set and rest periods. Paired, 2-tailed t-tests were used to compare mean values between 2 conditions, BFR and matched. P-values for significant differences are underlined.

	<u>Condition</u>	Initial conc. (μM)		First phase duration (s)		Transition conc. (μM)		First phase slope ($\mu\text{M/s}$)	
		BFR	Matched	BFR	Matched	BFR	Matched	BFR	Matched
[HbR] set 1 (average $R^2 = .895$)	Average \pm SEM	40 \pm 4	34 \pm 4	25 \pm 5	30 \pm 7	60 \pm 7	56 \pm 7	69 \pm 29	63 \pm 20
	p-Value		0.059		0.330		0.187		0.599
[HbR] rest 1 (average $R^2 = .940$)	Average \pm SEM	81 \pm 8	62 \pm 6	25 \pm 5	27 \pm 7	58 \pm 5	37 \pm 3	-62 \pm 13	-57 \pm 9
	p-Value		<u>0.029</u>		0.781		<u>0.011</u>		0.717
[HbO₂] set 1 (average $R^2 = .959$)	Average \pm SEM	93 \pm 4	88 \pm 7	15 \pm 2	17 \pm 2	65 \pm 4	63 \pm 5	-133 \pm 48	-94 \pm 27
	p-Value		0.371		0.296 #		0.638		0.279 #
[HbO₂] rest 1 (average $R^2 = .977$)	Average \pm SEM	71 \pm 2	67 \pm 4	51 \pm 7	31 \pm 2	114 \pm 9	111 \pm 9	56 \pm 10	89 \pm 14
	p-Value		0.307		<u>0.047</u> #		0.441		<u>0.004</u> #

one subject was excluded from this comparison because the fitted first phase was shorter than the TRS-20 measurement interval

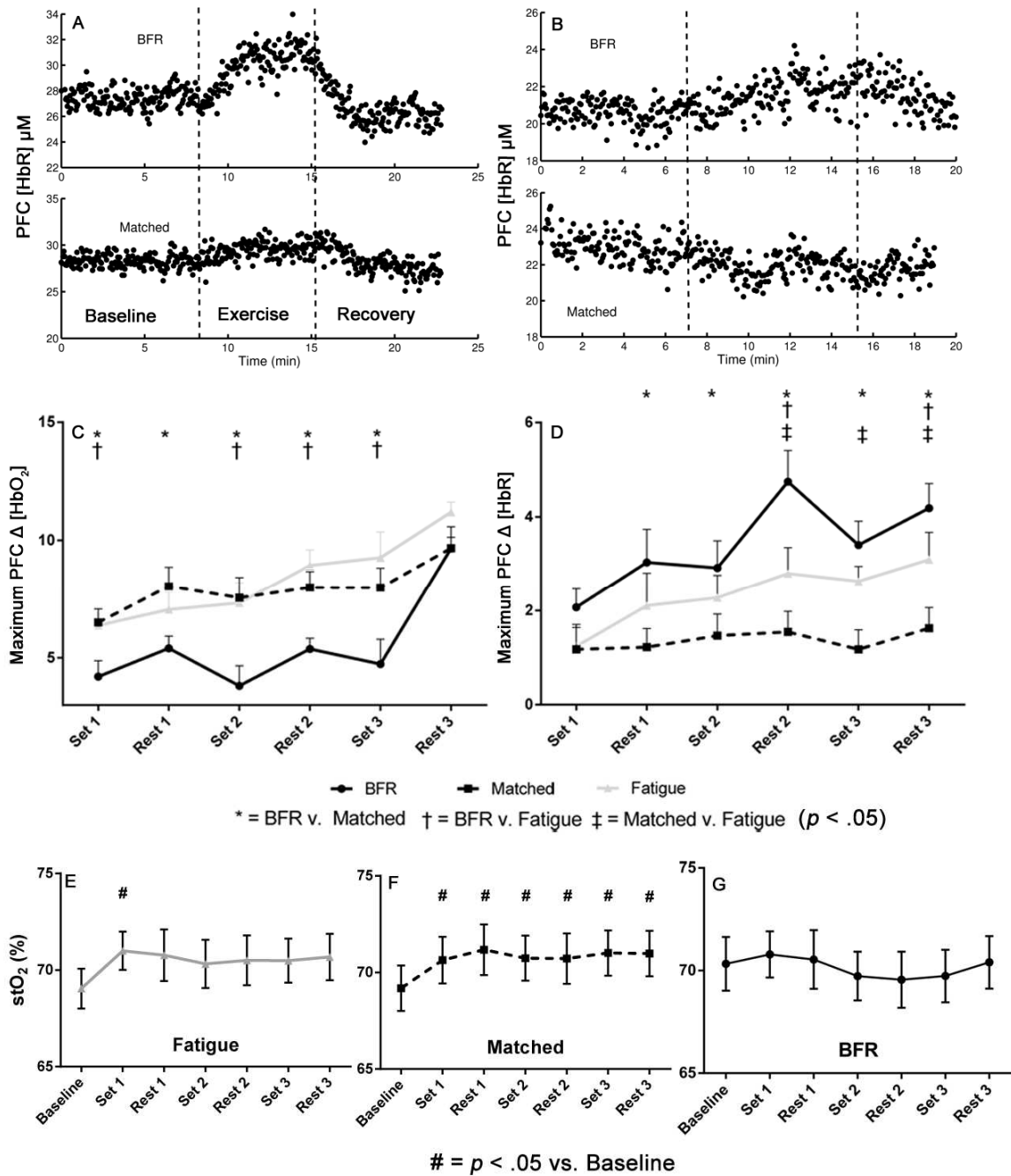


Figure 4.4: PFC Oxygenation changes: (A) and (B) demonstrate sample tracings in two subjects for [HbR] in BFR (above) and matched (below) conditions. For each exercise stage, the single-measurement maximal difference from the corresponding average baseline value was calculated for [HbO₂] (C) and [HbR] (D). BFR was associated with a higher maximum increase in [HbR], and a lower maximum increase in [HbO₂] than the other conditions. (E)-(G) show average stO₂ values at each stage of exercise, with conditions separated and analyzed using repeated measures one way ANOVA. (*) indicates significant difference when compared to baseline value. (E) shows data for BFR condition, (F) for matched, and (G) for fatigue.

PFC Oxygenation

Figure 4.4 shows results for PFC oxygenation parameters. Panels A and B show representative BFR and Matched raw data for [HbR] in two subjects, with the whole three sets of exercise shown by dashed lines. Generally, exercise was associated with small but consistent increases in both PFC [HbR] and [HbO₂], as shown by maximal changes from baseline (Δ [HbR] and Δ [HbO₂]) in figure panels 4.4C and 4.4D. The BFR condition was associated with a significantly lower Δ [HbO₂] than the Matched and Fatigue conditions during all sets (Fig. 4.4C), as well as the second rest period ($p < 0.01$ for all). During the first rest period, the Δ [HbO₂] was lower in BFR than in Matched ($p = 0.0008$). BFR was associated with a significantly higher Δ [HbR] (Fig. 4.4D) than Matched during the first rest period and all subsequent stages (and $p = 0.001$ for set 2, $p < 0.001$ for others). Δ [HbR] was higher in BFR than Fatigue during rests 2 and 3 as well ($p < 0.001$ and $p = 0.02$ respectively). Panels E-G show average absolute stO₂ at each experimental stage, with conditions analyzed separately by one-way ANOVA, and post-hoc Dunnett's test against baseline values. For Fatigue (Fig. 4.4E), there was a significant increase in stO₂ during set 1 ($p = 0.0176$). For the Matched condition (Fig. 4.4F), stO₂ at every stage was higher than at baseline ($p < .01$ for all). There were no PFC stO₂ changes with BFR (Fig. 4.4G).

DISCUSSION

VMO Oxygenation

We have assessed tissue hemoglobin content and oxygenation using TR-NIRS with and without BFR in order to understand the effects of occlusion on muscle oxygenation during knee extension. The typical patterns observed during NIRS measurements of exercising muscles are shown in the Matched condition in Figure 4.3. Exercise is associated with increased [HbR] and reduced [HbO₂], with both reversing during recovery. Recovery is associated with a hyperemic supra-exercise [HbO₂] and stO₂, due to both vasodilation and increased demand to pay back O₂ deficit. [HbR] and [HbO₂] together reflect the balance between O₂ utilization and muscle blood flow (84). To our knowledge, there are few published studies of muscle oxygenation during BFR exercise, and none in the VMO muscle. In a 2011 study, Kacin and Strazar, using a CW-NIRS system, compared oxygenation dynamics of the vastus lateralis (VL) before and after a BFR training program (135). They reported no acute differences in VL oxygenation with full arterial occlusion (230 mm Hg), but training resulted in larger increases in exercise-associated [THb] and [HbO₂] during non-BFR exercise. They did not report kinetics of oxygenation during recovery (135). We observed that knee extension with sub-systolic BFR (100 mm Hg) results in exposure of the VMO to substantially decreased stO₂ values (range: 7.5 to 11.2% lower) during recovery from each set. This reduction in stO₂ occurs in the context of greater [THb] indicating perhaps an increased capacity for post-exercise O₂ consumption. Part of this phenomenon

may be driven by increased downstream muscle O_2 demand in the period immediately following exercise. Analysis of exercise and recovery kinetics of $[HbO_2]$ and $[HbR]$ showed that while BFR slowed VMO $[HbO_2]$ hyperemia during recovery ($56 \mu M/min$ with BFR vs. $89 \mu M/min$ in Matched, $p = 0.004$), it did not inhibit the average increase in $[HbO_2]$. BFR exercise was, however, associated with a spike in $[HbR]$ before the onset of rapid clearance during recovery, contributing to the higher average $[HbR]$ (49% higher for BFR during rest 1). To come to these conclusions, we employed an empirical piecewise regression approach to identify transitions between VMO oxygenation phases. Typically, muscle $[HbR]$ kinetics are modeled with phasic mono-exponential regression(85,89,91). Recent work has shown, in the context of cycling ramp exercise, that piecewise linear fitting may be a valid approach (77). Qualitatively, the piecewise approach provides an advantage of greater descriptive utility and potentially useful comparisons between parameters such as phase duration and slope. While VMO $[HbR]$ and $[HbO_2]$ kinetics in knee extension have not been extensively characterized, our results would seem to indicate that the piecewise approach is valid. However, our study was limited by the acquisition time of the TR-NIRS instrument ($\sim 3s/measurement$) and therefore a loss of sensitivity to transient changes.

We also observed differences in measured PL between experimental conditions. The CV for PL at 796 nm was significantly higher in BFR vs. Matched, indicating greater variability over the course of exercise and recovery. There were also larger oscillations in μ_s' in BFR, although the CV difference was not statistically significant ($p = 0.09$). This observation is likely due to larger blood volume oscillations in BFR exercise, with a likely contribution of other molecular species (83) which accumulate to a higher degree in the BFR state. Also, the change in PL from baseline to final recovery (after release of BFR) was larger in BFR than in

Matched, perhaps indicating a persistent effect on VMO optical properties after BFR exercise. Both PL and μ_s' can affect reported $[\text{HbO}_2]$ and $[\text{HbR}]$ by the Beer-Lambert law. Another issue that must be considered is the effect of skin and subcutaneous adipose tissue (SAT) on measured optical properties. While all reflectance NIRS measurements include non-negligible contributions from the superficial layers, several factors mitigate this fact in this case: firstly, the overlying tissue above the VMO is relatively thin (3-6 mm, author's unpublished observations) compared to the source detector separation (30 mm). Secondly, the time-resolved approach discriminates between early and late-arriving photons, which allows for greater intrinsic sensitivity to absorption in deeper tissues. Finally, the level of $[\text{THb}]$ recorded in this study (baseline VMO $[\text{THb}] = 148.5 \pm 6.8 \mu\text{M}$) is consistent between subjects, indicating similar distribution of muscle in the sample volume. While the influence of superficial changes in blood flow and blood volume on reported kinetics cannot be discounted(136), others have shown these to be minimal in the case of brain TR-NIRS measurements (137). Furthermore, it has been shown that using spatially-resolved NIRS, another technique capable of compensating for changes in PL, reduces sensitivity to skin blood flow in muscle $[\text{THb}]$ measurements(92). Future studies may help quantify the effects of SAT thickness and skin blood flow on kinetics of VMO TR-NIRS signals, as has been done with other muscle groups (90).

Mechanisms of BFR effect

One hypothesis for the increased BFR-induced training adaptation and hypertrophy in muscle is the effect of metabolite accumulation in venous blood (123) and subsequent release of circulating factors (121,138). It is thought that reduced O₂ delivery is also likely to contribute to the BFR effect, as systemic hypoxia during resistance exercise has been shown to enhance hormonal responses (139). Given the persistently low muscle stO₂ during recovery with BFR, it is possible that hypoxic signaling may be stimulated in this condition. However, while we observed a decrease in [HbO₂] recovery slope, there is no evidence to suggest an O₂ delivery limitation during BFR because there was no overall reduction in [HbO₂] during exercise or rest. In fact, [HbO₂] is elevated during sets 2 and 3 of exercise in BFR over other conditions. It is possible that BFR, by slowing the egress of deoxygenated blood facilitated O₂ utilization, contributing to the observed [HbR] spike. Further studies are required to determine whether the lower stO₂ observed during recovery leads to hypoxic signaling or if it is simply a consequence of greater O₂ availability and extraction.

Additionally, it has been demonstrated that BFR training can enhance post-occlusive hyperemic blood flow in muscle (140), possibly as a result of increased angiogenesis. The persistent increase in blood volume caused by BFR, as evidenced by elevated [THb], may act to enhance the shear stimulus on the vessel wall, thereby promoting angiogenesis (135,141). The level of hypertrophy achieved with a given dosage of resistance exercise is also dependent on the duration of rest periods, with shorter intervals likely inducing larger gains

(142). It is possible that the spike in [HbR] we observe in BFR exercise acts in a way analogous to reduction in recovery time, i.e. by slowing metabolite clearance.

Prefrontal Cortex Oxygenation

We have also shown small but consistent increases in [HbR] and [HbO₂] in the PFC of subjects with and without BFR. In BFR and Fatigue conditions, when RPE is higher, this increase in PFC [HbR] is relatively larger, suggesting that PFC [HbR] may be related to activity-dependent fatigue (21,95). Additionally, during BFR, the increase in [HbO₂] during exercise is smaller than in the other conditions and therefore stO₂ does not increase. Our results correspond to published data indicating that knee extension is associated with increases in PFC stO₂ and blood volume ([THb]) (127). The observation that BFR abolished the PFC stO₂ increase during exercise suggests that it causes a different metabolic response for a given increase in [THb]. It has been observed (143) that lighter exercise with moderate occlusion is associated with perceptual responses akin to heavier-load, non-BFR exercise, possibly due to increased compression of peripheral nerves. In a 2003 study, it was shown that cycling exercise with occlusion could alter cerebral metabolism (144), possibly by altered sensory input from skeletal muscle. It is not clear whether small PFC stO₂ changes (< 5%) such as those we observed would impact perception of fatigue. It seems that at minimum, moderate exercise with BFR can affect O₂ utilization and blood flow in the PFC in a manner that correlates with increased RPE. In summary, the results of these studies indicate that muscle hemodynamics and oxygenation may play a role in the enhancement of resistance exercise outcomes by BFR and that BFR can modulate exercise-induced changes

in PFC hemodynamics in combination with perceived exertion during isokinetic resistance exercise.

CHAPTER 5: The use of diffuse optical spectroscopy to measure subcutaneous fat physiology during calorie restriction

RATIONALE

While the prevalence and severity of obesity and metabolic disorders are well-established, the causal links between obesity and its clinical sequelae are still incompletely understood. Recent physiological studies have revealed the potentially critical role of adipose tissue (AT) in the development of metabolic disorders (145,146). Both visceral and subcutaneous adipose tissue have been shown to be subject to various pathophysiological processes, such as inflammation (44,147), dysregulated oxygenation (41,43,148,149), and disrupted endocrine signaling (150,151). One of the central observations in this field in recent years has been the discovery of depots of “beige” adipocytes in humans. These cells have been shown to possess a unique gene expression profile and to preferentially upregulate O₂ consumption when compared with true “white” adipocytes (152). Various experimental models in mice have demonstrated that increased brown or beige adipocytes are protective against excess weight gain and insulin resistance (153). It has been shown that muscles subjected to exercise training produce a circulating factor, irisin, that acts upon white subcutaneous AT, inducing a processing of UCP-1

mediated (153) mitochondrial uncoupling and O₂ consumption, possibly improving metabolism generally (154).

There are a variety of environmental and molecular triggers for the process of AT browning (45), but changes in nutrition have also been shown to significantly alter AT phenotype. In mice, calorie restriction (CR), even of a relatively short duration of 3 months, can lead to nitric oxide (NO) mediated increases in white AT mitochondrial DNA, peroxisome proliferator-activated receptor- γ coactivator 1 α (PGC-1 α), and markers of mitochondrial biogenesis (155). The authors of this study also suggest that enhanced white AT SIRT1 expression may contribute to the widely observed life-extending effects of CR in mammals(155).

Studies of CR in humans have focused on morphological changes in AT, such as size and presence of inflammatory cells (156), as well as on changes in gene expression. Calorie restriction regardless of diet composition induces changes in the subcutaneous AT expression of genes involved in metabolic regulation (157). In addition to molecular changes in AT, there are also well-known morphological alterations that occur. It has been observed that reducing weight in humans leads to decreases in adipocyte size; in a recent study, a 10% weight loss was shown to result in a 16% decrease in adipocyte volume (158). It has also been suggested that these changes in cell volume might affect the kinetics of O₂ consumption by altering functional vascular density (42). The downstream metabolic implications of such changes are beginning to be understood. A recent investigation found that hypoxia-inducible factor (HIF)-1 alpha expression increased in animals provided a high-fat diet. HIF-1 alpha seems to act on the mitochondrion to uncouple respiration, leading to insulin resistance and inflammation (41). The authors suggest that increased O₂

consumption in AT by itself leads to detected hypoxia (149), and induction of HIF-1 alpha. Recent evidence from human studies emphasize the importance of adipocyte size in relation to metabolic disease. One study found a strong positive correlation between adipocyte size and the presence of type 2 Diabetes or its associated risk factors in candidates for bariatric surgery (39). A recent study revealed a correlation between adipocyte hypertrophy and both insulin resistance and AT inflammation (159). The process of AT browning also leads to morphological changes in adipocytes; specifically, brown and beige cells tend to have multilocular lipid droplets as opposed to the unilocular structure of white AT(153). Given the potential importance of the phenomena of AT browning, beige fat, and the relation between adipocyte size and metabolic disease, it is likely that methods for measuring AT physiology in humans will become increasingly needed in physiology and clinical medicine. Currently, magnetic resonance imaging (MRI) can be used to differentiate brown AT from white AT (160), but it is less clear that beige adipocytes can be distinguished in the same way. Additionally, there are to our knowledge no methods to non-invasively assess either adipocyte size or lipid droplet locularity.

Diffuse optical spectroscopic imaging (DOSI) may be uniquely suited to this purpose. DOSI is a near-infrared technique that quantitatively measures interactions of near-infrared light with tissues at depth. Specifically, by use of frequency-domain photon migration (FDPM), the reduced scattering coefficient (μ_s') and absorption coefficient (μ_a) of biological tissues can be accurately measured. Once absorption coefficients are calculated at several wavelengths with FDPM, broadband spectral reflectance and known molar extinction coefficients are used to calculate concentrations of the major absorbing chromophores in tissue (Oxyhemoglobin [HbO₂], deoxyhemoglobin [HbR], water, and bulk

lipid fractions) (65,66). Diffuse optical techniques are increasingly used in the study of cerebral(161) and muscular (90) hemodynamics and metabolism, as well as in cancer biology (69). To our knowledge, DOSI has not been explored as a method for measuring AT phenotype. However, other modalities such as PET and ^{133}Xe washout have been used to quantify blood flow in AT (162). While not capable of directly measuring flow, DOSI-measured concentrations of hemoglobin reflect changes in perfusion, metabolism, and total blood volume (99). Given these factors, we reasoned that DOSI could be used to track changes in abdominal subcutaneous AT that may occur with drastic changes in metabolism, and that such changes would reflect expected alterations in tissue structure and function. To this end, we chose to study a group of volunteers undergoing weight loss using by calorie restriction. There were two specific hypotheses: firstly, we hypothesized that weight loss by calorie restriction would be associated with increases in tissue scattering coefficients, reflective of a reduction in adipocyte size, as well as a potential increase in density subcellular components such as vesicles or mitochondria. Secondly, we hypothesized that weight loss would be associated with increased resting metabolism in subcutaneous AT. While DOSI cannot directly measure the metabolic rate of O_2 consumption in tissues, increases in individual DOSI-derived parameters such as [HbR], water fraction, and tissue optical index (TOI, the product of [HbR] and water, divided by lipid fraction) have been shown to correlate with increased metabolic rate (69). TOI has been used in DOSI studies of breast cancer to contrast metabolically active tumor tissue with relatively quiescent surrounding normal breast (69,71).

METHODS

Subjects and experimental design

Participants for this study were recruited from a medically-supervised weight management program conducted by UC-Irvine Healthcare. Potential participants were recruited and screened at information sessions or early program visits, and provided written informed consent, as well as written waiver to allow researchers access to medical records. Measurements took place at the Beckman Laser Institute (BLI) and Medical Clinic at UC-Irvine (Irvine, CA). Males and females 18-75 years old and participating in the weight loss program were included, and the exclusion criteria were a history of myocardial infarction and pregnancy or planned pregnancy. Measurement sessions occurred at three time points: T1 (before or within two weeks of starting weight loss), T2 (6-8 weeks after T1), and T3 (6 weeks after T2). At each measurement session, subjects were assessed for weight, blood pressure, abdominal circumference, diet and physical activity. Subjects were placed in a supine position and a skin marker was used to draw a rectangular grid of 30 points centered about the umbilicus. The grid consisted of 3 horizontal rows separated by 4 cm, and 10 columns separated by 3 cm (Figure 5.1A). Before DOSI measurements were initiated, subjects were resting in a supine position for a minimum of ten minutes. At each point on the grid, 3 DOSI measurements were obtained and averaged for analysis. Grid points were named by row (U for upper, M for middle, L for lower), and column (1-10). Additionally, ultrasound imaging (HDI-5000, Phillips Healthcare, MA, USA) was used to

assess the thickness of subcutaneous fat layer in the middle row of the grid. A total of 11 subjects participated in this study, of which 1 was subsequently excluded due to termination of weight loss during the course of measurement visits, resulting in an n = 10 (5 M, 5 F).

Weight Loss

Weight loss was achieved through medically supervised calorie restriction by meal replacement (HMR 70 program, MA, USA), with the level of meal replacement determined by starting weight, individual weight goal, and medical screening. Two levels of calorie restriction were administered in this group of subjects (Table 5.1). The more restrictive plan (type 1) involved intake of between 500-800 kcal/day, while the more flexible plan (type 2) allowed for up to 1200 kcal/day. Physical activity during the program was not controlled, but regular low to moderate exertion was encouraged. The rates of weight loss experienced therefore varied between subjects, as did the initial degree of overweight. T2 and T3 measurement sessions occurred at the same time of day as the T1 visit, and subjects were instructed to keep their routine before the measurements consistent in terms of diet and exercise.

Ultrasound Measurements

Ultrasound images were taken and saved at each of the 10 middle row grid points using an HDI-5000 imaging unit (Phillips). Subsequently, subcutaneous tissue thickness

was measured and recorded using the embedded distance function of the device. Tissue thickness was defined as the distance from the surface of the skin to the most superficial visible muscle layer. Thickness values were recorded and analyzed for the middle row of DOSI grid positions at all three measurement sessions.

DOSI Measurements

DOSI measurements were performed with a system capable of combined frequency-domain photon migration (FDPM) and broadband NIR spectroscopy (NIRS) that measures subsurface optical and physiological properties in centimeter-thick tissues. The full technical details of the system are described elsewhere (17, 33). Briefly, our FDPM approach uses high-frequency, broadband modulated light sources (50 – 500 MHz) of four wavelengths (660, 690, 780, and 830 nm), while NIRS makes use of a parallel lamp and spectrophotometer system to provide 650-1000 nm broadband reflectance data. FDPM and NIRS signals are combined using a model-based approach to obtain quantitative NIR absorption and scattering spectra (650-1000 nm) from tissue.

Detector and source fibers in a single black, delrin plastic housing were placed on the surface of the skin at a source-detector separation of 22 mm. At each measurement point, reflected signals were collected and stored, with subsequent analysis done using custom software (21) in MATLAB (Mathworks, MA, USA). The FDPM system detects phase and amplitude of reflected light at each of the four discrete wavelengths, and fits this information to the diffusion equation(66) to obtain tissue absorption (μ_a) and reduced scattering (μ_s') coefficients. Also necessary in this process is calibration of FDPM

reflectance signals against a solid tissue-simulating phantom with known μ_a and μ_s' . In this study, a single silicone-based calibration phantom was used for all studies and subsequent data processing. Broadband NIRS reflectance is calibrated using simple reflectance profile of a white surface with known reflectivity. Then, the broadband diffuse reflectance signal was fit to the measured FDPM optical properties to obtain μ_a and μ_s' at all wavelengths from 650-1000 nm. Finally, using a least-squares method and known molar extinction coefficients, concentrations of oxyhemoglobin ($[HbO_2]$), deoxyhemoglobin ($[HbR]$), total hemoglobin ($[THb]$), and fractions of water and lipid were calculated. From these quantities, the oxygen saturation (stO_2) and tissue optical index (TOI) were also calculated. The stO_2 is the ratio of $[HbO_2]/[THb]$. TOI is defined as equation 1 below where water and lipid are expressed as tissue fractions, and it has been used in DOSI studies as an index of metabolic activity (69).

$$TOI = \frac{[HbR] \times H_2O}{Lipid}$$

At each measurement site on the abdomen, three measurements were obtained and chromophore values were averaged for analysis. Both raw μ_a and μ_s' spectra were also obtained and used for analysis and visualization.

Data Analysis

Statistical analysis was performed using R (R Core Team (2014)). R: A language and environment for statistical computing. R Foundation for Statistical Computing, Vienna,

Austria. URL <http://www.R-project.org/>), primarily the lme4 package (version 1.1-7, URL: <http://CRAN.R-project.org/package=lme4>) for computation of linear mixed-effects models(163,164). Subject weight, abdominal circumference, and blood pressure were analyzed using models with fixed effects for time point and gender. The effect of individual subjects was included as a random effect with random slopes with regard to time point, to account for the repeated measures design. Ultrasound-derived thickness measurements and DOSI data were analyzed using models with the same random effects structure, but with an additional fixed effect of abdominal position. To determine whether the addition of time point as a fixed effect improved model quality significantly, these models were tested against corresponding null models without time point by the likelihood ratio test. A significant interaction terms between time point and position were included if they produced an improved fit by the likelihood ratio test. If a significant main effect was determined from the model on a given variable, sample means at each time point were calculated and compared using Tukey's method. Two individual DOSI measurement points were removed from the analysis a priori due to unphysical values of absorption and scattering, likely a result of improper probe contact. Additionally, 11 measurement points from one time point in one subject were missing due to instrument malfunction. Plots of time point means with standard error were generated in Prism (Version 6, Graphpad, La Jolla, CA) with p-values obtained from aforementioned multiple comparisons. Pearson Product-Moment Correlation analysis was also done in Prism, with the mean change in each optical parameter tested for correlation against the percentage of starting weight lost in each subject.

Image Generation

After initial processing, DOSI data from each set of 30 measurements was plotted using grid coordinates and heat map functions in MATLAB. Heat maps were created with a fixed scale over all subjects. Linear interpolation was used to account for sparse spacing of grid points. The colored maps were then overlaid on a 3D textured mesh of a one representative abdomen with grid points drawn on it. The initial 3D image was obtained by using Kinect for windows and accompanying software development kit (Microsoft, WA, USA). Colored heat maps obtained from MATLAB were warped and overlaid on the textured mesh using Photoshop CS6 Extended (Adobe, CA, USA) to create the final images.

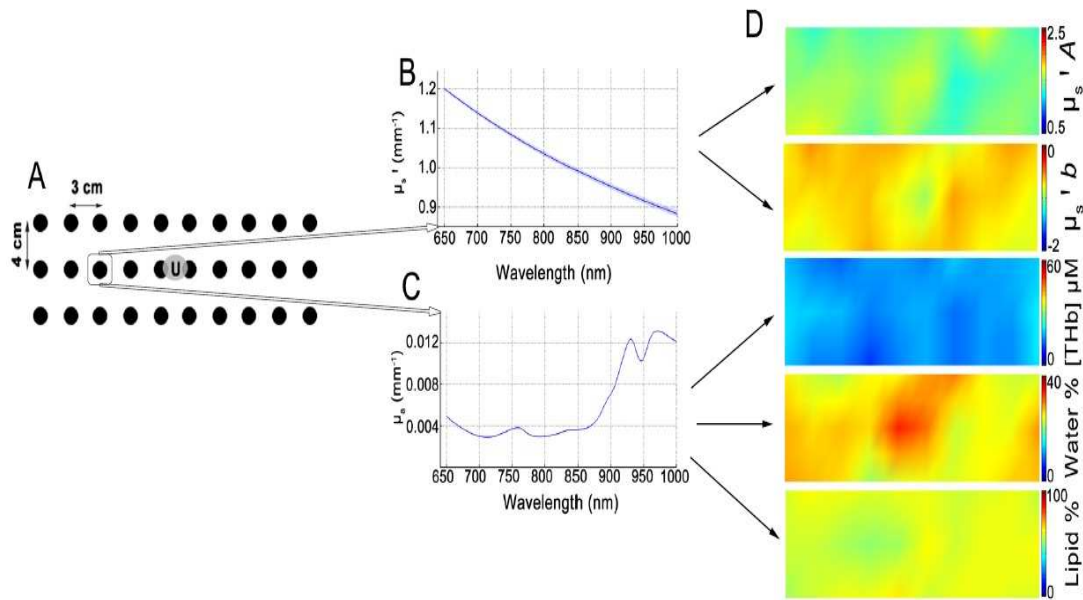


Figure 5.1: Measurement schematic: Schematic of DOSI measurement procedure. (A) demonstrates the grid used with distances between points indicated. The “U” in the center of the grid refers to the subject’s umbilicus. (B) shows a typical scattering spectrum obtained from one subject at point M3, with the mean of three replicate measurements \pm SD shown as a line and a shaded area respectively. (C) shows the mean absorption spectrum at the same location in the same subject, also as mean \pm SD (D) demonstrates example heat maps of scattering and absorption parameters from one subject over all 30 measurement points with linear interpolation.

RESULTS

Subject characteristics

Anthropometric data and weight loss effects are shown in Table 5.1, with p-values of comparisons with regard to time point shown. Calorie restriction was associated with significant changes in weight ($\chi^2 = 35.15$, $p < 0.001$), and weight also demonstrated a significant interaction between time point and gender ($\chi^2 = 7.2068$, $p = 0.027$). CR also had a significant effect on abdominal circumference ($\chi^2 = 31.47$, $p < 0.001$). There were also significant effects of CR on both systolic ($\chi^2 = 13.241$, $p < 0.01$), and diastolic blood pressure ($\chi^2 = 10.688$, $p < 0.01$), with significant reductions in both at T2 and T3. Mean weight loss was larger between T1 and T2 (mean \pm SE: -7.9 ± 1.3 kg, $p < 0.001$) than between T2 and T3 (-4.4 ± 1.3 kg, $p < .01$). Ultrasound measurements of subcutaneous tissue thickness were significantly affected by time point ($\chi^2 = 14.599$, $p < 0.001$), with no significant interaction with position. Mean tissue thickness at T1 was 3.4 cm, and changed to 3.1 cm at T2 (adj. $p < 0.001$). There was a further decline to 2.8 cm at T3 (adj. $p < 0.001$). In terms of position, the subcutaneous fat layer was consistently thicker at positions closer to the midline. Supplemental figure 1 shows data means and ranges of thicknesses obtained from ultrasound measurements at all points for all subjects. From T1 to T3, the mean reduction in weight was 11.7 ± 1.1 % (SE) of starting weight.

Table 5.1: Anthropometric Data Anthropometric data and weight loss outcomes for 10 subjects

Subject	Gender	Age	Diet	T1 BMI	Weight (kg)			Abd. Circumference (cm)			Systolic BP (mm Hg)			Diastolic BP (mm Hg)		
					T1	T2	T3	T1	T2	T3	T1	T2	T3	T1	T2	T3
1	M	73	1	42.7	151.0	139.9	127.5	137	130	125	127	113	107	78	71	73
2	M	49	1	36.7	129.8	124.4	117.5	121	113	113	126	122	126	78	79	82
3	M	58	1	33.7	109.5	98.9	97.3	106	106	100	122	115	107	83	73	70
4	F	58	2	30.3	75.1	68.9	64.3	99	90	80	131	126	124	89	78	80
5	F	45	1	40.0	115.9	108.4	104.3	127	119	117	127	122	130	89	85	80
6	F	60	1	29.9	86.6	79.2	76.2	100	98	95	114	107	116	69	71	76
7	F	58	2	25.2	64.4	63.0	61.2	88	86	83	120	102	111	75	66	72
8	M	41	2	31.6	88.9	81.0	79.1	99	93	93	139	135	127	92	94	87
9	M	58	1	31.2	110.4	95.5	91.9	107	99	93	138	115	121	91	83	76
10	F	60	1	32.4	86.8	80.7	76.8	108	103	98	139	138	128	92	76	72
mean		56		33.4	101.8	94.0	89.6	109	104	100	128	120	120	84	78	77
SD		9		5	26	25	22	15	14	14	9	11	9	8	8	5
SEM		2.8		2	8	8	7	5	4	5	3	4	3	3	3	2
<i>p</i>					T2-T1	T3-T1	T3-T2	T2-T1	T3-T1	T3-T2	T2-T1	T3-T1	T3-T2	T2-T1	T3-T1	T3-T2
					<0.001	<0.001	0.002	<0.001	<0.001	<0.001	<0.001	<0.001	0.996	0.002	0.007	0.914

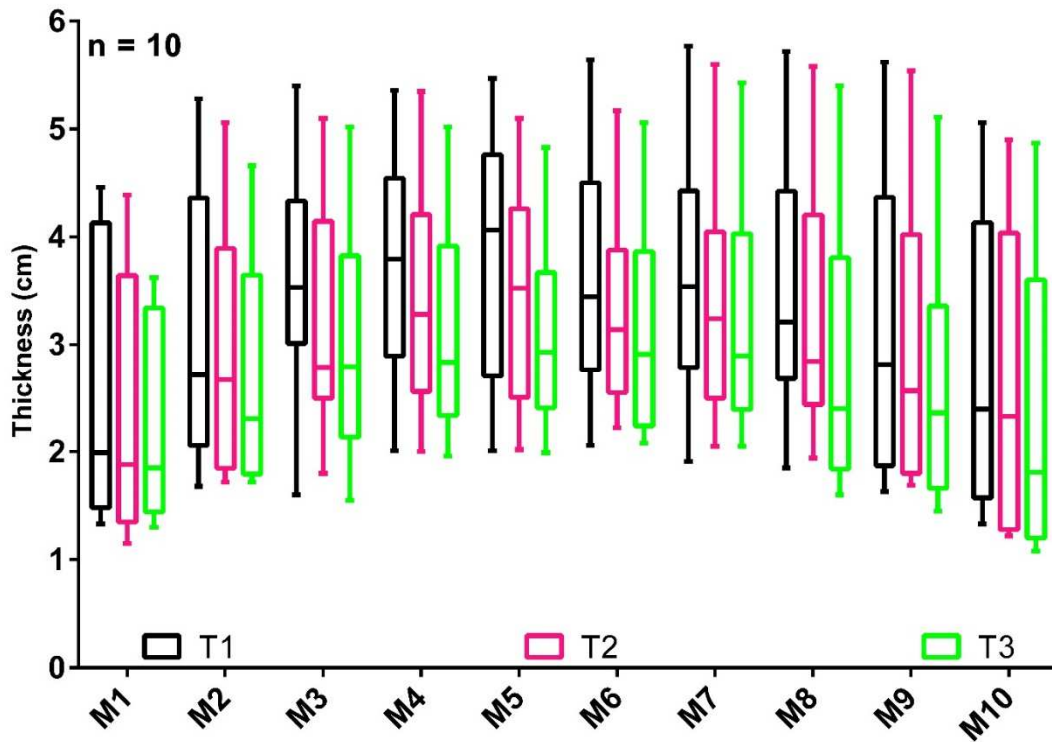


Figure 5.2: Tissue thickness results: Ultrasound thickness measurements for all 10 subjects and 10 middle row abdominal sites measured. Data are displayed in terms of mean, quartiles, and ranges for all three time points. T2 is magenta and T3 is green.

DOSI measurements

A schematic of the process used for DOSI measurements and analysis is shown in figure 2. A total of 30 sites on the abdomen were measured for each subject at each visit, centered about the umbilicus (figure 5.1A). Using optical scattering (figure 5.1B) and absorption (figure 5.1C) spectra at each measurement point, heat maps were created to visualize variation in DOSI parameters with respect to the surface of the abdomen, and weight loss (figures 5.1D). At each measurement point, two parameters related to optical scattering were obtained by measuring reduced scattering coefficient at all four wavelengths, according to equation 2:

$$\mu'_s = A \left(\frac{\lambda}{500 \text{ nm}} \right)^b \quad (67)$$

Here, b is the “slope” parameter which describes the dependence of scattering on wavelength, while A is the factor which describes the amplitude of NIR scattering. The λ term refers to the wavelength at which μ'_s is measured, and the 500 nm in the denominator is a reference wavelength used to normalize the value within parentheses. In figure 5.4A, average scattering spectra in a single subject at all three time points are shown. Here, there is both an upward shift in the spectrum with weight loss, as well as a steepening of the curve with respect to wavelength. These observations would therefore constitute an increase in A and a decrease in b , according to equation 2. The A and b parameters at all

measured abdominal sites were averaged for each time point along with absorber concentrations as described previously, and analyzed. For one subject (#9), the DOSI data obtained from M10 and the lowest row at T1 were lost due to an instrument malfunction, therefore data from this subject at T1 reflects a spatial mean of 19 measurements.

Table 5.2: All optical data: Mean \pm SEM for each subject for each of the nine DOSI outcome variables. Means are calculated over data from all available spatial points.

Subject	A			b			Water fraction		
	T1	T2	T3	T1	T2	T3	T1	T2	T3
1	1.33 \pm 0.02	1.49 \pm 0.02	1.50 \pm 0.02	-0.67 \pm 0.01	-0.71 \pm 0.02	-0.91 \pm 0.02	23.6 \pm 0.6	25.7 \pm 0.5	31.5 \pm 0.6
2	1.46 \pm 0.01	1.74 \pm 0.03	1.88 \pm 0.03	-0.73 \pm 0.01	-1.02 \pm 0.01	-1.06 \pm 0.02	23.0 \pm 0.5	28.5 \pm 0.6	33.8 \pm 0.6
3	1.40 \pm 0.01	1.38 \pm 0.02	1.44 \pm 0.02	-0.73 \pm 0.01	-0.82 \pm 0.01	-0.79 \pm 0.01	20.2 \pm 0.3	23.0 \pm 0.3	26.8 \pm 0.4
4	1.22 \pm 0.03	1.46 \pm 0.03	1.57 \pm 0.06	-0.50 \pm 0.02	-0.73 \pm 0.02	-0.85 \pm 0.03	14.6 \pm 0.5	20.7 \pm 0.7	27.3 \pm 0.8
5	1.29 \pm 0.03	1.47 \pm 0.04	1.51 \pm 0.04	-0.72 \pm 0.02	-0.82 \pm 0.02	-0.91 \pm 0.03	22.4 \pm 0.6	24.0 \pm 0.8	27.8 \pm 0.7
6	1.07 \pm 0.01	1.28 \pm 0.03	1.34 \pm 0.03	-0.65 \pm 0.01	-0.82 \pm 0.03	-0.79 \pm 0.03	14.5 \pm 0.4	16.8 \pm 0.5	19.4 \pm 0.8
7	1.14 \pm 0.03	1.18 \pm 0.03	1.26 \pm 0.03	-0.64 \pm 0.02	-0.71 \pm 0.02	-0.67 \pm 0.02	21.9 \pm 0.7	24.0 \pm 0.9	23.6 \pm 1.1
8	1.55 \pm 0.05	1.63 \pm 0.06	1.84 \pm 0.07	-0.98 \pm 0.03	-1.02 \pm 0.03	-1.12 \pm 0.03	23.1 \pm 0.6	25.3 \pm 0.6	29.3 \pm 0.8
9	1.85 \pm 0.06	2.20 \pm 0.06	2.11 \pm 0.06	-1.28 \pm 0.05	-1.49 \pm 0.03	-1.52 \pm 0.03	30.4 \pm 0.9	40.9 \pm 0.5	42.7 \pm 0.5
10	1.35 \pm 0.03	1.28 \pm 0.02	1.50 \pm 0.03	-1.00 \pm 0.02	-0.91 \pm 0.02	-0.99 \pm 0.02	24.7 \pm 0.6	23.1 \pm 0.5	28.3 \pm 0.6
	Lipid fraction			HbO₂			HbR		
	T1	T2	T3	T1	T2	T3	T1	T2	T3
1	59.9 \pm 0.6	58.4 \pm 0.5	59.3 \pm 0.9	11.3 \pm 0.7	10.3 \pm 0.4	11.3 \pm 0.5	6.2 \pm 0.2	6.2 \pm 0.1	7.0 \pm 0.2
2	61.5 \pm 0.7	63.2 \pm 1.3	63.4 \pm 0.9	7.3 \pm 0.5	9.0 \pm 0.5	12.2 \pm 0.6	5.4 \pm 0.1	5.3 \pm 0.1	6.3 \pm 0.1
3	64.3 \pm 0.4	64.8 \pm 0.6	63.5 \pm 1.1	10.1 \pm 0.4	8.5 \pm 0.3	9.3 \pm 0.4	4.8 \pm 0.1	5.7 \pm 0.1	7.1 \pm 0.2
4	64.1 \pm 0.6	67.8 \pm 1.1	65.6 \pm 1.0	4.7 \pm 0.3	6.9 \pm 0.5	9.9 \pm 0.5	4.5 \pm 0.1	5.0 \pm 0.2	6.8 \pm 0.3
5	63.3 \pm 0.7	60.9 \pm 0.6	64.8 \pm 0.9	7.9 \pm 0.6	8.8 \pm 0.6	13.6 \pm 0.9	4.5 \pm 0.1	5.4 \pm 0.2	5.1 \pm 0.1
6	70.2 \pm 0.7	76.0 \pm 0.9	72.2 \pm 0.6	8.2 \pm 0.5	7.8 \pm 0.4	8.9 \pm 0.6	4.9 \pm 0.1	5.2 \pm 0.1	4.8 \pm 0.2
7	65.6 \pm 0.7	69.2 \pm 0.9	62.5 \pm 0.9	8.7 \pm 0.4	10.5 \pm 0.8	10.9 \pm 0.8	6.9 \pm 0.3	8.1 \pm 0.5	8.1 \pm 0.6
8	64.1 \pm 0.7	60.1 \pm 0.8	59.8 \pm 0.9	9.3 \pm 0.5	10.1 \pm 0.4	9.9 \pm 0.7	5.8 \pm 0.1	6.1 \pm 0.2	7.1 \pm 0.2
9	62.2 \pm 1.6	51.9 \pm 1.2	46.5 \pm 0.9	10.8 \pm 0.9	13.8 \pm 0.6	9.8 \pm 0.7	6.5 \pm 0.1	7.6 \pm 0.2	8.1 \pm 0.1
10	68.1 \pm 1.4	60.9 \pm 1.3	62.9 \pm 1.5	12.1 \pm 0.5	9.8 \pm 0.6	14.8 \pm 0.6	6.7 \pm 0.1	7.1 \pm 0.2	6.9 \pm 0.1
	THb			stO₂			TOI		
	T1	T2	T3	T1	T2	T3	T1	T2	T3
1	17.5 \pm 0.7	16.5 \pm 0.5	18.4 \pm 0.7	64.1 \pm 1.3	62.2 \pm 0.7	61.2 \pm 0.9	2.46 \pm 0.15	2.75 \pm 0.11	3.85 \pm 0.25
2	12.8 \pm 0.6	14.3 \pm 0.6	18.4 \pm 0.7	55.8 \pm 1.2	61.5 \pm 1.0	65.2 \pm 0.8	2.06 \pm 0.10	2.46 \pm 0.11	3.37 \pm 0.12
3	14.9 \pm 0.5	14.2 \pm 0.3	16.5 \pm 0.5	67.0 \pm 0.8	59.2 \pm 0.7	56.3 \pm 0.8	1.52 \pm 0.05	2.05 \pm 0.07	3.14 \pm 0.27
4	9.2 \pm 0.5	11.9 \pm 0.7	16.7 \pm 0.7	49.3 \pm 1.3	56.6 \pm 0.9	58.6 \pm 1.2	1.04 \pm 0.06	1.57 \pm 0.11	2.91 \pm 0.19
5	12.4 \pm 0.7	14.2 \pm 0.8	18.7 \pm 1.0	62.2 \pm 1.0	60.9 \pm 0.9	71.8 \pm 0.9	1.63 \pm 0.10	2.22 \pm 0.18	2.22 \pm 0.12
6	13.1 \pm 0.6	13.0 \pm 0.5	13.8 \pm 0.7	61.4 \pm 0.9	58.5 \pm 1.0	63.8 \pm 0.8	1.02 \pm 0.05	1.17 \pm 0.05	1.35 \pm 0.11
7	15.6 \pm 0.6	18.6 \pm 1.2	19.0 \pm 1.4	55.1 \pm 1.0	55.9 \pm 0.9	57.2 \pm 0.8	2.40 \pm 0.19	3.00 \pm 0.35	3.42 \pm 0.53
8	15.0 \pm 0.6	16.3 \pm 0.5	17.0 \pm 0.8	60.3 \pm 1.3	61.7 \pm 0.9	56.4 \pm 1.4	2.11 \pm 0.10	2.61 \pm 0.13	3.63 \pm 0.28
9	17.3 \pm 0.9	21.4 \pm 0.7	17.9 \pm 0.7	60.9 \pm 1.9	63.6 \pm 0.9	52.9 \pm 1.6	3.29 \pm 0.28	6.25 \pm 0.36	7.54 \pm 0.23
10	18.8 \pm 0.5	17.0 \pm 0.7	21.7 \pm 0.7	63.8 \pm 0.9	56.7 \pm 1.2	67.7 \pm 0.7	2.55 \pm 0.20	2.76 \pm 0.11	3.18 \pm 0.14

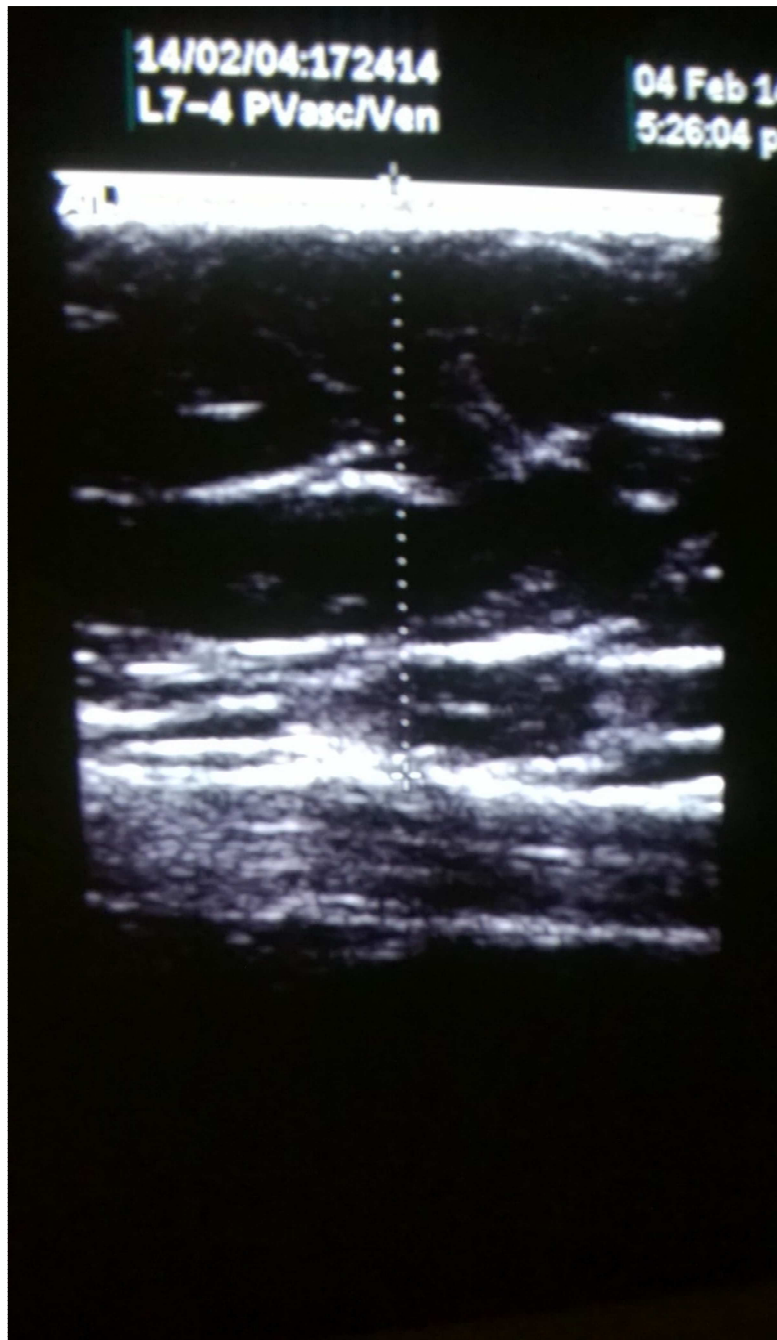


Figure 5.3: Sample ultrasound image: Example ultrasound image from weight loss subject. Subcutaneous tissue thickness was defined as distance from tissue surface to first visible striations indicating muscle layer.

NIR Scattering Changes

Linear mixed effects models (LME) revealed significant effects of weight loss on both scattering amplitude (A , $\chi^2 = 18.726$, $p < 0.001$) and slope (b , $\chi^2 = 11.761$, $p = 0.003$). Figures 5.5A and 5.5B show mean, standard error, and individual data points for each subject. A increased significantly at both T2 (T2-T1 = 0.15 ± 0.04 , adj. $p = 0.002$) and T3 (T3 - T2 = 0.08 ± 0.03 , adj. $p = 0.006$, T3-T1 = 0.23 ± 0.03 , adj. $p < 0.001$). The b parameter was significantly more negative at T2 and T3 than at T1 (T2 - T1 = -0.12 ± 0.03 , adj. $p = 0.001$, T3 - T2 = -0.06 ± 0.02 , adj. $p = 0.037$, T3 - T1 = -0.17 ± 0.04 , adj. $p < 0.001$). The changes in both b and A were larger between T1 and T2 than between T2 and T3. There was also a significant effect of gender on the A parameter, with a higher value observed in males than females (0.28 ± 0.08 higher, $p = 0.006$).

From T1 to T3, the mean increase in A over 28 measurement points ranged from 2.9% to 28.7%, with a mean and standard deviation of 17.0 ± 8.4 %. The mean b parameter change (reflecting a steeper slope) ranged from a 1.0% increase to 68.5% reduction, with a mean of 24.4 ± 20.9 %.

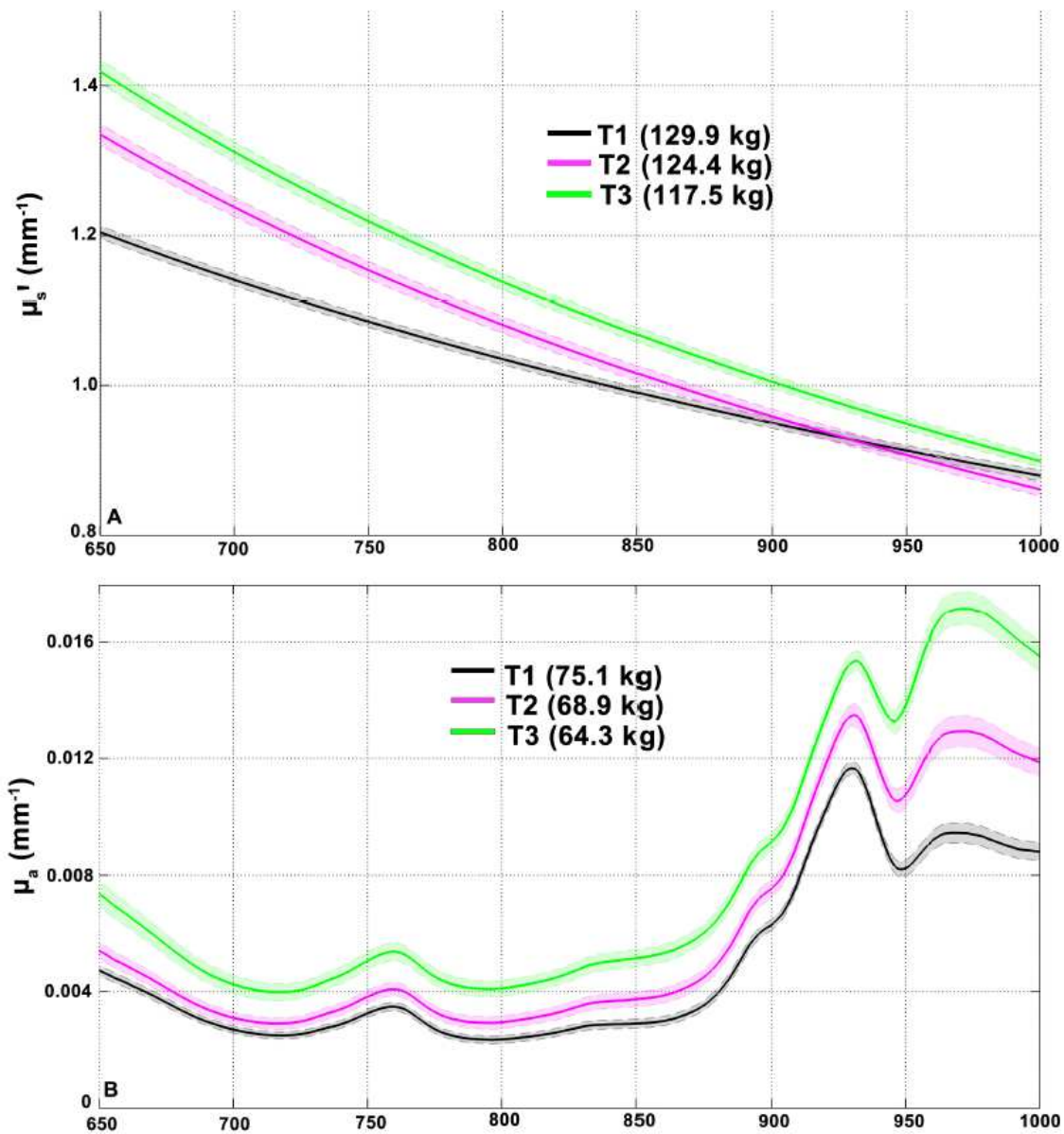


Figure 5.4: Scattering and absorption spectra: Full scattering (A) and absorption (B) spectra (mean \pm SEM of all spatial locations) for two subjects, with corresponding weights also displayed at each time point.

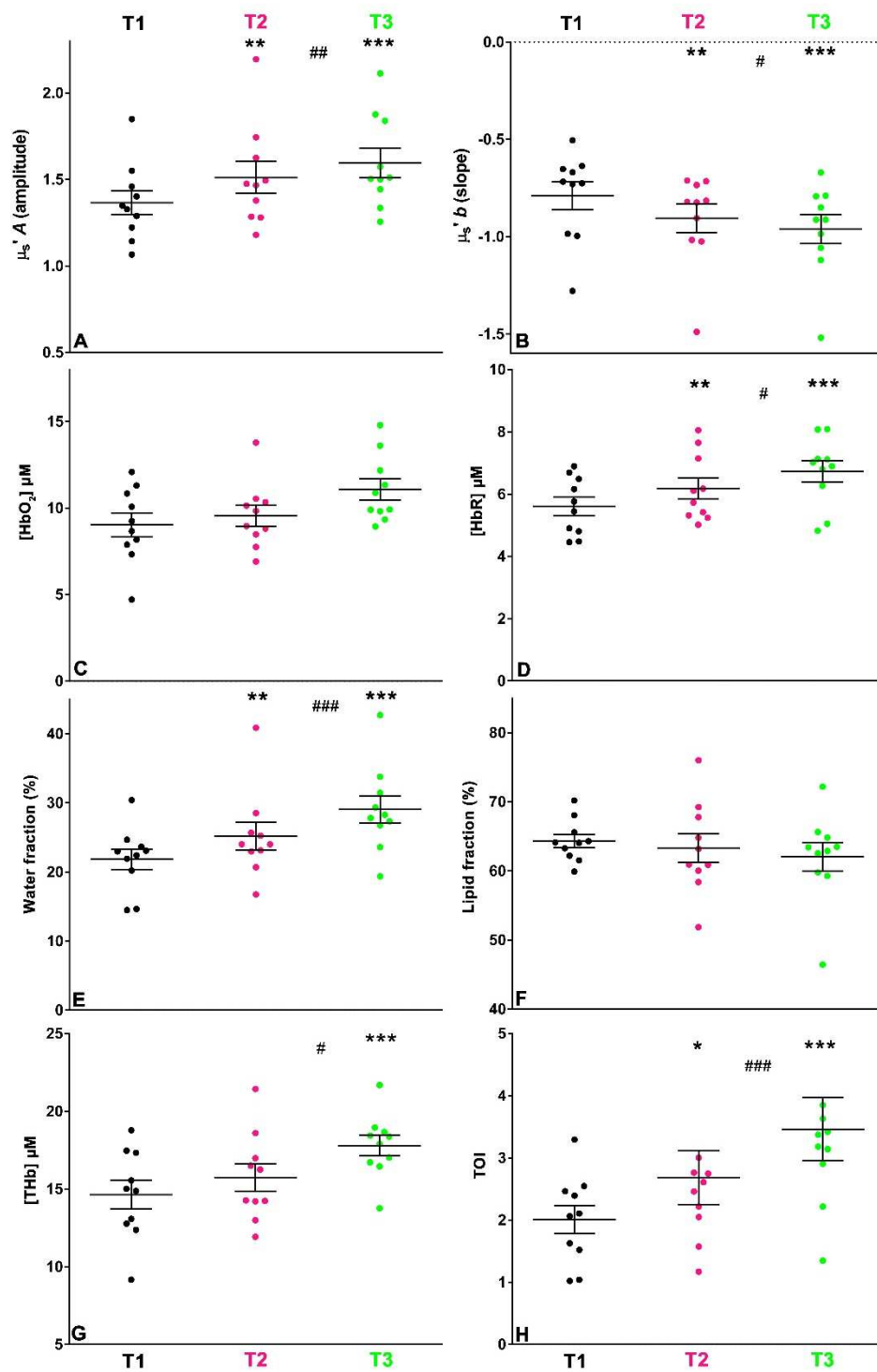


Figure 5.5: Mean differences: Mean \pm SEM of each chromophore value with individual data points shown. Each data point represents spatial mean for each subject. * indicates a significant difference from T1 level, whereas # indicates difference between T2 and T3. *** = $p < 0.001$, ** = $p < 0.01$, * = $p < 0.05$.

Absorption changes

Inspection of absorption spectra measured in individual subjects revealed progressive upward shifts in the 950-1000 nm range where water is the primary absorber with weight loss (as shown in one representative subject, Fig. 5.4B). LME models demonstrated significant effects of time point on water fraction ($\chi^2 = 18.646$, $p < 0.001$), [HbR] ($\chi^2 = 13.228$, $p = 0.001$), [THb] ($\chi^2 = 10.258$, $p = 0.006$) and TOI ($\chi^2 = 13.689$, $p = 0.001$), but not [HbO₂], stO₂ or lipid fraction. The mean [HbR] increased with time on the diet at both time points (figure 5.5E, T2 - T1 = 0.6 ± 0.1 μM , adj. $p < 0.001$, T3 - T2 = 0.5 ± 0.2 μM , adj. $p = 0.050$). [THb] was higher at T3 than at both T2 and T1 (figure 5.5G, T3 - T1 = 3.2 ± 0.8 μM , adj. $p < 0.001$, T3 - T2 = 2.1 ± 0.8 μM , adj. $p = 0.024$). The mean tissue water fraction increased from T1 to T2 (figure 5.5C, T2 - T1 = $3.4 \pm 1.0\%$, adj. $p = 0.003$), and from T2 to T3 (T3 - T2 = $3.9 \pm 0.6\%$, adj. $p < 0.001$). TOI increased progressively at both time points (figure 5.5H, T2 - T1 = 0.68 ± 0.25 , adj. $p = 0.019$, T3 - T1 = 1.45 ± 0.34 , adj. $p < 0.001$, T3 - T2 = 0.78 ± 0.14 , adj. $p < 0.001$).

Correlations between optical measures and weight loss

A significant Pearson correlation was found between the relative magnitude of weight loss and the increase in tissue water content in individual subjects between T1 and T3 (Figure 5.6A, $r = 0.679$, $p = 0.031$). There was also a moderate correlation with the absolute increase in TOI (Figure 5.6B, $r = 0.580$, $p = 0.079$).

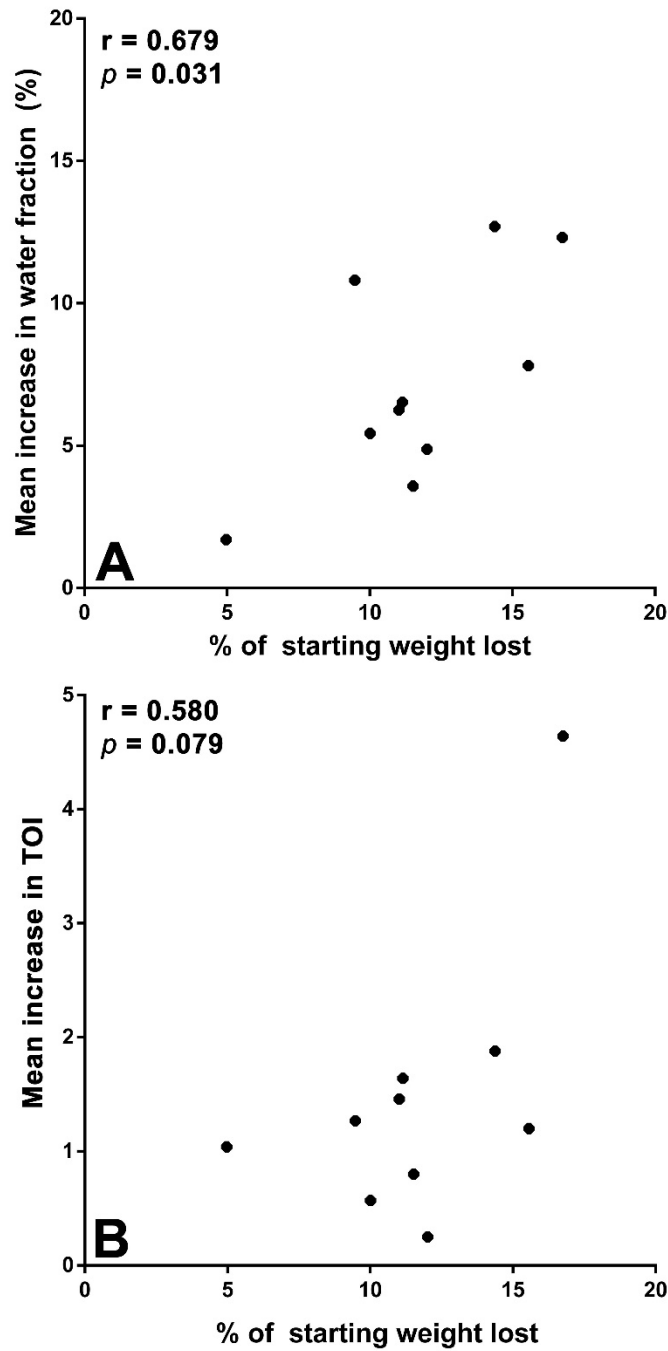


Figure 5.6: Weight loss correlations: Pearson-Product Moment correlations between mean absolute increase in water (A) from T1 to T3 and TOI (B) with percentage of starting weight loss in individual subjects.

DOSI patient topography images

Figures 5.7 and 5.8 shows sequential images of two parameters (scattering amplitude, A , and TOI) in two subjects: one male (5.7) and one female (5.8), with time points and corresponding weights shown to the left. In addition to significant effects with time on calorie restriction described above, LME models demonstrated significant effects of abdominal position on all optical outcomes analyzed. For the A parameter, there was a significant interaction between weight loss and abdominal position ($p < 0.001$). Qualitative analysis of images from these two subjects demonstrates a gradient in A , with higher baseline values measured in proximity to the abdominal midline, corresponding to areas of thicker subcutaneous AT. Although measurement locations in the upper row tend to exhibit higher values of A , increases in A are observed over the entire measurement area, and LME analysis uncovered no significant interactions between time point and abdominal position. With regard to TOI, baseline values are generally low, with a trend toward higher values and larger increases at lateral measurement locations, corresponding to areas with more superficial abdominal wall musculature.

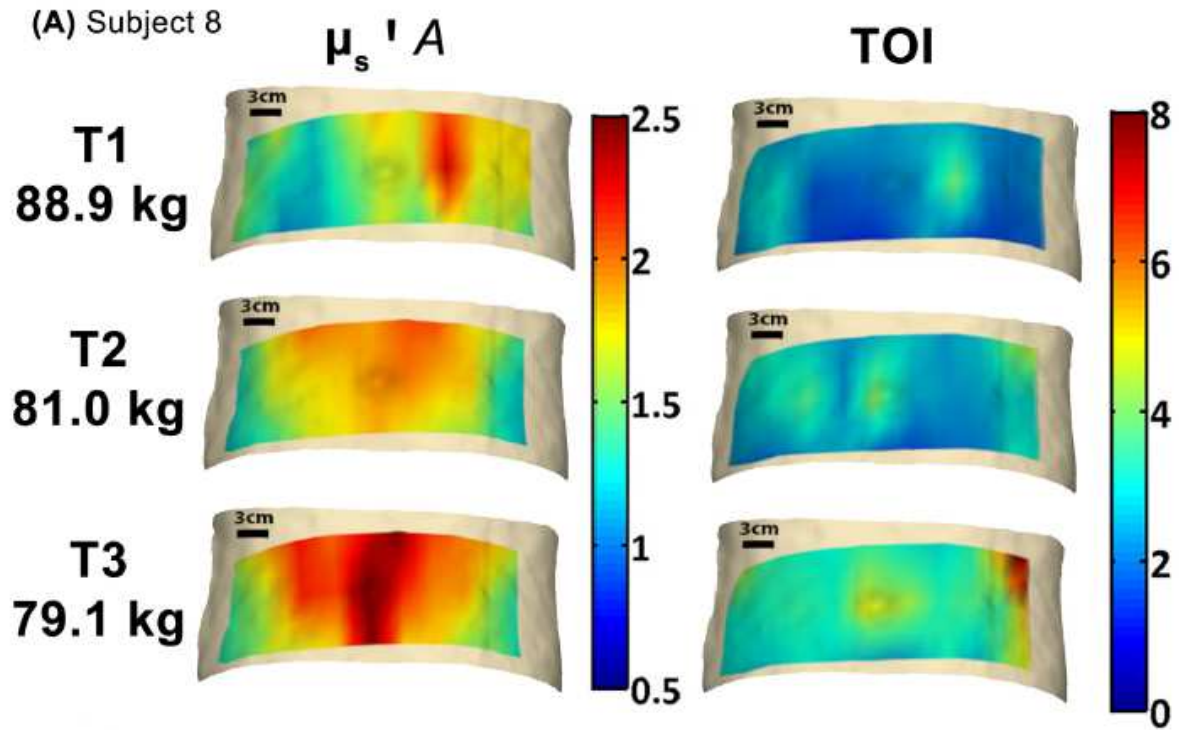


Figure 5.7: DOSI Maps subject 8: Sample sequential images of subject 8 for amplitude (left) and TOI (right). Heat maps are overlaid on representative abdominal surface. Calorie restriction was associated with a diffuse increase in both scattering amplitude and TOI, as well as other parameters described above.

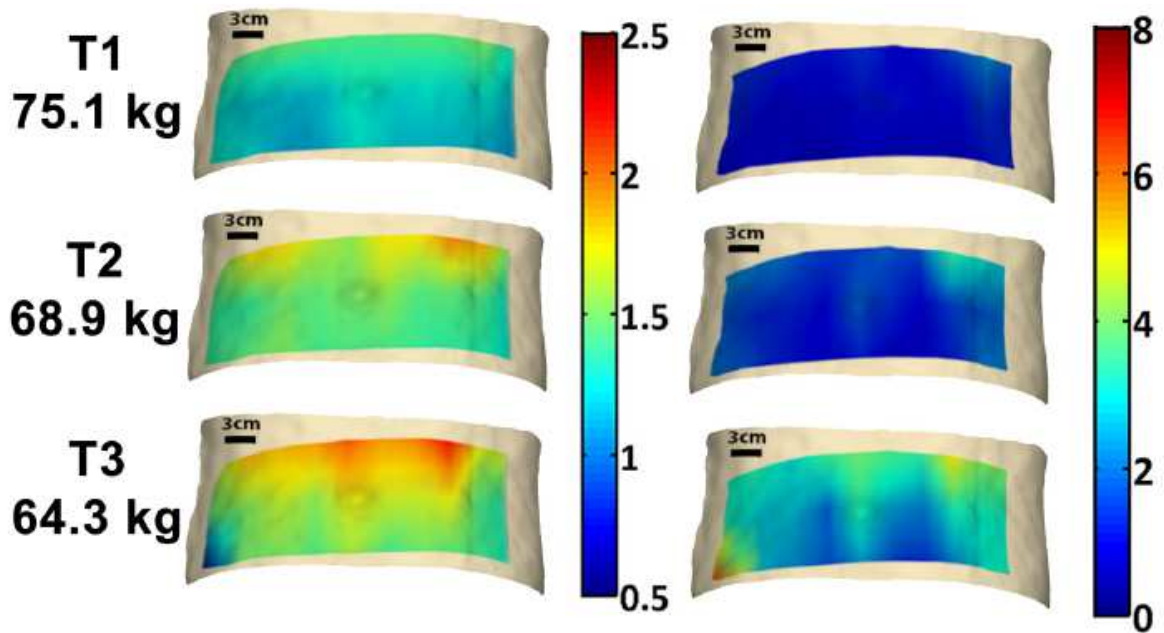


Figure 5.8: DOSI maps subject 4: Same as above, but for a second (female) subject.

DISCUSSION

Recent advances have demonstrated the numerous ways in which white AT can respond to and affect overall physiology and metabolism(165). It is becoming increasingly clear that changes in AT structure and function are involved in fundamental pathologic processes such as the development of insulin resistance (39,165). Therefore, it is a reasonable expectation that measurement modalities that are sensitive to AT characteristics may play a role in the evaluation and management of metabolic disease and its risk factors. DOSI, because of its ability to measure properties related to both structure and metabolism in vivo, is uniquely suited to this purpose. In this study, we have applied DOSI to measure changes in the optical properties of subcutaneous AT during weight loss by calorie restriction which are likely reflective of underlying changes in structure and function.

AT structure and optical scattering

It has long been recognized that adipocyte size is a dynamic parameter that is positively associated with degree of obesity, as well as fasting insulin levels(37). A recent study of twins non-concordant for obesity showed that increased weight is correlated with larger adipocytes, with or without AT hyperplasia (38). Interestingly, another recent study found that there is a threshold size that predicts the presence of diabetes or its risk factors in female candidates for bariatric surgery (39). The response of adipocytes to weight loss

interventions has also been well established experimentally. Studies have shown that individuals subjected to 12 weeks of a very low calorie diet (< 3400 kJ/day) demonstrate reductions in subcutaneous AT cell sizes on the order of 15-20% (156). Over this time scale, it is unlikely that a change in subcutaneous AT cell number would be observed (156), although AT hyperplasia is seen in certain obese individuals(166). It has also been observed that weight loss on the order of 5% of total body weight is sufficient to cause reductions in adipocyte size in severely obese women (40).

Based on the magnitude of weight loss observed in our study (11.3 ± 3.1 % of starting weight, T1 to T3) and the time course of the measurements recorded, it is likely that the significant increases in NIR scattering amplitude (a mean increase of 17.0% with weight loss) observed are reflective of the reduction in subcutaneous adipocyte size associated with weight loss. In the near-infrared range of the electromagnetic spectrum (650-1000), scattering of light occurs due to inhomogeneity in refractive index between tissue components(67). In the case of shrinking adipocytes, one would expect an increased frequency of such scattering events as a result of higher density of membranes surrounding both adipocytes and various intracellular and extracellular components. Furthermore, the scattering slope parameter (b), a measure of the wavelength dependence of NIR scattering, became significantly more negative from T1 to T3. A more negative slope denotes a steeper decrease in reduced scattering coefficient (μ_s') as a function of wavelength, and can be attributed to a decrease in average size of optical scatterers in the tissue. Additionally, the fact that the change in scattering amplitude was detectable in six weeks suggests a relatively rapid onset.

While it is likely that the significant changes in scattering observed correlate with adipocyte size reductions, there are some clear limitations to this conclusion. Firstly, our study did not include histological confirmation of adipocyte size. Additionally, it cannot be said with certainty which cellular or extracellular components are contributing to the scattering changes observed. It is unlikely that changes in average lipid droplet size would affect NIR scattering directly because NIR scattering events are caused by components with diameters on the order of the optical wavelength (650-1000 nm) of the incident light(67). However, this does not preclude the possibility of increased density of membrane-bound subcellular components small enough to contribute to bulk tissue scattering, such as vesicles, mitochondria, or other organelles (59,167). If CR of the duration studied here causes appreciable browning of white AT, or an increased proportion of beige adipocytes, then it is likely that increases in multilocular lipid droplets are also contributing to the changes in A and b . To determine the precise source of the observed scattering changes, further studies incorporating microscopy are needed as well as the use of more rigorous biophysical modeling techniques.

Changes in AT metabolism

In addition to the above effects on scattering parameters, we observed that weight loss is also associated with significant increases in [HbR], [THb], water fraction and TOI, all of which reflect underlying metabolism and perfusion. It is known that obesity is associated with reduced blood flow in subcutaneous AT at rest (148), and with a blunted increase in post-prandial AT blood flow (162), but the implications of this reduction on O₂ delivery are

not known with certainty. In fact, measurements of O_2 partial pressure in AT have been known to be elevated in obesity, possibly reflecting a deficit in the tissue's ability to extract O_2 for metabolism(43). While overall subcutaneous AT O_2 consumption is low compared to other tissues(148), there is evidence for the relevance of AT metabolism to certain disease states. For example, the insulin sensitizing action of thiazolidinediones may be partially dependent on increased AT secretion of adiponectin, which is related to AT energetics(168). Additionally, it has been demonstrated that exercise training can drive metabolic changes in AT by endocrine secretions from the muscle (154). Furthermore, as described previously, increased oxidative capacity is a feature of brown and beige adipocytes, both of which are associated with improvements in metabolic status.

However, there are studies which highlight gaps in our understanding of the relationship between food intake and AT O_2 flux. For example, recent data from animals seems to indicate that one of the early effects of a high fat diet is elevated AT O_2 consumption driven by mitochondrial uncoupling (41). This in turn leads to relative AT hypoxia and downstream HIF-1 α mediated inflammation, one of the phenomena implicated in insulin resistance (41). Much remains to be understood about the relationship between diet status, inflammation, and AT metabolism in humans, and the relative lack of human data on this subject is due to the difficulties involved in measuring AT blood flow and pO_2 .

While DOSI cannot directly measure these quantities, it is sensitive to changes in the balance of microvascular perfusion, metabolism, and O_2 saturation. Taken together, the changes observed in subcutaneous AT with weight loss indicate an increase in resting metabolism (TOI), O_2 extraction ([HbR]), and water content. A 2003 study demonstrated that subcutaneous AT water content does increase with weight loss by calorie restriction,

as assessed by a skin-surface measurement of dielectric constant(46). The authors attributed this increase in water to increased tissue blood flow and nutrient delivery, and also described a correlation between the increase in water and improvements in insulin sensitivity(46). Using a direct spectroscopic measurement (DOSI), we observed an increase in AT [THb] and water content, further supporting this proposed relationship, although the precise water tissue compartment (e.g. intravascular vs. extra-vascular; intracellular vs extracellular) cannot be determined from these measurements. Moreover, there was a significant correlation within subjects between the percentage of weight lost and the mean increase in water fraction from T1 to T3, suggesting a metabolic change in subcutaneous AT proportional to the effect of dietary intervention.

The TOI of subcutaneous AT also increased substantially with weight loss, primarily due to increases in both water content and [HbR]. Because [HbR] changes are known to be a consequence of O₂ extraction (124,169), the observed [HbR] increase is likely due to enhanced adipocyte O₂ consumption. This is consistent with our observation of changes in *A* and *b* scattering parameters that suggest a reduction in adipocyte size with weight loss. Adipocyte shrinkage is thought to reduce the diffusion distance of O₂ from the capillaries to the mitochondria (7), potentiating more efficient extraction. The increases in water content and TOI were larger between T2 and T3, suggesting a delayed effect that is dependent on the AT structural change described by larger scattering changes between T1 and T2.

Limitations

It is clear from these studies that DOSI measurements are sensitive to structural and metabolic changes in AT that occur in response to weight loss. However, there are some limitations to this conclusion. First, we have not attempted to conduct histological analysis on AT samples from weight loss subjects, and must therefore rely on known effects of weight loss reported by others. Second, the small sample size thus far ($n = 10$) prevents rigorous analysis of correlations between changes in DOSI parameters and the degree of weight loss or other individual subject characteristics such as insulin resistance or severity of obesity. An additional concern is that the relatively large time between measurements (six weeks) limited our ability to determine the sequence of events, and the time of onset of changes. Animal studies show that AT O_2 consumption can change within a matter of days after a diet change(6), and adipocyte size increases have been observed to occur within a period of days as well(14). Furthermore, while the morphological effects of CR and weight loss on AT are firmly established (ie, the reduction in adipocyte size), there are fewer published studies in humans on metabolic changes. Finally, future studies must also quantitatively explore the contribution of spatial heterogeneity on the abdominal surface on the changes described.

Conclusions

This study describes, for the first time, the use of a quantitative, non-invasive spectroscopic technique (DOSI) for measuring dynamic changes in adipose tissue light-

tissue interactions *in vivo*. We have applied this technology to study the response of AT to calorie restriction, an intervention known to produce significant improvements in weight and in health. Our data demonstrate that DOSI-detected changes in optical and physiological properties are consistent with existing hypotheses on the response of AT to CR and weight loss. DOSI may contribute to a fuller understanding of AT biology in various metabolic states, and may constitute a new bedside tool for monitoring AT metabolism and composition generally. While DOSI is not capable of the spatial resolution of MRI, it offers advantages in quantitation, spectral information content, ease of application and cost. If the findings of this study are repeated and correlated with specific cellular phenomena, DOSI and similar technologies might be used to guide therapeutic interventions such as diet, exercise, and medication by assessing their impact on AT physiology quantitatively and longitudinally. Additionally, considering that the magnitude of weight loss seen in this study was associated with significant reduction in blood pressure (systolic: -9 ± 4 mm Hg), it is possible that the changes we have observed in adipose light-tissue interactions may correlate with improvements in vascular disease risk.

CHAPTER 6: Concluding remarks and future directions

While the individual experimental chapters contain conclusions that follow from specific results, there are some general statements to be made here, as well as some suggestions for future elaboration of these studies.

Exercise studies

While NIRS measurements during exercise are by no means novel, the implementation of TR-NIRS and the analysis methods used have made the studies here worthwhile contributions with novel aspects to them. We have demonstrated the utility of TR-NIRS in making continuous measurements of tissue oxygenation in muscle and brain during exercise, as well as longitudinally in individual subjects undergoing a training program. This is not trivial, as the lack of quantitation associated with most commercial CW-NIRS systems means that such longitudinal comparisons are much more difficult. The use of piecewise regression to characterize threshold behavior shows the utility of NIRS in combination with existing paradigms of our understanding of incremental exercise. The data obtained from studying cerebral oxygenation hints at both vascular adaptation in the brain (chapter 3), and a connection between the sensation of fatigue and PFC hemodynamics (chapter 4). There has also been an attempt to connect physiology measured in specific tissues to patterns in ventilation (chapter 2). And finally, these data suggest that there may be good reason to employ quantitative approaches that can

measure scattering coefficients due to potential errors in reported oxygenation late in exercise if this is not done.

There are several potential areas of focus that could form the next set of studies. First, and most obvious would be to apply the same experimental protocols in non-healthy subjects. Indeed, these studies have begun in populations of obese children and analysis of the data is underway. A second area of interest would be to examine cerebral oxygenation patterns with simultaneous measurements of circulating lactate. The role of lactate in cerebral O₂ uptake is an area of great interest (170), and to determine the kinetics of brain [HbR] in relation to real time kinetics in blood lactate would be highly desirable and translatable to practical exercise physiology. Thirdly, another task would be to quantify the influence of superficial signals on the detected TR-NIRS parameters. This is of course a perennial concern with reflectance measurements, and will need to be continuously addressed using various devices and modeling techniques. Finally, it would be very valuable to conduct a study of cerebral oxygenation using the DOSI system, so that broadband optical properties could be characterized. It is likely that there are changes in water content in high-intensity exercise (20), and accounting for this might provide a fuller picture of the PFC response to exercise.

With regard to the studies of blood flow restriction (chapter 4), the obvious continuation would be to study the effects of resistance training with and without BFR. Such a study is currently in progress, and includes both DOSI measurements of muscle optical properties, and TR-NIRS characterization of hemodynamics in response to occlusion. These results were not included in this manuscript, but preliminary data are extremely interesting.

Measurements of adipose tissue

To our knowledge, this is the first application of NIR spectroscopy to the study of adipose physiology, and this constitutes a unique contribution to the field. However, these results are very preliminary, and raise many more questions than could possibly be answered. There are some very obvious areas of inquiry that ought to be pursued to extend the knowledge gained from these measurements.

Firstly, DOSI measurements of AT must be combined with some histological analysis of cell morphology and vascularization. This could be done either *in vivo* or *ex vivo*, on existing samples of fat. It should be established whether scattering properties of fat tissue correspond in a reliable way to cell size and/or density. If so, this would make the translational value of DOSI much higher, as it would provide a potential method for monitoring insulin resistance. Another specific question is whether calorie restriction causes true increases in mitochondrial content. This might be done using NADH fluorescence techniques, and possible studies in smaller animals. Another further area that has already begun is the use of more sophisticated spectral analysis to determine subtle changes in absorption signature that might reflect lipid composition changes in AT occurring with weight loss (68).

Even more basically, studies should be done to determine how soon after diet change are optical property changes detectable. This would be done by conducting assessments at earlier time points. Additionally, it would be useful to determine which subcutaneous fat depots respond strongly, and which more weakly to the intervention. There is evidence that lower body subcutaneous fat responds differently to upper body

subcutaneous fat, with differential tendencies toward hyperplasia as opposed to hypertrophy (171). And finally, it would be interesting to determine whether existing pharmacological treatments for type II diabetes which act by improving insulin sensitivity, might have a similar effect as CR upon AT. If so, optical measurements of AT may be a way of screening for efficacy for such treatments, in terms of their ability to alter subcutaneous AT phenotype.

REFERENCES

1. Murphy SL, Xu J, Kochanek KD. National vital statistics reports. *National vital statistics reports*. 2013;61(4).
2. Babelova A, Sedding DG, Brandes RP. Anti-atherosclerotic mechanisms of statin therapy. *Current Opinion in Pharmacology*. 2013;13(2):260-264.
3. Tahrani AA, Bailey CJ, Del Prato S, Barnett AH. Management of type 2 diabetes: new and future developments in treatment. *The Lancet*.378(9786):182-197.
4. American Diabetes A. Standards of Medical Care in Diabetes—2014. *Diabetes Care*. 2014;37(Supplement 1):S14-S80.
5. Stone NJ, Robinson JG, Lichtenstein AH, et al. 2013 ACC/AHA Guideline on the Treatment of Blood Cholesterol to Reduce Atherosclerotic Cardiovascular Risk in Adults: A Report of the American College of Cardiology/American Heart Association Task Force on Practice Guidelines. *Journal of the American College of Cardiology*. 2014;63(25, Part B):2889-2934.
6. Mokdad AH, Marks JS, Stroup DF, Gerberding JL. Actual causes of death in the United States, 2000. *Jama*. 2004;291(10):1238-1245.
7. Colditz GA. Economic costs of obesity and inactivity. *Med Sci Sports Exerc*. 1999;31(11 Suppl):S663-667.
8. Sonntag D, Ali S, Lehnert T, Konnopka A, Riedel-Heller S, König HH. Estimating the lifetime cost of childhood obesity in Germany: Results of a Markov Model. *Pediatr Obes*. 2015.

9. Ogden CL, Carroll MD, Kit BK, Flegal KM. Prevalence of childhood and adult obesity in the United States, 2011-2012. *Jama*. 2014;311(8):806-814.
10. Ochner CN, Tsai AG, Kushner RF, Wadden TA. Treating obesity seriously: when recommendations for lifestyle change confront biological adaptations. *The Lancet Diabetes & Endocrinology*.
11. Nieuwdorp M, Gilijamse PW, Pai N, Kaplan LM. Role of the microbiome in energy regulation and metabolism. *Gastroenterology*. 2014;146(6):1525-1533.
12. Church T. Exercise in Obesity, Metabolic Syndrome, and Diabetes. *Progress in Cardiovascular Diseases*. 2011;53(6):412-418.
13. Kokkinos P. Cardiorespiratory fitness, exercise, and blood pressure. *Hypertension*. 2014;64(6):1160-1164.
14. Balkau B, Mhamdi L, Oppert J-M, et al. Physical Activity and Insulin Sensitivity: The RISC Study. *Diabetes*. 2008;57(10):2613-2618.
15. Kim Y, Park H. Does Regular Exercise without Weight Loss Reduce Insulin Resistance in Children and Adolescents? *Int J Endocrinol*. 2013;2013:402592.
16. Whipp BJ, Davis JA. The ventilatory stress of exercise in obesity. *The American review of respiratory disease*. 1984;129(2 Pt 2):S90-92.
17. Norman A-C, Drinkard B, McDuffie JR, Ghorbani S, Yanoff LB, Yanovski JA. Influence of Excess Adiposity on Exercise Fitness and Performance in Overweight Children and Adolescents. *Pediatrics*. 2005;115(6):e690-e696.
18. Zabinski MF, Saelens BE, Stein RI, Hayden-Wade HA, Wilfley DE. Overweight Children's Barriers to and Support for Physical Activity. *Obesity Research*. 2003;11(2):238-246.

19. Rowell LB, Leary DS. Reflex control of the circulation during exercise: chemoreflexes and mechanoreflexes. *Journal of Applied Physiology*. 1990;69(2):407-418.
20. Wasserman K, Hansen JE, Sue DY, Whipp BJ, Froelicher VF. Principles of exercise testing and interpretation. *Journal of Cardiopulmonary Rehabilitation and Prevention*. 1987;7(4):189.
21. Ekkekakis P. Illuminating the black box: investigating prefrontal cortical hemodynamics during exercise with near-infrared spectroscopy. *J Sport Exerc Psychol*. 2009;31(4):505-553.
22. Miller EK, Cohen JD. An integrative theory of prefrontal cortex function. *Annu Rev Neurosci*. 2001;24:167-202.
23. Lambert EV, St Clair Gibson A, Noakes TD. Complex systems model of fatigue: integrative homeostatic control of peripheral physiological systems during exercise in humans. *Br J Sports Med*. 2005;39(1):52-62.
24. Dietrich A. Transient hypofrontality as a mechanism for the psychological effects of exercise. *Psychiatry Research*. 2006;145(1):79-83.
25. Hillman CH, Erickson KI, Kramer AF. Be smart, exercise your heart: exercise effects on brain and cognition. *Nat Rev Neurosci*. 2008;9(1):58-65.
26. Strangman G, Culver JP, Thompson JH, Boas DA. A quantitative comparison of simultaneous BOLD fMRI and NIRS recordings during functional brain activation. *Neuroimage*. 2002;17(2):719-731.
27. Turner N, Cooney GJ, Kraegen EW, Bruce CR. Fatty acid metabolism, energy expenditure and insulin resistance in muscle. *Journal of Endocrinology*. 2014;220(2):T61-T79.

28. Samuel VT, Shulman GI. Mechanisms for insulin resistance: common threads and missing links. *Cell*. 2012;148(5):852-871.
29. Eckardt K, Gorgens SW, Raschke S, Eckel J. Myokines in insulin resistance and type 2 diabetes. *Diabetologia*. 2014;57(6):1087-1099.
30. Mann S, Beedie C, Balducci S, et al. Changes in insulin sensitivity in response to different modalities of exercise: a review of the evidence. *Diabetes/Metabolism Research and Reviews*. 2014;30(4):257-268.
31. Geliebter A, Maher MM, Gerace L, Gutin B, Heymsfield SB, Hashim SA. Effects of strength or aerobic training on body composition, resting metabolic rate, and peak oxygen consumption in obese dieting subjects. *The American Journal of Clinical Nutrition*. 1997;66(3):557-563.
32. SHIMANO T, KRAEMER WJ, SPIERING BA, et al. RELATIONSHIP BETWEEN THE NUMBER OF REPETITIONS AND SELECTED PERCENTAGES OF ONE REPETITION MAXIMUM IN FREE WEIGHT EXERCISES IN TRAINED AND UNTRAINED MEN. *The Journal of Strength & Conditioning Research*. 2006;20(4):819-823.
33. Pellemounter MA, Cullen MJ, Baker MB, et al. Effects of the obese gene product on body weight regulation in ob/ob mice. *Science*. 1995;269(5223):540-543.
34. Sainz N, Barrenetxe J, Moreno-Aliaga MJ, Martinez JA. Leptin resistance and diet-induced obesity: central and peripheral actions of leptin. *Metabolism*. 2015;64(1):35-46.
35. Silha JV, Krsek M, Skrha JV, Sucharda P, Nyomba BL, Murphy LJ. Plasma resistin, adiponectin and leptin levels in lean and obese subjects: correlations with insulin resistance. *European Journal of Endocrinology*. 2003;149(4):331-335.

36. Lim S, Quon MJ, Koh KK. Modulation of adiponectin as a potential therapeutic strategy. *Atherosclerosis*. 2014;233(2):721-728.
37. Björntorp P, Gustafson A, Persson B. ADIPOSE TISSUE FAT CELL SIZE AND NUMBER IN RELATION TO METABOLISM IN ENDOGENOUS HYPERTRIGLYCERIDEMIA. *Acta Medica Scandinavica*. 1971;190(1-6):363-367.
38. Heinonen S, Saarinen L, Naukkarinen J, et al. Adipocyte morphology and implications for metabolic derangements in acquired obesity. *Int J Obes (Lond)*. 2014.
39. Cotillard A, Poitou C, Torcivia A, et al. Adipocyte size threshold matters: link with risk of type 2 diabetes and improved insulin resistance after gastric bypass. *J Clin Endocrinol Metab*. 2014;99(8):E1466-1470.
40. Varady KA, Tussing L, Bhutani S, Braunschweig CL. Degree of weight loss required to improve adipokine concentrations and decrease fat cell size in severely obese women. *Metabolism*. 2009;58(8):1096-1101.
41. Lee YS, Kim JW, Osborne O, et al. Increased Adipocyte O₂ Consumption Triggers HIF-1 α , Causing Inflammation and Insulin Resistance in Obesity. *Cell*. 2014;157(6):1339-1352.
42. Lemoine AY, Ledoux S, Larger E. Adipose tissue angiogenesis in obesity. *Thromb Haemost*. 2013;110(4):661-668.
43. Goossens GH, Bizzarri A, Venticlef N, et al. Increased Adipose Tissue Oxygen Tension in Obese Compared With Lean Men Is Accompanied by Insulin Resistance, Impaired Adipose Tissue Capillarization, and Inflammation. *Circulation*. 2011;124(1):67-76.

44. Le KA, Mahurkar S, Alderete TL, et al. Subcutaneous Adipose Tissue Macrophage Infiltration Is Associated With Hepatic and Visceral Fat Deposition, Hyperinsulinemia, and Stimulation of NF- κ B Stress Pathway. *Diabetes*. 2011;60(11):2802-2809.
45. Harms M, Seale P. Brown and beige fat: development, function and therapeutic potential. *Nat Med*. 2013;19(10):1252-1263.
46. Laaksonen DE, Nuutinen J, Lahtinen T, Rissanen A, Niskanen LK. Changes in abdominal subcutaneous fat water content with rapid weight loss and long-term weight maintenance in abdominally obese men and women. *Int J Obes Relat Metab Disord*. 2003;27(6):677-683.
47. Bucerius J, Mani V, Wong S, et al. Arterial and fat tissue inflammation are highly correlated: a prospective 18F-FDG PET/CT study. *Eur J Nucl Med Mol Imaging*. 2014;41(5):934-945.
48. Thomas EL, Parkinson JR, Frost GS, et al. The missing risk: MRI and MRS phenotyping of abdominal adiposity and ectopic fat. *Obesity (Silver Spring)*. 2012;20(1):76-87.
49. Chance B. Optical method. *Annual review of biophysics and biophysical chemistry*. 1991;20(1):1-30.
50. Sassaroli A, Fantini S. Comment on the modified Beer? Lambert law for scattering media. *Physics in Medicine and Biology*. 2004;49(14):N255.
51. Boas DA, Franceschini MA, Dunn AK, Strangman G. Noninvasive imaging of cerebral activation with diffuse optical tomography. *In vivo optical imaging of brain function*. 2002:193-221.

52. Tsuchiya Y. Photon path distribution and optical responses of turbid media: theoretical analysis based on the microscopic Beer-Lambert law. *Physics in Medicine and Biology*. 2001;46(8):2067.
53. von Kompen EJ. Spectrophotometry of hemoglobin and hemoglobin derivatives. *Advances in clinical chemistry*. 1983;23:199.
54. Jobsis FF. Noninvasive, infrared monitoring of cerebral and myocardial oxygen sufficiency and circulatory parameters. *Science*. 1977;198(4323):1264-1267.
55. Mancini DM, Bolinger L, Li H, Kendrick K, Chance B, Wilson JR. Validation of near-infrared spectroscopy in humans. *Journal of Applied Physiology*. 1994;77(6):2740-2747.
56. Ferrari M, Quaresima V. A brief review on the history of human functional near-infrared spectroscopy (fNIRS) development and fields of application. *Neuroimage*. 2012;63(2):921-935.
57. Hoshi Y. Towards the next generation of near-infrared spectroscopy. *Philos Trans A Math Phys Eng Sci*. 2011;369(1955):4425-4439.
58. Yodh A, Chance B. Spectroscopy and imaging with diffusing light. *Physics Today*. 1995;48(3):34-41.
59. Bartek M, Wang X, Wells W, Paulsen KD, Pogue BW. Estimation of subcellular particle size histograms with electron microscopy for prediction of optical scattering in breast tissue. *J Biomed Opt*. 2006;11(6):064007.
60. Patterson MS, Chance B, Wilson BC. Time resolved reflectance and transmittance for the non-invasive measurement of tissue optical properties. *Appl Opt*. 1989;28(12):2331-2336.

61. Yamashita Y, Niwayama M. Principles and Instrumentation. In: Jue T, Masuda K, eds. *Application of Near Infrared Spectroscopy in Biomedicine*. Vol 4: Springer US; 2013:1-19.
62. Gunadi S, Leung TS, Elwell CE, Tachtsidis I. Spatial sensitivity and penetration depth of three cerebral oxygenation monitors. *Biomedical Optics Express*. 2014;5(9):2896-2912.
63. Tromberg BJ, Coquoz O, Fishkin JB, et al. Non-invasive measurements of breast tissue optical properties using frequency-domain photon migration. *Philosophical Transactions of the Royal Society of London B: Biological Sciences*. 1997;352(1354):661-668.
64. Fishkin JB, Coquoz O, Anderson ER, Brenner M, Tromberg BJ. Frequency-domain photon migration measurements of normal and malignant tissue optical properties in a human subject. *Appl Opt*. 1997;36(1):10-20.
65. No KS, Kwong R, Chou PH, Cerussi A. Design and testing of a miniature broadband frequency domain photon migration instrument. *J Biomed Opt*. 2008;13(5):050509.
66. Bevilacqua F, Berger AJ, Cerussi AE, Jakubowski D, Tromberg BJ. Broadband absorption spectroscopy in turbid media by combined frequency-domain and steady-state methods. *Appl Opt*. 2000;39(34):6498-6507.
67. Jacques SL. Optical properties of biological tissues: a review. *Phys Med Biol*. 2013;58(11):R37-61.
68. Kukreti S, Cerussi A, Tromberg B, Gratton E. Intrinsic tumor biomarkers revealed by novel double-differential spectroscopic analysis of near-infrared spectra. *Journal of Biomedical Optics*. 2007;12(2):020509-020509-020503.

69. Cerussi A, Shah N, Hsiang D, Durkin A, Butler J, Tromberg BJ. In vivo absorption, scattering, and physiologic properties of 58 malignant breast tumors determined by broadband diffuse optical spectroscopy. *J Biomed Opt.* 2006;11(4):044005.
70. Chung SH, Yu H, Su MY, Cerussi AE, Tromberg BJ. Molecular imaging of water binding state and diffusion in breast cancer using diffuse optical spectroscopy and diffusion weighted MRI. *J Biomed Opt.* 2012;17(7):071304.
71. Leproux A, Durkin A, Compton M, Cerussi AE, Gratton E, Tromberg BJ. Assessing tumor contrast in radiographically dense breast tissue using Diffuse Optical Spectroscopic Imaging (DOSI). *Breast Cancer Res.* 2013;15(5):R89.
72. O'Sullivan TD, Leproux A, Chen JH, et al. Optical imaging correlates with magnetic resonance imaging breast density and reveals composition changes during neoadjuvant chemotherapy. *Breast Cancer Res.* 2013;15(1):R14.
73. Moalla W, Dupont G, Temfemo A, Maingourd Y, Weston M, Ahmaidi S. Assessment of exercise capacity and respiratory muscle oxygenation in healthy children and children with congenital heart diseases. *Appl Physiol Nutr Metab.* 2008;33(3):434-440.
74. Dogra S, Spencer MD, Murias JM, Paterson DH. Oxygen uptake kinetics in endurance-trained and untrained postmenopausal women. *Appl Physiol Nutr Metab.* 2013;38(2):154-160.
75. Murias JM, Spencer MD, Kowalchuk JM, Paterson DH. Muscle deoxygenation to $\dot{V}O_2$ relationship differs in young subjects with varying $\tau\dot{V}O_2$. *Eur J Appl Physiol.* 2011.

76. Murias JM, Spencer MD, Delorey DS, Gurd BJ, Kowalchuk JM, Paterson DH. Speeding of VO₂ kinetics during moderate-intensity exercise subsequent to heavy-intensity exercise is associated with improved local O₂ distribution. *J Appl Physiol*. 2011.
77. Spencer MD, Murias JM, Paterson DH. Characterizing the profile of muscle deoxygenation during ramp incremental exercise in young men. *Eur J Appl Physiol*. 2012;112(9):3349-3360.
78. Ferreira LF, Townsend DK, Lutjemeier BJ, Barstow TJ. Muscle capillary blood flow kinetics estimated from pulmonary O₂ uptake and near-infrared spectroscopy. *J Appl Physiol*. 2005;98(5):1820-1828.
79. Habazettl H, Athanasopoulos D, Kuebler WM, et al. Near-infrared spectroscopy and indocyanine green derived blood flow index for noninvasive measurement of muscle perfusion during exercise. *J Appl Physiol*. 2010;108(4):962-967.
80. Taelman J, Vanderhaegen J, Robijns M, Naulaers G, Spaepen A, Van Huffel S. Estimation of muscle fatigue using surface electromyography and near-infrared spectroscopy. *Adv Exp Med Biol*. 2011;701:353-359.
81. Bhambhani Y, Malik R, Mookerjee S. Cerebral oxygenation declines at exercise intensities above the respiratory compensation threshold. *Respir Physiol Neurobiol*. 2007;156(2):196-202.
82. Perrey S. Non-invasive NIR spectroscopy of human brain function during exercise. *Methods*. 2008;45(4):289-299.
83. Ferreira LF, Hueber DM, Barstow TJ. Effects of assuming constant optical scattering on measurements of muscle oxygenation by near-infrared spectroscopy during exercise. *J Appl Physiol*. 2007;102(1):358-367.

84. Ferreira LF, Koga S, Barstow TJ. Dynamics of noninvasively estimated microvascular O₂ extraction during ramp exercise. *J Appl Physiol.* 2007;103(6):1999-2004.
85. DeLorey DS, Kowalchuk JM, Paterson DH. Relationship between pulmonary O₂ uptake kinetics and muscle deoxygenation during moderate-intensity exercise. *J Appl Physiol.* 2003;95(1):113-120.
86. Tew G, Ruddock A, Saxton J. Skin blood flow differentially affects near-infrared spectroscopy-derived measures of muscle oxygen saturation and blood volume at rest and during dynamic leg exercise. *European Journal of Applied Physiology.* 2010;110(5):1083-1089.
87. Mortensen SP, Damsgaard R, Dawson EA, Secher NH, González-Alonso J. Restrictions in systemic and locomotor skeletal muscle perfusion, oxygen supply and V_{O2} during high-intensity whole-body exercise in humans. *The Journal of Physiology.* 2008;586(10):2621-2635.
88. Seifert T, Secher NH. Sympathetic influence on cerebral blood flow and metabolism during exercise in humans. *Progress in Neurobiology.* 2011;95(3):406-426.
89. Koga S, Poole DC, Fukuoka Y, et al. Methodological validation of the dynamic heterogeneity of muscle deoxygenation within the quadriceps during cycle exercise. *Am J Physiol Regul Integr Comp Physiol.* 2011;301(2):R534-541.
90. Chin LM, Kowalchuk JM, Barstow TJ, et al. The relationship between muscle deoxygenation and activation in different muscles of the quadriceps during cycle ramp exercise. *J Appl Physiol (1985).* 2011;111(5):1259-1265.

91. Bowen TS, Rossiter HB, Benson AP, et al. Slowed oxygen uptake kinetics in hypoxia correlate with the transient peak and reduced spatial distribution of absolute skeletal muscle deoxygenation. *Exp Physiol*. 2013;98(11):1585-1596.
92. Messere A, Roatta S. Influence of cutaneous and muscular circulation on spatially resolved versus standard Beer-Lambert near-infrared spectroscopy. *Physiol Rep*. 2013;1(7):e00179.
93. Rupp T, Perrey S. Prefrontal cortex oxygenation and neuromuscular responses to exhaustive exercise. *Eur J Appl Physiol*. 2008;102(2):153-163.
94. Rooks CR, Thom NJ, McCully KK, Dishman RK. Effects of incremental exercise on cerebral oxygenation measured by near-infrared spectroscopy: a systematic review. *Prog Neurobiol*. 2010;92(2):134-150.
95. Subudhi AW, Olin JT, Dimmen AC, Polaner DM, Kayser B, Roach RC. Does cerebral oxygen delivery limit incremental exercise performance? *J Appl Physiol*. 2011;111(6):1727-1734.
96. Secher NH, Seifert T, Van Lieshout JJ. Cerebral blood flow and metabolism during exercise: implications for fatigue. *J Appl Physiol*. 2008;104(1):306-314.
97. Vogiatzis I, Louvaris Z, Habazettl H, et al. Frontal cerebral cortex blood flow, oxygen delivery and oxygenation during normoxic and hypoxic exercise in athletes. *The Journal of Physiology*. 2011;589(16):4027-4039.
98. Fisher JP, Hartwich D, Seifert T, et al. Cerebral perfusion, oxygenation and metabolism during exercise in young and elderly individuals. *J Physiol*. 2013;591(Pt 7):1859-1870.

99. Lee J, Kim JG, Mahon S, et al. Tissue hemoglobin monitoring of progressive central hypovolemia in humans using broadband diffuse optical spectroscopy. *J Biomed Opt.* 2008;13(6):064027.
100. Danduran MJ, Dixon JE, Rao RP. Near Infrared Spectroscopy Describes Physiologic Payback Associated With Excess Postexercise Oxygen Consumption in Healthy Controls and Children With Complex Congenital Heart Disease. *Pediatr Cardiol.* 2011.
101. Thiagarajah JR, Papadopoulos MC, Verkman AS. Noninvasive early detection of brain edema in mice by near-infrared light scattering. *Journal of Neuroscience Research.* 2005;80(2):293-299.
102. Saitoh T, Ooue A, Kondo N, Niizeki K, Koga S. Active muscle oxygenation dynamics measured during high-intensity exercise by using two near-infrared spectroscopy methods. *Adv Exp Med Biol.* 2010;662:225-230.
103. Blain G, Meste O, Bouchard T, Bermon S. Assessment of ventilatory thresholds during graded and maximal exercise test using time varying analysis of respiratory sinus arrhythmia. *Br J Sports Med.* 2005;39(7):448-452; discussion 448-452.
104. Mizuno M, Tokizawa K, Iwakawa T, Muraoka I. Inflection points of cardiovascular responses and oxygenation are correlated in the distal but not the proximal portions of muscle during incremental exercise. *Journal of Applied Physiology.* 2004;97(3):867-873.
105. Bodner ME, Rhodes EC. A review of the concept of the heart rate deflection point. *Sports Med.* 2000;30(1):31-46.

106. Colcombe SJ, Erickson KI, Scalf PE, et al. Aerobic Exercise Training Increases Brain Volume in Aging Humans. *The Journals of Gerontology Series A: Biological Sciences and Medical Sciences*. 2006;61(11):1166-1170.
107. Verburgh L, Königs M, Scherder EJA, Oosterlaan J. Physical exercise and executive functions in preadolescent children, adolescents and young adults: a meta-analysis. *Br J Sports Med*. 2014;48(12):973-979.
108. Muggeo VMR. Estimating regression models with unknown break-points. *Stat Med*. 2003;22(19):3055-3071.
109. Muggeo VMR. Segmented: an R package to fit regression models with broken-line relationships. *R news*. 2008;8(1):20-25.
110. Oussaidene K, Prieur F, Tagougui S, Abaidia A, Matran R, Mucci P. Aerobic fitness influences cerebral oxygenation response to maximal exercise in healthy subjects. *Respir Physiol Neurobiol*. 2015;205:53-60.
111. Culver JP, Siegel AM, Franceschini MA, Mandeville JB, Boas DA. Evidence that cerebral blood volume can provide brain activation maps with better spatial resolution than deoxygenated hemoglobin. *Neuroimage*. 2005;27(4):947-959.
112. Swain RA, Harris AB, Wiener EC, et al. Prolonged exercise induces angiogenesis and increases cerebral blood volume in primary motor cortex of the rat. *Neuroscience*. 2003;117(4):1037-1046.
113. Isaacs KR, Anderson tJ, Alcantara AA, Black JE, Greenough WT. Exercise and the Brain: Angiogenesis in the Adult Rat Cerebellum After Vigorous Physical Activity and Motor Skill Learning. *J Cereb Blood Flow Metab*. 1992;12(1):110-119.

114. Dehghani H, Delpy DT. Near-infrared spectroscopy of the adult head: effect of scattering and absorbing obstructions in the cerebrospinal fluid layer on light distribution in the tissue. *Appl Opt.* 2000;39(25):4721-4729.
115. Racinais S, Buchheit M, Girard O. Breakpoints in ventilation, cerebral and muscle oxygenation, and muscle activity during an incremental cycling exercise. *Front Physiol.* 2014;5:142.
116. Ganesan G, Cotter JA, Reuland W, Cerussi AE, Tromberg BJ, Galassetti P. Effect of blood flow restriction on tissue oxygenation during knee extension. *Med Sci Sports Exerc.* 2015;47(1):185-193.
117. Takarada Y, Sato Y, Ishii N. Effects of resistance exercise combined with vascular occlusion on muscle function in athletes. *European Journal of Applied Physiology.* 2002(4):308-314.
118. American College of Sports Medicine position stand. Progression models in resistance training for healthy adults. *Med Sci Sports Exerc.* 2009;41(3):687-708.
119. Sumide T, Sakuraba K, Sawaki K, Ohmura H, Tamura Y. Effect of resistance exercise training combined with relatively low vascular occlusion. *J Sci Med Sport.* 2009;12(1):107-112.
120. Takarada Y, Takazawa H, Ishii N. Applications of vascular occlusion diminish disuse atrophy of knee extensor muscles. *Med Sci Sports Exerc.* 2000;32(12):2035-2039.
121. Cook SB, Brown KA, Deruisseau K, Kanaley JA, Ploutz-Snyder LL. Skeletal muscle adaptations following blood flow-restricted training during 30 days of muscular unloading. *J Appl Physiol.* 2010;109(2):341-349.

122. Karabulut M, Abe T, Sato Y, Bembem MG. The effects of low-intensity resistance training with vascular restriction on leg muscle strength in older men. *Eur J Appl Physiol.* 2010;108(1):147-155.
123. Loenneke JP, Wilson GJ, Wilson JM. A mechanistic approach to blood flow occlusion. *Int J Sports Med.* 2010;31(1):1-4.
124. Ferrari M, Muthalib M, Quaresima V. The use of near-infrared spectroscopy in understanding skeletal muscle physiology: recent developments. *Philos Transact A Math Phys Eng Sci.* 2011;369(1955):4577-4590.
125. Pereira MR, Gomes PC, Bhambhani Y. A Brief Review of the Use of Near Infrared Spectroscopy with Particular Interest in Resistance Exercise. *Sports Med.* 2007;37(7):615-624.
126. de Ruyter CJ, de Boer MD, Spanjaard M, de Haan A. Knee angle-dependent oxygen consumption during isometric contractions of the knee extensors determined with near-infrared spectroscopy. *J Appl Physiol.* 2005;99(2):579-586.
127. Matsuura C, Gomes PS, Haykowsky M, Bhambhani Y. Cerebral and muscle oxygenation changes during static and dynamic knee extensions to voluntary fatigue in healthy men and women: a near infrared spectroscopy study. *Clin Physiol Funct Imaging.* 2011;31(2):114-123.
128. Reynolds L, Levin TA, Medeiros JM, Adler NS, Hallum A. Emg Activity of the Vastus Medialis Oblique and the Vastus Lateralis in Their Role in Patellar Alignment. *Am J Phys Med Rehabil.* 1983;62(2):61-70.
129. Pattyn E, Verdonk P, Steyaert A, et al. Vastus Medialis Obliquus Atrophy : Does It Exist in Patellofemoral Pain Syndrome? *Am J Sports Med.* 2011;39(7):1450-1455.

130. Sheehy P, Burdett RG, Irrgang JJ, VanSwearingen J. An electromyographic study of vastus medialis oblique and vastus lateralis activity while ascending and descending steps. *J Orthop Sports Phys Ther.* 1998;27(6):423-429.
131. Smith TO, Bowyer D, Dixon J, Stephenson R, Chester R, Donell ST. Can vastus medialis oblique be preferentially activated? A systematic review of electromyographic studies. *Physiother Theory Pract.* 2009;25(2):69-98.
132. Noakes TD. Time to move beyond a brainless exercise physiology: the evidence for complex regulation of human exercise performance. *Appl Physiol Nutr Metab.* 2011;36(1):23-35.
133. Matsuura C, Gomes PSC, Haykowsky M, Bhambhani Y. Cerebral and muscle oxygenation changes during static and dynamic knee extensions to voluntary fatigue in healthy men and women: a near infrared spectroscopy study. *Clin Physiol Funct Imaging.* 2011;31(2):114-123.
134. Borg GA. Psychophysical bases of perceived exertion. *Med Sci Sports Exerc.* 1982;14(5):377-381.
135. Kacin A, Strazar K. Frequent low-load ischemic resistance exercise to failure enhances muscle oxygen delivery and endurance capacity. *Scand J Med Sci Sports.* 2011;21(6):e231-e241.
136. Davis SL, Fadel PJ, Cui J, Thomas GD, Crandall CG. Skin blood flow influences near-infrared spectroscopy-derived measurements of tissue oxygenation during heat stress. *J Appl Physiol (1985).* 2006;100(1):221-224.

137. Aletti F, Re R, Pace V, et al. Deep and surface hemodynamic signal from functional time resolved transcranial near infrared spectroscopy compared to skin flowmotion. *Comput Biol Med.* 2012;42(3):282-289.
138. Takano H, Morita T, Iida H, et al. Hemodynamic and hormonal responses to a short-term low-intensity resistance exercise with the reduction of muscle blood flow. *Eur J Appl Physiol.* 2005;95(1):65-73.
139. Kon M, Ikeda T, Homma T, Suzuki Y. Effects of low-intensity resistance exercise under acute systemic hypoxia on hormonal responses. *J Strength Cond Res.* 2012;26(3):611-617.
140. Patterson SD, Ferguson RA. Increase in calf post-occlusive blood flow and strength following short-term resistance exercise training with blood flow restriction in young women. *Eur J Appl Physiol.* 2010;108(5):1025-1033.
141. Prior BM, Yang HT, Terjung RL. What makes vessels grow with exercise training? *J Appl Physiol.* 2004;97(3):1119-1128.
142. de Salles BF, Simao R, Miranda F, Novaes Jda S, Lemos A, Willardson JM. Rest interval between sets in strength training. *Sports Med.* 2009;39(9):765-777.
143. Hollander DB, Reeves GV, Clavier JD, Francois MR, Thomas C, Kraemer RR. Partial occlusion during resistance exercise alters effort sense and pain. *J Strength Cond Res.* 2010;24(1):235-243.
144. Dalsgaard MK, Nybo L, Cai Y, Secher NH. Cerebral metabolism is influenced by muscle ischaemia during exercise in humans. *Exp Physiol.* 2003;88(2):297-302.
145. Bremer AA, Jialal I. Adipose Tissue Dysfunction in Nascent Metabolic Syndrome. *Journal of Obesity.* 2013;2013:1-8.

146. Bremer AA, Devaraj S, Afify A, Jialal I. Adipose tissue dysregulation in patients with metabolic syndrome. *J Clin Endocrinol Metab.* 2011;96(11):E1782-1788.
147. Bassaganya-Riera J, Misyak S, Guri AJ, Hontecillas R. PPAR gamma is highly expressed in F4/80(hi) adipose tissue macrophages and dampens adipose-tissue inflammation. *Cell Immunol.* 2009;258(2):138-146.
148. Hodson L, Humphreys SM, Karpe F, Frayn KN. Metabolic Signatures of Human Adipose Tissue Hypoxia in Obesity. *Diabetes.* 2013;62(5):1417-1425.
149. Pasarica M, Sereda OR, Redman LM, et al. Reduced adipose tissue oxygenation in human obesity: evidence for rarefaction, macrophage chemotaxis, and inflammation without an angiogenic response. *Diabetes.* 2009;58(3):718-725.
150. Samuvel DJ, Jin J, Sundararaj KP, et al. TLR4 Activation and IL-6-Mediated Cross Talk between Adipocytes and Mononuclear Cells Synergistically Stimulate MMP-1 Expression. *Endocrinology.* 2011.
151. Karolina DS, Armugam A, Tavintharan S, et al. MicroRNA 144 impairs insulin signaling by inhibiting the expression of insulin receptor substrate 1 in type 2 diabetes mellitus. *PLoS One.* 2011;6(8):e22839.
152. Wu J, Bostrom P, Sparks LM, et al. Beige adipocytes are a distinct type of thermogenic fat cell in mouse and human. *Cell.* 2012;150(2):366-376.
153. Bartelt A, Heeren J. Adipose tissue browning and metabolic health. *Nat Rev Endocrinol.* 2014;10(1):24-36.
154. Bostrom P, Wu J, Jedrychowski MP, et al. A PGC1-alpha-dependent myokine that drives brown-fat-like development of white fat and thermogenesis. *Nature.* 2012;481(7382):463-468.

155. Nisoli E, Tonello C, Cardile A, et al. Calorie Restriction Promotes Mitochondrial Biogenesis by Inducing the Expression of eNOS. *Science*. 2005;310(5746):314-317.
156. Rossmeislova L, Malisova L, Kracmerova J, Stich V. Adaptation of human adipose tissue to hypocaloric diet. *Int J Obes (Lond)*. 2013;37(5):640-650.
157. Viguerie N, Vidal H, Arner P, et al. Adipose tissue gene expression in obese subjects during low-fat and high-fat hypocaloric diets. *Diabetologia*. 2005;48(1):123-131.
158. Verhoef SP, Camps SG, Bouwman FG, Mariman EC, Westerterp KR. Physiological response of adipocytes to weight loss and maintenance. *PLoS One*. 2013;8(3):e58011.
159. Landgraf K, Rockstroh D, Wagner IV, et al. Evidence of early alterations in adipose tissue biology and function and its association with obesity-related inflammation and insulin resistance in children. *Diabetes*. 2014.
160. Lidell ME, Betz MJ, Dahlqvist Leinhard O, et al. Evidence for two types of brown adipose tissue in humans. *Nat Med*. 2013;19(5):631-634.
161. Pierro ML, Sassaroli A, Bergethon PR, Ehrenberg BL, Fantini S. Phase-amplitude investigation of spontaneous low-frequency oscillations of cerebral hemodynamics with near-infrared spectroscopy: a sleep study in human subjects. *Neuroimage*. 2012;63(3):1571-1584.
162. Frayn KN, Karpe F. Regulation of human subcutaneous adipose tissue blood flow. *Int J Obes*. 2014;38(8):1019-1026.
163. Bates D, Mächler M, Bolker B, Walker S. Fitting linear mixed-effects models using lme4. *arXiv preprint arXiv:1406.5823*. 2014.

164. Winter B. Linear models and linear mixed effects models in R with linguistic applications. *arXiv*. 2013;1308.5499.
165. Hyvonen MT, Spalding KL. Maintenance of white adipose tissue in man. *Int J Biochem Cell Biol*. 2014.
166. Arner P, Spalding KL. Fat cell turnover in humans. *Biochem Biophys Res Commun*. 2010;396(1):101-104.
167. Wang X, Pogue BW, Jiang S, et al. Image reconstruction of effective Mie scattering parameters of breast tissue in vivo with near-infrared tomography. *J Biomed Opt*. 2006;11(4):041106.
168. Kraunsøe R, Boushel R, Hansen CN, et al. Mitochondrial respiration in subcutaneous and visceral adipose tissue from patients with morbid obesity. *The Journal of Physiology*. 2010;588(12):2023-2032.
169. Boas DA, Pitris C, Ramanujam N. *Handbook of biomedical optics*. CRC press; 2012.
170. Dalsgaard MK, Quistorff B, Danielsen ER, Selmer C, Vogelsang T, Secher NH. A reduced cerebral metabolic ratio in exercise reflects metabolism and not accumulation of lactate within the human brain. *The Journal of Physiology*. 2004;554(2):571-578.
171. Tchoukalova YD, Votruba SB, Tchkonina T, Giorgadze N, Kirkland JL, Jensen MD. Regional differences in cellular mechanisms of adipose tissue gain with overfeeding. *Proceedings of the National Academy of Sciences of the United States of America*. 2010;107(42):18226-18231.